

Performance of Digital Radiographic Detectors: Quantification and Assessment Methods¹

Digital radiographic systems are gaining widespread use in many clinical applications. Digital radiographic detectors vary dramatically with respect to the technologies that they use and the particular implementation. Their performance thus varies from system to system. It is often necessary to characterize the performance of a digital radiographic or mammographic detector for optimization, design, comparison, or quality assurance purposes. To do so, it is most useful to measure the performance of the detector in terms of common performance metrics, so that meaningful comparisons can be made.

The performance of a digital radiographic detector can be described in terms of a number of performance factors. Among them, sharpness and noise are two key characteristics that describe the intrinsic image quality performance of digital radiographic systems (1,2). Together, these two, along with an associated characteristic, the signal-to-noise ratio (SNR), define the intrinsic ability of an imaging system to faithfully represent the anatomic features of the body part being imaged.

This chapter first focuses on the quantification of sharpness, noise, and SNR in radiographic systems in terms of common performance metrics of the modulation transfer function (MTF), the noise power spectrum (NPS), and the detective quantum efficiency (DQE). Methods for measuring the MTF, the NPS, and the DQE are then described. The chapter ends with an outline of detector performance factors that may be considered in a comprehensive evaluation of the performance of a detector. The next chapter in the syllabus focuses on the factors that influence the sharpness and noise performance of a digital radiographic detector.

QUANTIFICATION OF DETECTOR PERFORMANCE

Sharpness

The sharpness of a medical imaging system refers to the ability of the system to represent distinct anatomic features within the object being imaged. Sharpness is directly related to resolution, the ability to distinguish neighboring features of an image from each other. Figure 1 illustrates how a degradation of sharpness can lead to loss of detail in a radiograph of a knee.

Detector unsharpness is due to small-scale dispersion and digitization processes during the image formation, discussed in detail in the next chapter.

Advances in Digital Radiography: RSNA Categorical Course in Diagnostic Radiology Physics 2003; pp 37–47.

¹From the Departments of Radiology, Physics, and Biomedical Engineering, DUMC Box 3302, Duke University Medical Center, Durham, NC 27710 (e-mail: samei@duke.edu).

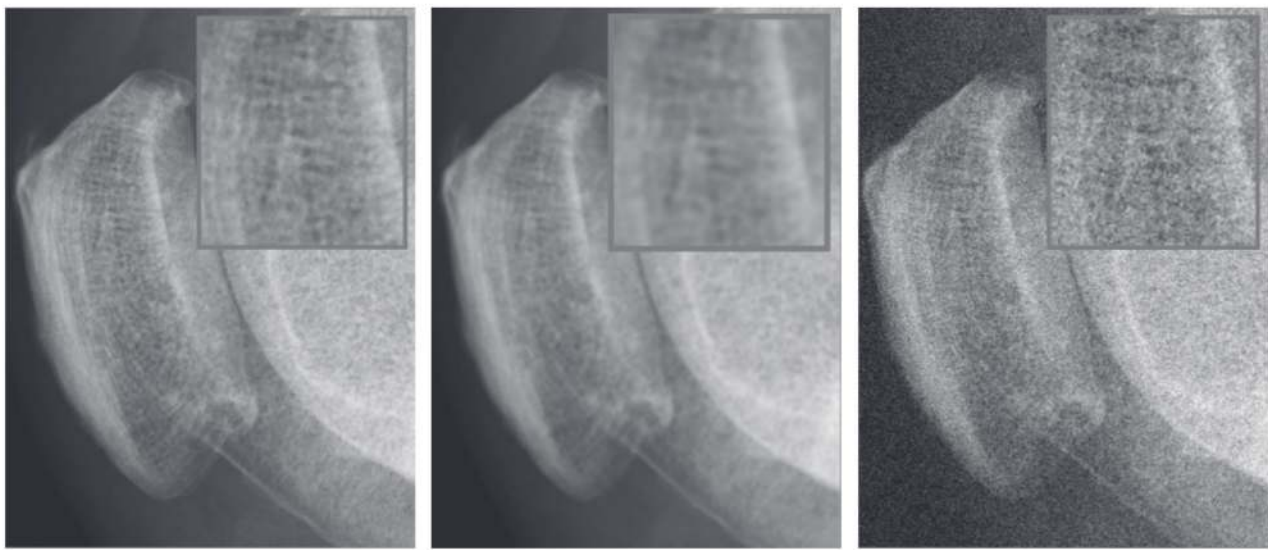


Figure 1. (a) Section of a high-resolution radiograph of the knee. (b) Same section with added blur. (c) Same section with added noise. Magnified sections of the images are shown at upper right corner of each image to demonstrate the loss of detail resolution with added blur and noise.

The sharpness of an imaging detector or system is best characterized in terms of its MTF. The MTF is a measure of the ability of an imaging detector to reproduce image contrast from subject contrast at various spatial frequencies (1,3). Figure 2 offers a schematic depiction of the MTF in one dimension. An input to an imaging system can be thought of as a one-dimensional trace through x-ray intensity variations impinging on the detector. The Fourier theorem states that such an input is equivalent to multiple single-frequency sinusoidal functions (modulations), the summation of which could generate the original input. Thus, these functions can be thought of as the spatial frequency components of the original input. Most radiographic systems are able to transfer or render lower-frequency longer-wavelength modulations to the output or image without much change in the modulation amplitude. However, the amplitudes of higher-frequency modulations are damped, leading to a loss of image detail and sharpness. The MTF is a plot of the ratio of the output-to-input modulations as a function of their spatial frequency. The higher the MTF, the better the sharpness and resolution of an image, as illustrated in Figure 3.

There are two notable advantages of using the MTF to describe the sharpness properties of an imaging system. First, the sharpness can be characterized at multiple levels of detail (ie, spatial frequencies). Second, if a system has multiple components, each of which affects its sharpness, the MTF of the overall system, under suitable conditions, is simply a multiplication of the MTFs of the individual components. For example, the MTF of a digital detector is equal to the product of the MTFs associated with the capture, coupling, and collection elements of

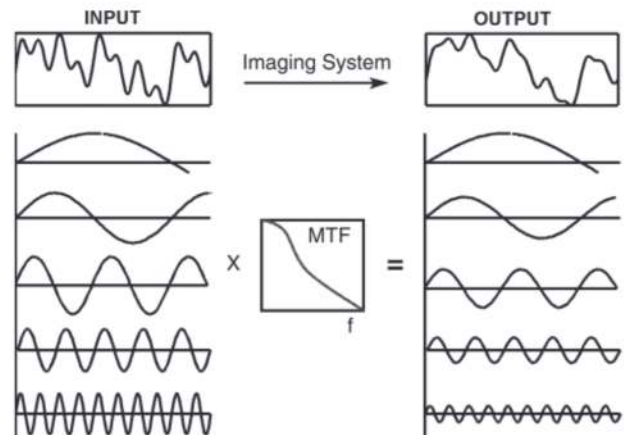


Figure 2. Schematic depiction of the MTF in one dimension, describing the ability of an imaging system to transfer input modulations to output modulations at various spatial frequencies (f).

the detector, which is discussed in more detail in the next chapter.

Mathematically, the MTF is the Fourier amplitude of the point spread function, the response of the detector to an infinitely sharp impulse to the detector (ie, a delta function) (4). In digital radiographic detectors, the response of the detector is dependent on the location of the impulse with respect to the pixel sampling array. As such, digital systems violate an important requirement for proper assessment of the MTF, that is, shift invariance, or the independence of a detector response from the location of an impulse (4). To remedy this limitation, the concept of pre-sampled MTF has been introduced as a way to define

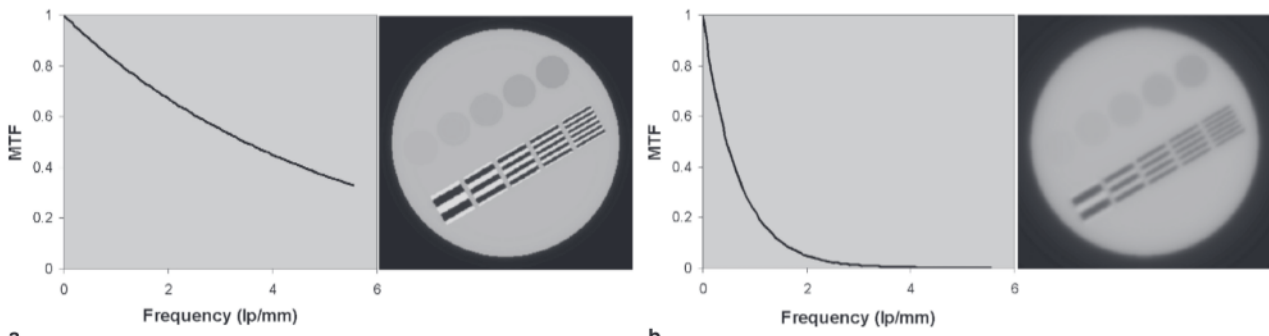


Figure 3. Effect of the MTF on resolution. **(a)** Higher MTF. **(b)** Lower MTF. Higher MTF provides better contrast transfer and resolution in the resultant image than does lower MTF. *lp* = line pairs. (Images were generated with a simulation program developed by David M. Gauntt, PhD, Birmingham, Ala.)

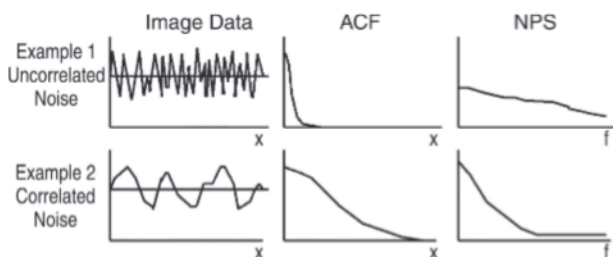


Figure 4. Schematic depiction of the NPS in one dimension, describing the spatial correlation properties of noise as the Fourier transform of the autocorrelation function (ACF). Note that in both examples, the variances of the fluctuations are the same.

the sharpness performance of a digital detector independent of the sampling process (5). Extensive experimental methods have been developed for the assessment of the presampled MTF of digital radiographic systems, which are described later in this chapter.

Noise

In radiographic imaging, noise refers to "unwanted" image details that interfere with the visualization of an abnormality of interest and with the interpretation of an image. These superfluous image details fall into two categories, anatomic noise and radiographic noise (6,7). The former refers to normal unwanted anatomic variations within an image (eg, the rib projection pattern in a chest radiograph confounding the detection of a lung nodule). As such, the characterization of anatomic noise is task-dependent and is not directly related to the intrinsic performance of a detector.

The second type of noise, radiographic noise, however, refers to unwanted variations within an image that do not originate within the imaged subject. Rather, they are "added" variations superimposed on the anatomic data during the acquisition process. Radiographic noise is also directly related to resolution because it affects the ability to resolve distinct features of an image. Comparison of Figure 1a and 1c illustrates how added radiographic noise can lead to loss of detail within an image.

In a discussion of radiographic noise, it should be noted that the term noise is often used to describe two quantities, absolute noise and relative noise. The absolute noise refers to the absolute magnitude of fluctuations within the image (eg, pixel standard deviation), while the relative noise refers to the magnitude of image fluctuations relative to the signal present in the image (eg, pixel standard deviation divided by mean signal). Relative noise is the relevant factor in the detection of abnormalities, and if not qualified, the term noise often refers to relative noise.

Although it is often quantified in terms of variance or standard deviation, radiographic noise is best characterized by its NPS. The NPS is the variance of noise within an image divided among various spatial frequency components of the image (8). As this definition implies, the integral of the NPS is equal to the noise variance. Like the term noise, the NPS is also (confusingly) used to refer to two distinct quantities, absolute NPS (as defined previously) and normalized NPS. The normalized NPS, which is defined as the absolute NPS divided by the mean signal, is related to the relative noise and can be thought of as the relative noise variance divided among various spatial frequencies. Because radiographic noise does not include anatomic variations, the appropriate image for either definition is a uniform flat exposure with no object in the field of view. Broad large-scale variation in such an image is conventionally characterized as nonuniformity, while finer-scale fluctuations are characterized as noise.

Mathematically, the NPS is the normalized squares of Fourier amplitudes averaged over an ensemble of noisy but otherwise uniform images (9). Conceptually easier to grasp than this definition, the NPS is also the Fourier transform of the autocorrelation function, a measure of the spatial correlation of noise patterns within an image (4). Figure 4 offers a schematic depiction of the NPS in one dimension. A one-dimensional trace through a uniform radiographic image might depict fluctuations that can have different correlation properties. A highly uncorrelated noise pattern will render a sharply peaked autocorrelation function and

a broad NPS, while a correlated noise pattern will have a broader autocorrelation function and a narrower NPS. In this example, both patterns have similar variances, and thus the integrals under the NPS curves are equal. However, Figure 4 shows how the NPS can represent the spatial pattern of noise, in addition to its magnitude. The lower the NPS, the better or lower is the noise within the image. The experimental methods to estimate the NPS for a digital radiographic system are described later in this chapter.

Signal-to-Noise Ratio

As noted previously, the term noise in medical imaging has often been used to describe two different quantities: (*a*) the absolute noise, represented by the NPS; and (*b*) the relative noise, represented by the normalized NPS or the SNR. As previously stated, it is the relative noise and the SNR, not the absolute noise, that affect the resolvability of features within an image. Pioneering work by Albert Rose (10) has shown that SNR^2 is inversely proportional to the contrast and the diameter of objects that can be reliably depicted in images with a noise background emulating those of radiographic images. Images with a higher SNR render objects at lower contrast and smaller-diameter thresholds.

Mathematically, the SNR is defined as a scalar quantity equal to the ratio of the mean signal to the standard deviation of fluctuations within an image. However, as implied in the preceding discussion, the resolution (ie, the ability to resolve distinct features in a radiographic image) is influenced by both sharpness and noise. Thus, if expressed as a spatial-frequency-dependent quantity, $\text{SNR}(f)$, the SNR can be used to take into account both of those characteristics. $\text{SNR}(f)$ includes the frequency-dependent signal response of the detector, expressed in terms of the MTF, and its frequency-dependent noise response, expressed in terms of the NPS. Mathematically, $\text{SNR}(f)$ is related to those quantities as follows: $\text{SNR}^2(f) = G^2 \cdot \text{MTF}^2(f)/\text{NPS}(f)$, where G is the system gain.

In the formation of a radiographic image, the noise associated with the finite number of x-ray photons forming the image is often dominant. This noise is commonly known as quantum noise. Quantum noise is governed by Poisson statistics, and thus its associated SNR^2 is directly proportional to the number of individual x-ray quanta forming the image (4). A larger number of quanta (ie, more radiation exposure) render more absolute but less relative noise in the image and vice versa. There are other sources of noise in radiographic images, which are discussed in more detail in the next chapter, but quantum noise defines an "ideal" noise floor below which the noise level of an image cannot be further reduced. The SNR^2 associated with that noise level is denoted as the ideal SNR^2 ($\text{SNR}^2_{\text{ideal}}$), a scalar quantity independent of spatial frequency. In practice, the actual noise level within an

image is associated with an SNR^2 lower than that of $\text{SNR}^2_{\text{ideal}}$. The equivalent number of quanta that would give the same SNR^2 as actually measured, assuming an ideal detector detecting all of the impinging x-ray photons, is known as the noise equivalent quanta (NEQ).

The magnitude of the (relative) noise within a radiographic image is proportional to the number of quanta (and thus to the radiation exposure) used to form the image. Therefore, for a given radiographic system, the actual SNR^2 ($\text{SNR}^2_{\text{actual}}$) (ie, the NEQ) is proportional to $\text{SNR}^2_{\text{ideal}}$. Furthermore, $\text{SNR}^2_{\text{actual}}$ is always less than $\text{SNR}^2_{\text{ideal}}$ in magnitude because of detector inefficiencies, non-x-ray-quanta sources of noise, and added blur in image formation. Given these dependencies, the ratio of $\text{SNR}^2_{\text{actual}}$ (or the NEQ) to $\text{SNR}^2_{\text{ideal}}$ can readily be used as a metric that defines the intrinsic SNR performance of a radiographic detector, theoretically independent of radiation exposure (in the absence of additional non-x-ray-quanta noise sources). This ratio, a single metric commonly used to characterize the intrinsic performance of a digital radiographic system, is known as the DQE. Because $\text{SNR}^2_{\text{actual}}$ is a function of spatial frequency, so is the DQE. The DQE of an "ideal" radiographic detector is equal to unity at all frequencies. Because $\text{SNR}^2_{\text{actual}}$ is always less than $\text{SNR}^2_{\text{ideal}}$, the value of the DQE is always less than 1. However, the higher the DQE, the better are the SNR characteristics of a detector.

MEASUREMENT OF DETECTOR PERFORMANCE

The performance of a digital radiographic detector is dependent on the x-ray beam quality (ie, x-ray source target, peak kilovoltage, and filtration) and quantity (ie, exposure) used to form the image. Thus, the x-ray technique or techniques at which a detector performance is sought is an important consideration. Ideally, the detector should be tested by using techniques similar to those used for the intended application. For example, a chest radiographic system might be tested at 120 kVp, while a digital mammographic system might be tested in the 25–35-kVp range. Additional filtration is necessary to create an x-ray spectrum more closely emulating that impinging on the detector when a patient is being imaged and to reduce the dependence of the measurements on the particularities of the x-ray source used. The filter is placed as close as possible to the focal spot to reduce the contribution of scattered radiation to the acquired images.

In the past, a variety of beam qualities have been used by investigators, most notably 70 kVp with 0.5-mm Cu filtration (11) and 70–120 kVp with 19-mm Al filtration (12–14). However, when comparing the performance of different detectors, it is helpful to use similar x-ray beams. Recently, prompted by a new initiative by the International Electrotechnical Commiss-

Radiographic Techniques Used for the Evaluation of Detector Performance							
Relevant Clinical Application	IEC Alias	Nominal Peak Kilovoltage (kVp)	Filtration (mm)*	Half-Value Layer (mm)*	IEC Values†	Ideal SNR ² (mm ⁻² mR ⁻¹)	Energy-weighted‡
Mammography	RQN-M	28 ± 1	BEM, 45.0§	NA	NA	NA	NA
Neonatal, pediatric, extremities	RQA3¶	~50	Al, 10.0	Al, 4.0 ± 0.1	190,826	175,992	172,704
General radiography, extremities, head, shoulder	RQA5¶	~70	Al, 21.0	Al, 7.1 ± 0.1	264,626	255,232	248,931
		70	Cu, 0.5	NA	NA	248,836	242,053
		70	Al, 19.0	NA	NA	251,393	244,806
General radiography, fluoroscopy	RQC¶	70–80	Cu, 1.5–2.0	Cu, 0.5 ± 0.1	NA	289,340#	285,098#
General radiography	RQA7¶	~90	Al, 30.0	Al, 9.1 ± 0.1	283,815	282,889	274,133
Chest radiography	RQT¶	~120	Al, 22.0	Al, 10.4 ± 0.1	NA	272,240	256,102
		115	Al, 19.0	NA	NA	272,054	256,260
		120	Al, 19.0	NA	NA	270,619	253,785
General radiography, chest	RQA9¶	~120	Al, 40.0	Al, 11.5 ± 0.1	272,545	273,548	260,467
High-energy applications	RQA10¶	~150	Al, 45.0	Al, 12.8 ± 0.1	NA	248,633	231,946
		150	Al, 19.0; Cu, 1.0	NA	NA	245,919	230,776

Note.—The IEC techniques are fully described in an IEC standard document (17). NA = not available.

*Filtration quality, >99.9% purity.

†Converted from the IEC document (16), using an 8.77- μ Gy/mR conversion factor.

‡Values computed for a typical high-frequency x-ray beam, tungsten target, 12° anode angle, 2.5-mm Al intrinsic filtration plus the specified added filtration, using xSpect x-ray simulation routine (13).

§IEC specifies the technique for a Mo target with 0.03-mm (\pm 0.002) Mo intrinsic filtration and percent ripple of less than 4%. BEM = breast equivalent material made of 50% adipose and 50% glandular tissue.

¶IEC specifies the technique for a tungsten target and intrinsic tube filtration equivalent to 2.5-mm Al at 75 kVp.

#Computed for 75 kVp, 1.5-mm Cu.

sion (IEC) (15,16), the use of certain standard beam quantities for characterization of detector performance has become popular. The Table (13,16,17) lists the definition of some of the beam qualities used for detector characterization, including those of the IEC.

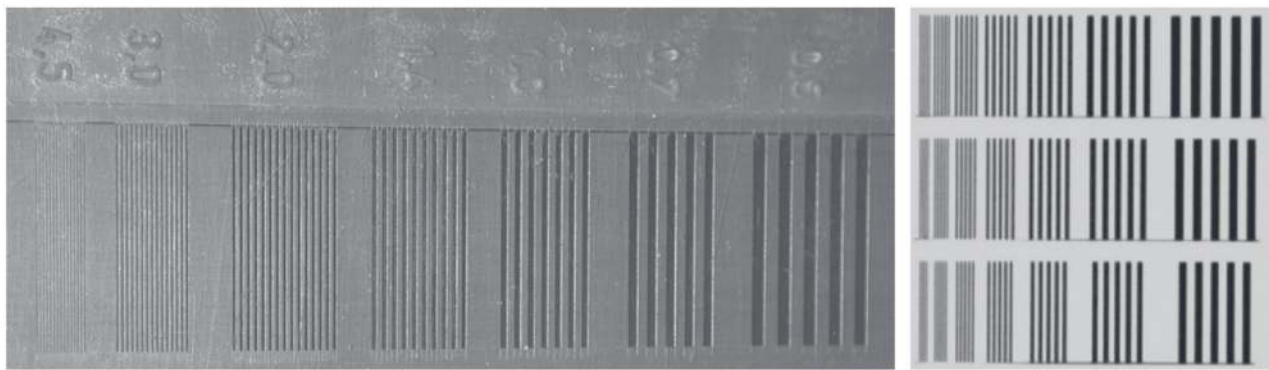
Another prerequisite for assessing the performance of a digital detector is its flat-field calibration. Digital detectors are susceptible to inherent nonuniformities, dead pixels, and pixel-to-pixel sensitivity differences, which are discussed further in the next chapter. To correct for such nonuniformities, most digital detectors employ nonuniformity (eg, offset and gain) calibrations (12,14). Often, these calibrations are done with an antiscatter grid in place, while the assessment methods outlined subsequently are often used with the grid removed. Furthermore, sometimes the detector may have additional or protective covers or may be integrated within a Bucky unit or table with a certain level of x-ray absorption. The presence of additional absorptive layers does affect the noise performance of the detector. Therefore, it is imperative that (a) a detector is calibrated according to the guidelines of the manufacturer for the imaging setup with which

it will be evaluated (eg, no grid, specific covers used) before the evaluation is initiated, and (b) the setup is reported along with the results of the evaluation.

Finally, the system should be able to output image data in a linear and raw format; that is, the pixel values should be linearly proportional to exposure, and no processing (other than nonuniformity and pixel defect calibrations) should have been applied to the image data. If the linearity and processing requirements are not met but the data can be converted to a linear format and the processing steps “undone,” the data may still be used for the sharpness and noise assessments. If unaccounted for, however, the computations required for those assessments will violate the required underlying theoretical basis for the assessments.

Sharpness Assessment Methods

Three notable methods have been developed to assess the sharpness performance of digital radiographic systems. In all of these methods, an image of a sharp test object is first acquired. The three methods are distinguished on the basis of the type of test object used: bar pattern, slit, or edge. The sharpness of the system



a.

b.

Figure 5. (a) Bar-pattern test object. (b) Digital radiograph of another bar-pattern test object.

is then assessed, usually in terms of the MTF, from the level of blur in the acquired image. The test object is often imaged in contact with the detector front cover by using a small focal spot and a large source-to-image distance to reduce the contribution of focal spot blur to the detector characterization. Furthermore, to make the measurements independent of the sampling inherent in a digital detector, the test object is often positioned with a small angle with respect to the pixel array of the detector. The angulation allows sampling of the image data at a pitch finer than that of the detector pixellation (by means of the different relative placements of the object with respect to the detector array), thus obtaining the so-called presampled MTF.

The image is acquired by using the desired beam quality, as discussed previously, but often with exposures notably higher than those used clinically, in order to reduce the level of noise in the measurement. The high exposure level is justified because the sharpness of digital detectors is usually not dependent on exposure. When the MTF depends on exposure, multiple images of the object may be averaged to obtain the MTF estimate, a method sometimes used to improve the accuracy of the results (particularly for the definition of the tails of the line spread function in the slit method).

The bar-pattern assessment method, as the name implies, is based on the use of a bar-pattern test object. Such test objects are made with a relatively thin layer of high-atomic-number metals (eg, Pb) covering a range of discrete frequencies (Fig 5). These test objects are commercially available in multiple thickness and frequency ranges. After acquisition, the image of the bar pattern is processed to deduce the square-wave response function at each of the spatial frequencies of the pattern by averaging the data over the length of the associated bar patterns. The MTF is then mathematically deduced from the square-wave response function (18). The advantages of the bar-pattern method include (*a*) the relative ease and speed of implementation and (*b*) conceptual simplicity. However, the method suffers from low precision,

noise, and coarse sampling of an otherwise continuous MTF.

The slit assessment method has been one of the traditional methods to measure the MTF. The slit test object is often made of two thick pieces of metal (often 2-mm-thick pieces of Pb) held at a precise distance from each other, forming a slit opening between them with a width of tens of microns (often 10 μm) (Fig 6). The object is aligned precisely with the beam and the detector, and one or multiple images are acquired at high exposures. The location of the slit in the acquired image is determined, and the image data along the slit are averaged to form the line spread function, from which the MTF is deduced by Fourier transformation (11).

The advantages of the slit method include (*a*) high precision, particularly at high spatial frequencies (19), and (*b*) the acceptance of the method as an established method to measure the MTF. The disadvantages include the need for the precise alignment of the slit device, which makes the measurement complicated and time-consuming. Furthermore, the method suffers from noise in the tails of the line spread function, necessitating the use of high or multiple exposures, and, more importantly, the extrapolation of the tails of the line spread function, which imposes an *a priori* function on and reduces the precision of the low-frequency component of the MTF.

The edge assessment method has also been one of the established methods to measure the MTF but has recently gained more popularity for the performance assessment of digital radiographic systems. The edge test object is made of a relatively thin metal foil, one side of which is polished to achieve a sharp, straight, and smooth edge (Fig 7). The foil should be made of a high-atomic-number material and should be thick enough to maximize attenuation and minimize secondary radiation yet thin enough to minimize alignment sensitivity. Previously, lead, platinum-iridium alloys, and tungsten have been used to make edge objects ranging in thickness from 0.1 to 1 mm (20–22).



Figure 6. (a) Slit test object. (b) Magnified view of the slit opening ($10 \mu\text{m}$ wide), showing slight nonuniformities. (Image courtesy of James T. Dobbins III, PhD, Duke University Medical Center, Durham, NC.) (c) Digital radiograph of the object, averaged over 12 separate acquisitions, used for the assessment of the MTF. (Image courtesy of John Yorkston, PhD, Rochester, NY.)

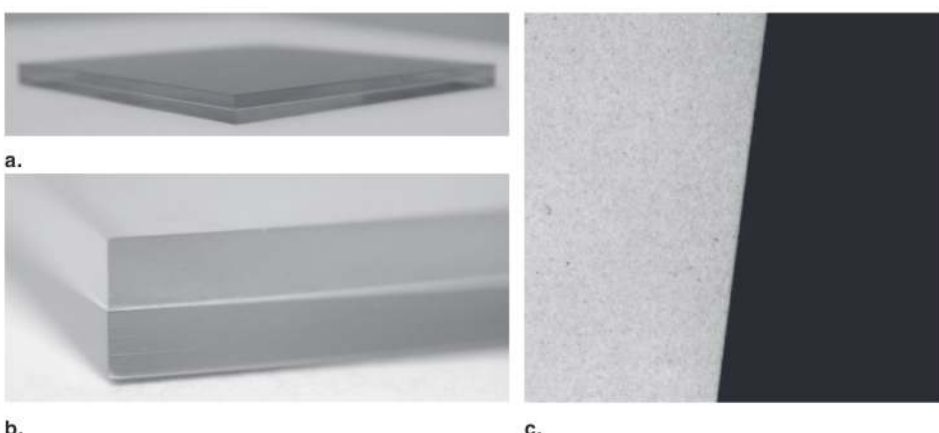


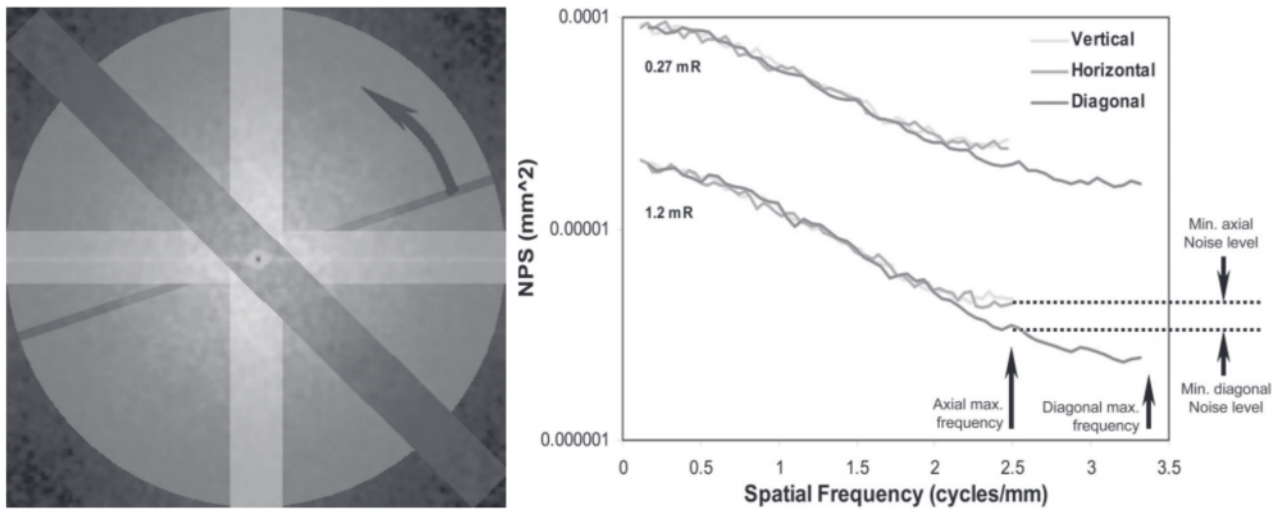
Figure 7. (a) Precise polished edge test object. (b) Magnified view of the metal edge laminated between two slabs of polymerized methyl methacrylate. (c) Digital radiograph of the object used for the assessment of the MTF.

The object is aligned with the beam and the detector, but a precise alignment is not required because the method is less susceptible to misalignment. The image data along the edge image are averaged to form the edge spread function. The edge spread function is differentiated and subjected to further Fourier transformation to obtain the line spread function and the MTF (21).

The advantages of the edge method include (a) high precision, particularly at low spatial frequencies (19), (b) simplicity, and (c) speed of data acquisition (ie, alignment). The disadvantages of the method include (a) its susceptibility to noise caused by the differentiation process and (b) less precision at high spatial frequencies (19). Noise in the edge measurement method can be reduced by proper exposure and by modest

smoothing of the edge spread function data. An accurate, relatively precise, simple, and convenient method, the edge method has now been endorsed as the standard method for measuring the MTF of digital radiographic systems (15).

The assessment methods described in the preceding paragraphs provide the MTF estimate at only one location and only in one direction, perpendicular to the orientation of the test object. If the sharpness of a detector is suspected to be different in different areas of the detector, the MTF may be measured in different areas (eg, center and corners). Rotating the object also provides one-dimensional MTF estimates along different orientations. The MTF is often measured in two near-axial directions. Because the MTF is an inherently two-dimensional function, newer methods have been



a.

b.

Figure 8. (a) Methods of band averaging. (b) Resultant NPS for a digital radiographic system. The diagonal band averaging provides noise estimates beyond the cutoff frequency associated with the axial sampling. The estimates are also less affected by noise aliasing. The radial NPS (not shown) lies between the axial and diagonal estimates.

proposed that are based on disk (23) and multiple-hole (24,25) test objects for the assessment of the two-dimensional MTF in a single image acquisition. However, because the MTF of most digital radiographic detectors is nearly rotationally symmetric, these newer methods have not gained popularity.

Noise Assessment Methods

Two methods have previously been used to characterize the NPS of radiographic detectors. The one-dimensional moving-slit method has commonly been used in the past to characterize the NPS of analog screen-film systems. However, for the performance assessment of a digital radiographic system, the slit method has largely been replaced by a two-dimensional Fourier analysis method. This method is based on first acquiring uniform (flat-field) images at the desired beam qualities and exposures. The exposure to the detector should be measured precisely, free-in-air, because the exposure dependence of the noise magnitude is one of the important characteristics of digital detectors reflected in the DQE. In the most common implementation of the technique, the image is segmented into multiple small regions. The size of the regions is often in the neighborhood of 25 × 25 mm. Possible large-scale nonuniformities within and between regions are often removed by subtraction methods (9,26) because such nonuniformities are often not characterized as noise.

The NPS from each individual region is estimated by Fourier transformation. These spectra are appropriately filtered, normalized, and averaged to obtain the two-dimensional NPS (9). To obtain a smooth estimate of the NPS, a large number of regions often must be used. The regions can be segmented from a single uniform ra-

diograph, as stated previously, or can be taken from an ensemble of radiographs. Finally, one-dimensional traces through the two-dimensional NPS are obtained by orthogonal, diagonal, or radial band averaging of the two-dimensional spectrum (Fig 8) (20).

SNR and DQE Assessment Methods

The SNR performance of a digital radiographic detector is most commonly characterized in terms of the NEQ and the DQE. The NEQ is computed from the measured MTF and NPS as follows: $NEQ(f) = G^2 \cdot MTF^2(f)/NPS(f)$, where the gain term, G , is either (a) estimated from the mean area pixel value of the detector at the exposure at which the NPS is measured (11), or (b) otherwise set to unity if the NPS computations include proper normalization (9).

As noted previously, although the NEQ gives a direct indication of target detectability at a given exposure level, it is dependent on exposure. The DQE, as the ratio of the NEQ to SNR^2_{ideal} , provides an exposure-independent measure of detector performance in the absence of nonquantum sources of noise. To be able to compute the DQE, the ideal SNR^2 per exposure (SNR^2_{ideal}/E) should be known, from which SNR^2_{ideal} can be determined by multiplying by the exposure associated with the NEQ (and the original NPS). The SNR^2_{ideal}/E quantity is either obtained from tabulated values for specific beam qualities (11,15) or is otherwise estimated by computational modeling (9). Furthermore, two "types" of ideal SNR^2 have been used: (a) the counting type, which assumes an ideal detector behaves as a perfect x-ray photon counter; or (b) the energy-weighted type, which assumes an ideal detector behaves as a perfect x-ray photon energy integrator (13). The values for the two types of ideal SNR^2

show about a 3%–5% difference, depending on the peak kilovoltage. As the asymmetry of the x-ray spectrum increases at high peak kilovoltages, so does the difference. The Table provides the values of the two types of $\text{SNR}^2_{\text{ideal}}/E$ for some typical beam qualities.

OTHER DETECTOR PERFORMANCE FACTORS

Although sharpness, noise, and SNR response are considered the key performance characteristics of digital radiographic detectors, these factors do not encompass all of the important performance characteristics. Other notable performance factors include scatter sensitivity, dynamic range, veiling glare, spatial artifacts, temporal artifacts, and temporal stability. Specific quantification and testing procedures may be devised to evaluate the performance of the detector in terms of these characteristics. Because the main focus of this chapter is sharpness and noise, these factors are only briefly discussed in the subsequent paragraphs.

Scatter Sensitivity

The conventional sharpness, noise, and SNR assessment methods concern only the primary beam and do not include the contribution of scattered radiation to the image quality. In those methods, the filtration elements are placed as close as possible to the focal spot, essentially eliminating any scattered radiation in the recorded images. If the Bucky unit of the detector is equipped with an antiscatter grid, the grid is also removed because the methods aim to assess the detector performance independent of auxiliary equipment. However, in normal clinical use with a grid, the grid attenuates part of the primary beam. Systems that use strategies other than an antiscatter grid to reduce scattered radiation (eg, slot-scanning) are naturally not affected by this primary beam loss.

In clinical practice, scattered radiation is an ever-present component of radiographic imaging, markedly affecting the quality of the image. The scattered radiation reduces subject contrast and affects the level of noise within the image. The effect varies for different detectors because of the difference in the spectral sensitivity of various capture element materials used in the detector. Furthermore, from an imaging system perspective, the effect of the scattered radiation is dependent on the specifics of the methods used to reduce scattered radiation, such as slot-scanning, air gaps, or antiscatter grids. Thus, the performance of a radiographic system without scatter and without a grid does not fully represent the noise and DQE performance of the system in actual clinical usage and can create biases in comparing the performance of different imaging systems. An overall performance assessment of a digital radiographic detector should include scatter sensitivity, taking into consideration the whole acquisition system, including the detector and the antiscatter element.

The scatter assessment may be made with a phantom (placed close to the detector) with scattering properties similar to those of actual patients. The measurement is dependent on the phantom, the technique, and the geometry of the acquisition, all of which should either be standardized (for comparing intrinsic performance of different systems) or otherwise be representative of the clinical usage of the system. The primary method used to measure scattered radiation is the beam stop method (27). In this method, small opaque disks (often made of lead) are placed on the tube side of the phantom, and two images are acquired with and without the disks. The ratio of the image signals in the projected areas of the disks, with and without the disks present, provides an estimate of the scatter fraction (ie, the ratio of scatter to scatter plus primary). Disks placed at different areas of the image provide estimates of the scatter fraction as a function of location. Currently, there is no established method to measure the noise contribution of the scattered radiation.

Veiling Glare

Veiling glare is a known image degradation process in the image formation caused by broad spreading of the scanning laser beam (in computed radiography) or secondary energy carriers (in other digital radiographic detectors) in the detector material, which leads to a drop in the zero or near-zero spatial frequency response propagated through the entire frequency range. Because this process affects the modulation (or contrast) response of the detector, it is reasonable to expect veiling glare to be a part of the sharpness assessment of the detector in terms of the MTF.

However, MTF assessment methods have limited accuracy at low frequencies because of the limited size of the region of interest used to measure the MTF and the noise in the tails of the line spread function. MTF normalization is, in fact, one of the steps in conventional MTF measurements, practically eliminating any veiling glare from the measured MTF. However, the veiling glare can be measured by using a method similar to the beam stop method used for scatter measurements described in the preceding text (28). The only difference is that no scattering medium (ie, phantom) is present, thus allowing an accurate estimate of the scatter within the detector (ie, veiling glare). Glare ratio may be calculated as the ratio of the image signals in the projected area of the disk, with and without the disk present.

Dynamic Range

Dynamic range is the useful range of exposures within which a detector can record images with an acceptable quality. The assessment of the detector performance in terms of noise and the DQE over a wide range of exposures tests the system performance at discrete points within its dynamic range. However,

it is useful to determine the extremes of exposure between which the detector may be used reliably, by using the associated large-area signal and noise response of the detector. The dynamic range can be calculated as the ratio of the exposure associated with the detector saturation (eg, exposure that gives a pixel value of 4,095 in a 12-bit detector) to that associated with a minimum pixel value above the noise threshold of the detector, assuming a minimum threshold SNR² in the 3–5 range (29).

Spatial Artifacts

All digital detectors are susceptible to pixel dropouts or point defects caused by dust specks (in computed radiography) or by nonlinear or defective pixel elements (in flat-panel detectors and detectors that are based on a charge-coupled device [CCD] or a complementary metal oxide semiconductor [CMOS]) (Fig 9). Neighborhood pixel-averaging methods are used to effectively reduce such artifacts if the locations of the defects are known and if the number and proximity of the defective pixels are within a limited range. Spatial artifacts may also be seen in digital detectors that are comprised of multiple tiled subpanels or tiled CCDs; these artifacts are seen as faint seam lines between the subpanels or CCDs. Although various strategies have been devised to reduce or eliminate these artifacts, such as pixel averaging, and gain and offset corrections, the artifacts may still appear under certain circumstances, especially at high exposures. Similarly, a computed radiographic detector may exhibit pixel jitter or spatial nonlinearity artifacts caused by laser scan nonuniformities. Because detector spatial artifacts are highly dependent on the technology, their assessment methods should focus on characterizing possible artifacts associated with the type of detector being tested.

Temporal Artifacts

Some digital radiographic detectors exhibit lag artifacts in the form of residual signals from previous acquisitions that appear in subsequent images (30). Lag artifacts can be due to (a) incomplete erasure of the image detector (in the case of computed radiography) or (b) residual memory effects in amorphous silicon or the capture element (in the case of flat-panel detectors and CCD- or CMOS-based detectors). In the flat-panel and the CCD- or CMOS-based detectors, the residual signal fades with a finite time constant. The amount of residual signal at a given time depends on the time lapse from the prior exposure. Thus, in applications in which image acquisition is rapid (eg, fluoroscopy or multiple-view acquisitions), strategies have been devised to reduce the effect. Two common strategies are (a) subtracting a fraction of the prior image from the subsequent image or (b) performing an offset correction between two image acquisitions (if there is sufficient time between the two acquisitions). The magnitude of lag artifact and the effectiveness of its reduction

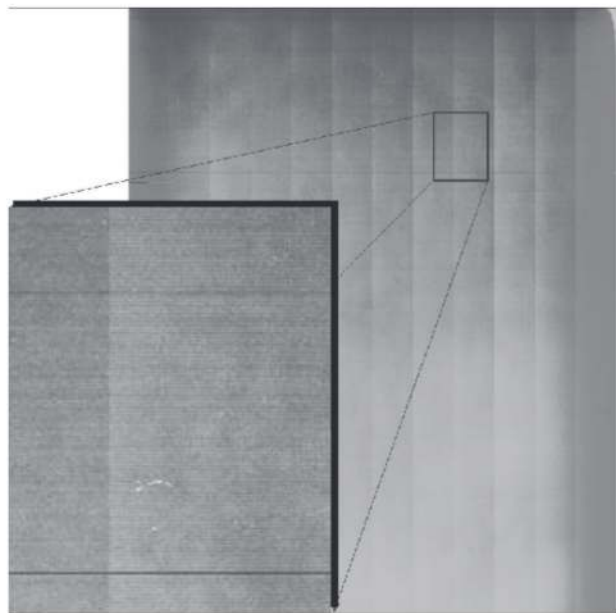


Figure 9. Contrast-enhanced uncorrected uniform image from a flat-panel digital detector, illustrating various structured noise patterns.

methods can be characterized by measuring the time constant of the fading of the signal after acquisition of a high-exposure image of a high-contrast object.

Temporal Stability

Even though a detector may behave perfectly at the time of testing, its performance may vary over time. Variations might be due to (a) normal deteriorations (eg, mechanical changes or changes in the scanning or erasure components in computed radiography) or (b) susceptibility to environmental conditions such as temperature, if the temperature of the electronic components is not well regulated. Thus, there is a need to ensure that the performance of a detector is stable over time. To do so, a quality control program may be implemented within which the detector characteristics most susceptible to change are tracked over time. Many detector manufacturers offer quality control tools with their products that may be used for this purpose. However, because the quality control testing methods might be simpler and more limited than those used in more comprehensive evaluations, it is important to perform the quality control tests at the same time as the comprehensive evaluations to establish benchmark performance levels for tracking over time.

SUMMARY

The performance of a digital radiographic detector can be described in terms of various performance metrics. Among them, sharpness and noise are most commonly equated with the intrinsic performance of digital radiographic detectors. The MTF, the NPS, the NEQ, and the

DQE are meaningful measures of sharpness and noise for digital radiographic detectors. Extensive methods have been developed to measure these quantities. The measurements can readily be used for the design of new detectors and for optimization, testing, and comparison of existing ones.

Acknowledgment: The author thanks many colleagues for intellectual contributions and helpful discussions regarding materials presented in this chapter.

References

- Rossmann K. Point spread-function, line spread-function, and modulation transfer function: tools for the study of imaging systems. *Radiology* 1969; 93:257–272.
- Rossmann K. Spatial fluctuations of x-ray quanta and the recording of radiographic mottle. *Radiology* 1963; 90:863–869.
- Giger ML, Doi K. Investigation of basic imaging properties in digital radiography. I. Modulation transfer-function. *Med Phys* 1984; 11:287–295.
- Barrett HH, Swindell W. Radiological imaging: the theory of image formation, detection, and processing. New York, NY: Academic Press, 1981.
- Dobbins JT III. Effects of undersampling on the proper interpretation of modulation transfer function, noise power spectra, and noise equivalent quanta of digital imaging systems. *Med Phys* 1995; 22:171–181.
- Samei E, Flynn MJ, Eyler WR. Detection of subtle lung nodules: relative influence of quantum and anatomic noise on chest radiographs. *Radiology* 1999; 213:727–734.
- Samei E. Effects of anatomical structure on signal detection. In: Van Metter RL, Beutel J, Kundel HL, eds. Handbook of medical imaging: physics and psychophysics. Vol 1. Bellingham, Wash: SPIE, 2000; 655–682.
- Dobbins JT III. Image quality metrics for digital systems. In: Van Metter RL, Beutel J, Kundel HL, eds. Handbook of medical imaging: physics and psychophysics. Vol 1. Bellingham, Wash: SPIE, 2000; 161–222.
- Flynn MJ, Samei E. Experimental comparison of noise and resolution for 2k and 4k storage phosphor radiography systems. *Med Phys* 1999; 26:1612–1623.
- Rose A. The sensitivity performance of the human eye on the absolute scale. *J Opt Soc Am* 1948; 38:196–208.
- Dobbins JT III, Ergun DL, Rutz L, Hinshaw DA, Blume H, Clark DC. DQE(f) of four generations of computed radiography acquisition devices. *Med Phys* 1995; 22:1581–1593.
- Samei E. Image quality in two phosphor-based flat panel digital radiographic detectors. *Med Phys* 2003; 30:1747–1757.
- Samei E, Flynn MJ. An experimental comparison of detector performance for computed radiography systems. *Med Phys* 2002; 29:447–459.
- Samei E. Image quality in two phosphor-based flat panel digital radiographic detectors. *Med Phys* 2003; 30:1747–1757.
- Hoeschen D. DQE of digital x-ray imaging systems: a challenge for standardization. *Proc SPIE* 2001; 4320:280–286.
- International Electrotechnical Commission. Medical electrical equipment: characteristics of digital x-ray imaging devices. I. Determination of the detective quantum efficiency. Publication no. IEC 62220-1. Geneva, Switzerland: International Electrotechnical Commission, 2003.
- International Electrotechnical Commission. Medical diagnostic x-ray equipment: radiation conditions for use in the determination of characteristics. Publication no. IEC 1267. Geneva, Switzerland: International Electrotechnical Commission, 1994.
- Borasi G, Nitrosi A, Ferrari P, Tassoni D. On site evaluation of three flat panel detectors for digital radiography. *Med Phys* 2003; 30:1719–1731.
- Cunningham IA, Reid BK. Signal and noise in modulation transfer function determinations using the slit, wire, and edge techniques. *Med Phys* 1992; 19:1037–1044.
- Samei E, Flynn MJ. An experimental comparison of detector performance for direct and indirect digital radiography systems. *Med Phys* 2003; 30:608–622.
- Samei E, Flynn MJ, Reimann DA. A method for measuring the presampled MTF of digital radiographic systems using an edge test device. *Med Phys* 1998; 25:102–113.
- Granfors PR, Aufrechtig R. Performance of a 41X41-cm² amorphous silicon flat panel x-ray detector for radiographic imaging applications. *Med Phys* 2000; 27:1324–1331.
- Reimann DA, Jacobs HA, Samei E. Use of Wiener filtering in the measurement of the two-dimensional modulation transfer function. *Proc SPIE* 2000; 3977:670–680.
- Bath M, Sund P, Mansson LG. Method for determining the two-dimensional presampling modulation transfer function in digital radiography. *Proc SPIE* 2001; 4320:268–279.
- Fetterly KA, Hangiadreou NJ, Schueler BA, Ritenour ER. Measurement of the presampled two-dimensional modulation transfer function of digital imaging systems. *Med Phys* 2002; 29:913–921.
- Floyd CE Jr, Warp RJ, Dobbins JT III, et al. Imaging characteristics of an amorphous silicon flat-panel detector for digital chest radiography. *Radiology* 2001; 218:683–688.
- Jordan LK III, Floyd CE Jr, Lo JY, Ravin CE. Measurement of scatter fractions in erect posteroanterior and lateral chest radiography. *Radiology* 1993; 188:215–218.
- Seibert JA, Nalcioglu O, Roeck WW. Characterization of the veiling glare PSF in x-ray image intensified fluoroscopy. *Med Phys* 1984; 11:172–179.
- Yaffe MJ, Rowlands JA. X-ray detectors for digital radiography. *Phys Med Biol* 1997; 42:1–39.
- Zhao W, DeCrescenzo G, Rowlands JA. Investigation of lag and ghosting in amorphous selenium flat-panel x-ray detectors. *Proc SPIE* 2002; 4682:9–20.

Performance of Digital Radiographic Detectors: Factors Affecting Sharpness and Noise¹

Digital radiography (DR) systems are replacing analog systems in many clinical applications. Broadly speaking, DR can be defined as projection x-ray imaging in which the image data are sampled into discrete elements in the spatial and intensity dimensions. Initially, image data are captured by the x-ray capture element of the detector, in a process similar to that used by analog (ie, screen-film) radiographic systems. The captured analog signal is then transformed into digital form through the processes of sampling and quantization. The digital image data are finally transferred to a computer and processed for display and distribution.

DR detectors vary dramatically with respect to the technologies on which they are based. However, these detectors all share three distinct components: the x-ray capture element, the coupling element, and the collection element. Figure 1 illustrates these elements and lists them for the most common DR detectors. The performance of digital detectors and the quality of their acquired images are directly related to various physical processes that take place in these elements during image formation.

The previous chapter described assessment methods for characterizing the performance of DR detectors, focusing mainly on sharpness and noise, two key factors often equated with the intrinsic performance of these detectors (1–3). This chapter focuses on the factors that affect the sharpness and noise characteristics of digital detectors, organized with respect to the three key detector elements described previously. This chapter further provides a quantitative summary of the sharpness and noise performance of current commercially available DR systems on the basis of experimental measurements.

SHARPNESS FACTORS IN DR SYSTEMS

As mentioned in the previous chapter, the sharpness of an image is related to (a) the intrinsic sharpness of the detector employed; (b) subject contrast, as determined by object characteristics, beam quality, and scatter, as well as the blur caused by the finite size of the x-ray focal spot; and (c) patient motion during the acquisition. Because this chapter focuses on detector performance, only the detector-related factors are discussed.

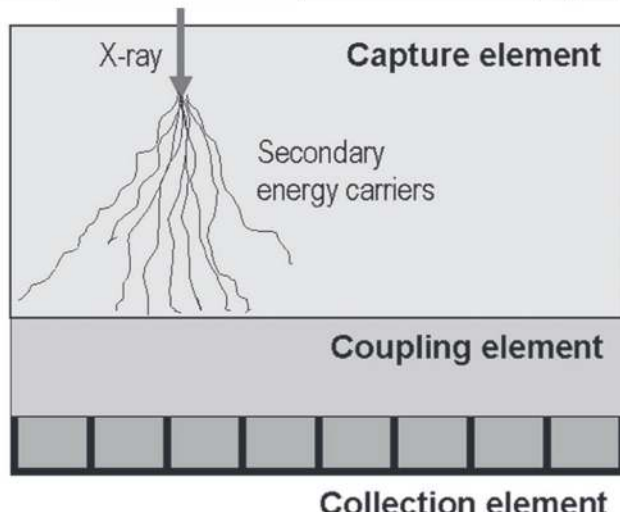
Multiple factors affect the sharpness of DR detectors. The factors can be categorized in terms of the three components of DR detectors: the capture element, the coupling element, and the collection element (Fig 1).

Advances in Digital Radiography: RSNA Categorical Course in Diagnostic Radiology Physics 2003; pp 49–61.

¹From the Departments of Radiology, Physics, and Biomedical Engineering, DUMC Box 3302, Duke University Medical Center, Durham, NC 27710 (e-mail: samei@duke.edu).

Figure 1. Three fundamental elements of DR systems.

Detector Technology	Typical capture element	Typical coupling element	Collection element
CR	PSL phosphor (e.g., BaFBr)	PSL light-guide	Photo-multiplier tube; signal digitization
CCD/CMOS-based	CsI or G ₂ O ₂ S phosphor	Lens or fiber-optic taper	CCD or CMOS
Indirect flat panel	CsI or G ₂ O ₂ S phosphor	Contact layer	Photodiode /TFT array
Direct flat panel	a-Se	None	TFT array
Electrostatic	a-Se	Induction space	Electrometer probes; signal digitization



Capture Element Blur

Blur in the capture element of DR detectors occurs through two different processes during image formation. First, the energy of x-ray photons can be dissipated by scattering, fluorescence, or photoelectric interactions within the detector causing all or part of the energy to be deposited somewhere in the detector other than the original point of entry. This can cause a blur (as well as noise) within the acquired image. In most DR detectors, the magnitude of this blur is notably lower than that of the other sources of blur described in the following paragraphs.

The second blur process affecting the capture element involves the scattering of secondary energy carriers that are generated when the energy of the x-ray photons is absorbed by the sensitive layer of the detector (Fig 2a, 2b). In phosphor-based detectors, these secondary energy carriers are visible photons generated as a result of the x-ray photon interaction with the phosphor material (eg, CsI, Gd₂O₂S). In direct flat-panel detectors, the secondary energy carriers are the electronic charges (electrons and holes) generated when the x-ray photons interact with the photoconductor (eg, amorphous selenium).

Computed radiography (CR) is an exception to the process described in the preceding paragraph because the blur in the capture element occurs not from scattering of the photostimulable luminescence (PSL), but rather from the scattering of the

laser beam used to stimulate the phosphor material (Fig 2c). Furthermore, there is an additional source of blur in CR detectors caused by the movement of the laser beam during the scanning process. The emission of photostimulable light is not prompt. Instead, it occurs with a finite decay on the order of microseconds. This causes a "lag" in the photostimulable emission as the laser beam rapidly scans the phosphor screen, which slightly reduces the modulation transfer function (MTF) in the laser scan direction, as illustrated in Figure 3 (4).

The capture element blur is negligible for direct flat-panel detectors because charge dissipation is practically eliminated by the application of an electric field (5). However, the capture element blur is the dominant source of blur in phosphor-based detectors. This blur can be reduced with a number of strategies. First of all, reducing the thickness of the sensitive layer can markedly reduce the blur (4). This is due to the fact that in thinner screens, light has less volumetric space for scattering. Figure 4 illustrates that reduction in terms of improved MTF for a CR detector. However, the drawback to this strategy is that the reduced thickness causes a reduction in the efficiency of the detector in detecting the x-rays, which causes an increase in image noise and a decrease in the detective quantum efficiency (DQE).

Notable advances in the reduction of capture element blur have come from the use of structured

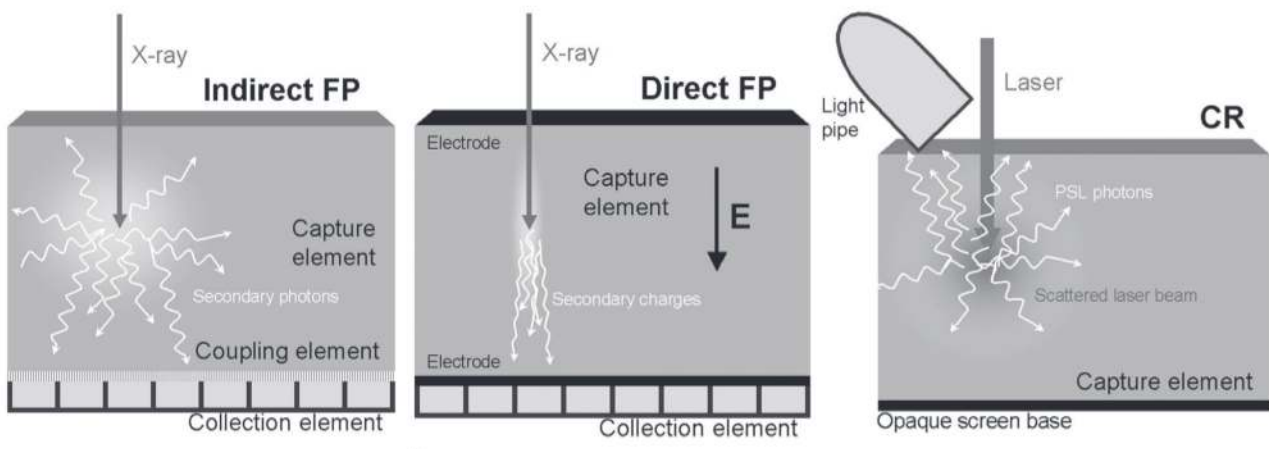


Figure 2. Schematic cross sections of (a) an indirect flat-panel detector, (b) a direct flat-panel detector, and (c) a CR detector, illustrating the generation of secondary energy carriers in the capture elements of the detectors. E = electric field, FP = flat panel, PSL = photostimulable luminescence.

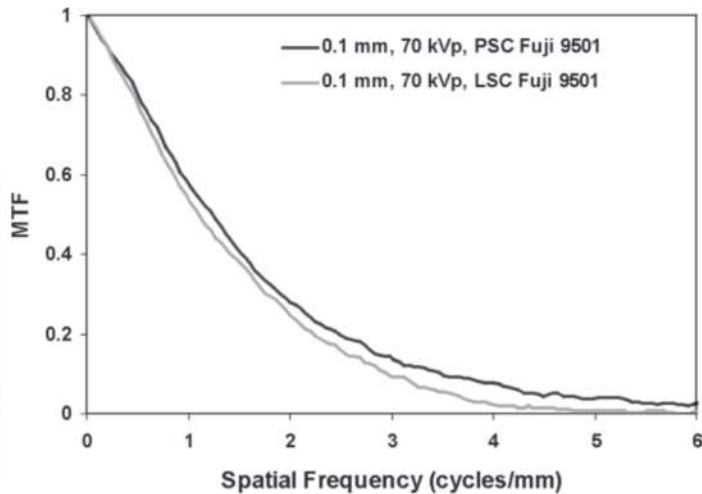
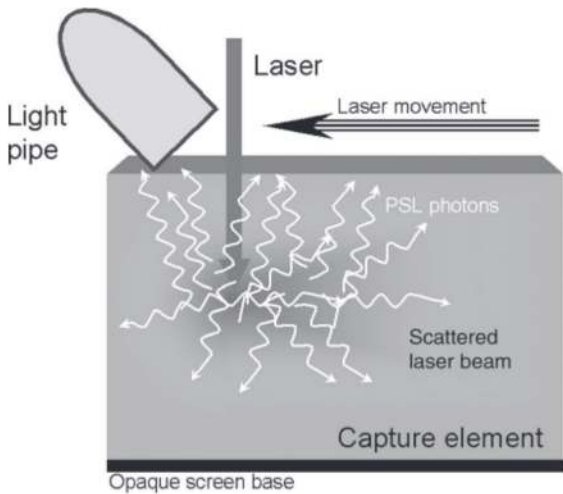


Figure 3. (a) Schematic cross section of a CR screen, illustrating the lag in the generation of PSL signal in the laser scan direction. (b) Lag leads to a reduction of the MTF in the laser scan (*LSC*) direction compared with the plate scan (*PSC*) direction (Fuji 9501-HQ, ST-Va screen, 0.1-mm pixel size, 70 kVp with 19-mm added Al filtration).

phosphors in DR detectors. Conventional phosphor screens used in imaging are turbid in nature, made of phosphor particles suspended (glued) within a layer of binding material. In this form, the screen scatters a large amount of light, whether (a) that due to x-ray interaction in phosphor-based detectors, flat-panel detectors or detectors that are based on a charge-coupled device (CCD) or complementary metal oxide semiconductor (CMOS), or (b) that due to the interrogating laser beam in CR detectors. Growing the phosphor material in a needlelike structure (the needles being perpendicular to the screen surface) reduces the lateral scattering of light photons, as illustrated in Figure 5. This needlelike structure of the phosphor has enabled the development of digital detectors with thicker phosphors that have superior DQE and noise performance and with sharpness better than or at least

equivalent to those made of turbid phosphors (6). Figures 6a and 7a illustrate the MTFs of two indirect flat-panel detectors and two CR detectors with turbid and structured phosphors. In both detectors, the structured phosphor layer is at least 2.5 times thicker than the turbid phosphor layer.

In terms of asymmetry of the sharpness in the CR detectors, the limiting factor is the system throughput because the photoluminescence decay responsible for additional blur in the laser scan direction limits the speed at which the screen can be scanned. Recent progress in the development of line-scanning technology (described in the chapter by Ralph Schaetzing, PhD) has enabled a more rapid acquisition of image data from the CR screen, one line at a time, thus notably increasing the readout speed without undue effects on sharpness.

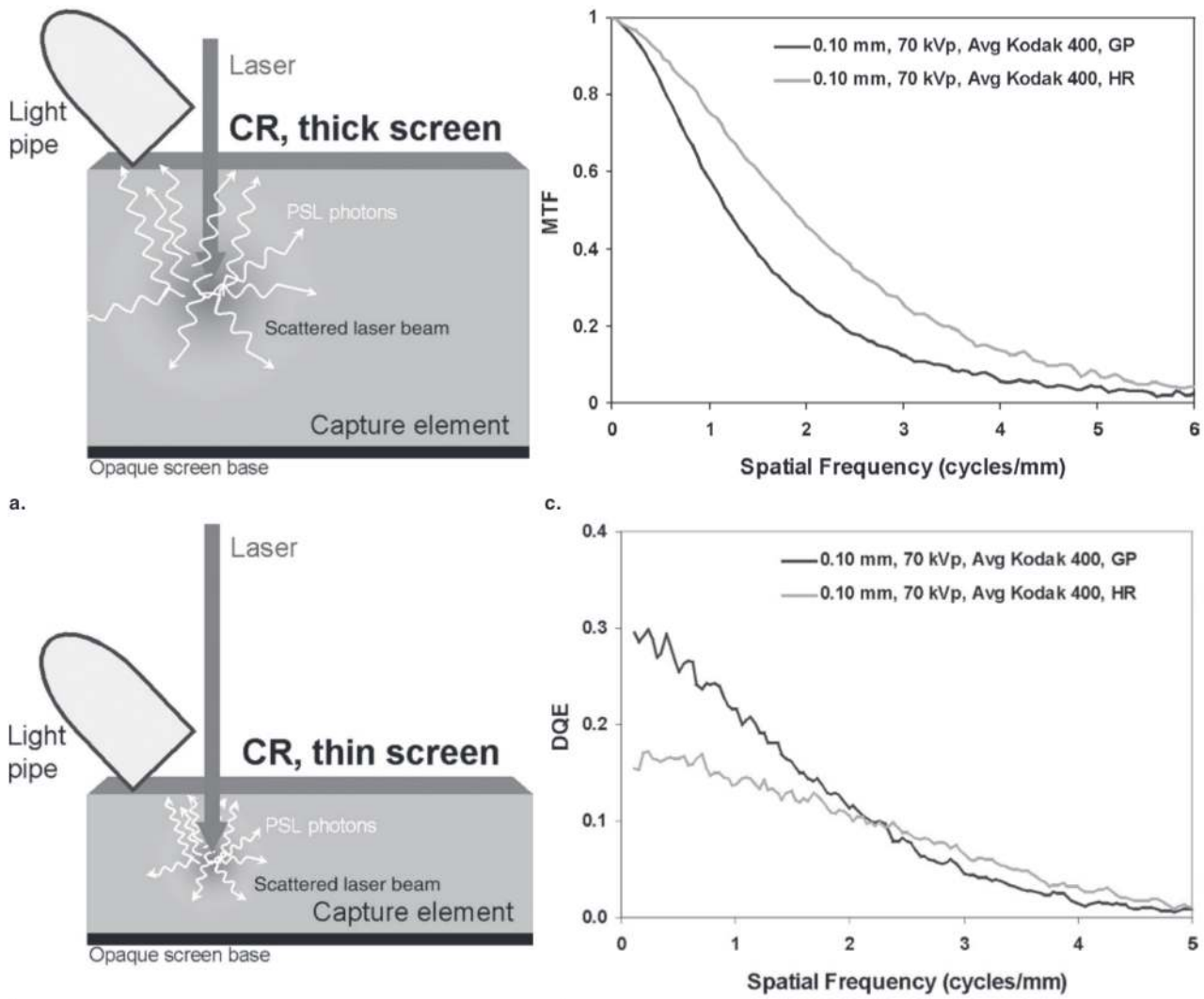
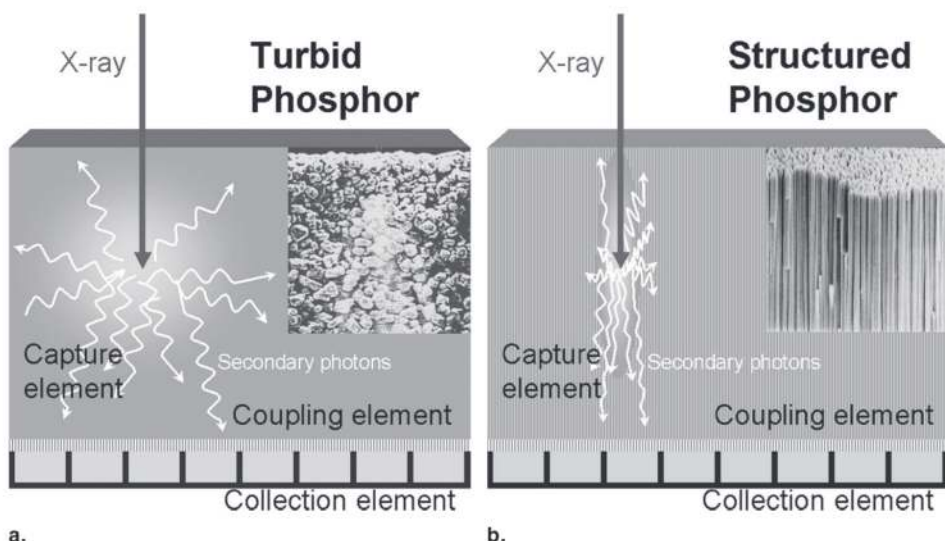


Figure 4. Schematic cross sections of (a) a thick CR screen (Kodak GP) and (b) a thin CR screen (Kodak HR), illustrating the effect of screen thickness on laser scattering. The thin screen produces (c) higher MTF, with (d) an associated loss in the DQE, especially at low to mid spatial frequencies (Kodak CR-400 reader, 0.1-mm pixel size, 70 kVp with 19-mm added Al filtration).

Figure 5. Schematic cross sections of an indirect flat-panel detector with (a) turbid phosphor and (b) structured phosphor screens as the capture element.



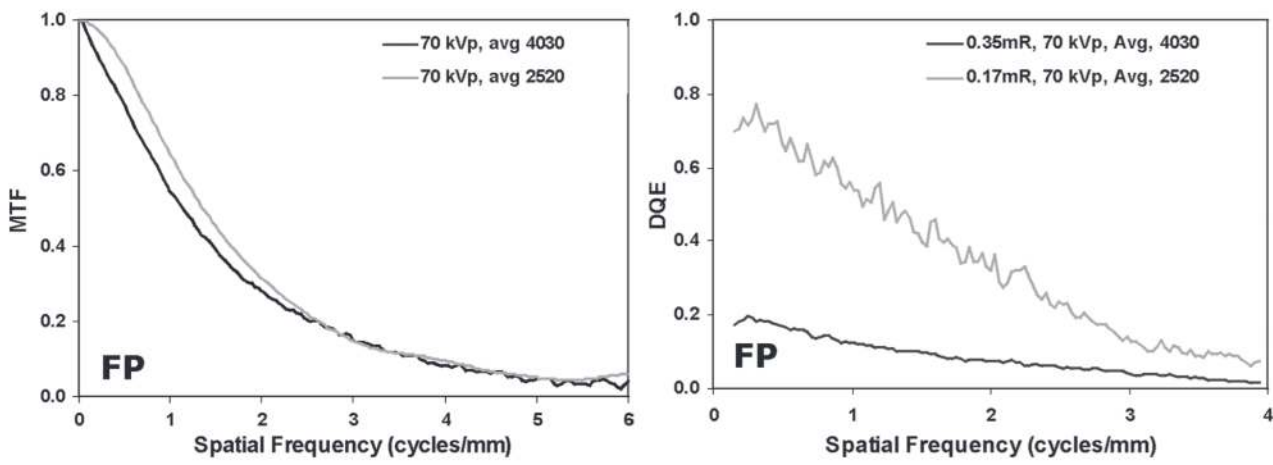


Figure 6. (a) MTF and (b) DQE of two identical indirect flat-panel detectors (Varian 4030 and 2520 detectors, 0.127-mm pixel size), one with a turbid phosphor screen (Lanex Regular, 4030) and one with a structured phosphor screen (600- μ m CsI, 2520) as the capture element (70 kVp with 19-mm added Al filtration). FP = flat panel.

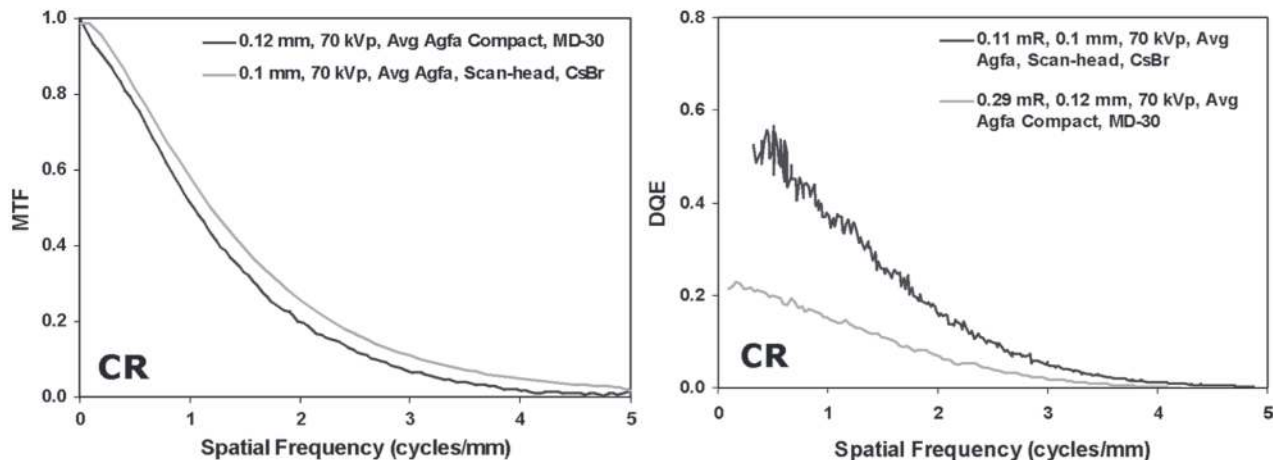


Figure 7. (a) MTF and (b) DQE of two CR detectors (Agfa ADC-Compact reader, 0.12-mm pixel size; and Agfa Scan-head prototypic reader, 0.1-mm pixel size), one with a turbid phosphor screen (Agfa MD-30) and one with a structured phosphor screen (Agfa prototypic CsBr screen) (70 kVp with 19-mm added Al filtration). (Structured phosphor CR data courtesy of Ralph Schaetzling, PhD, Greenville, SC.)

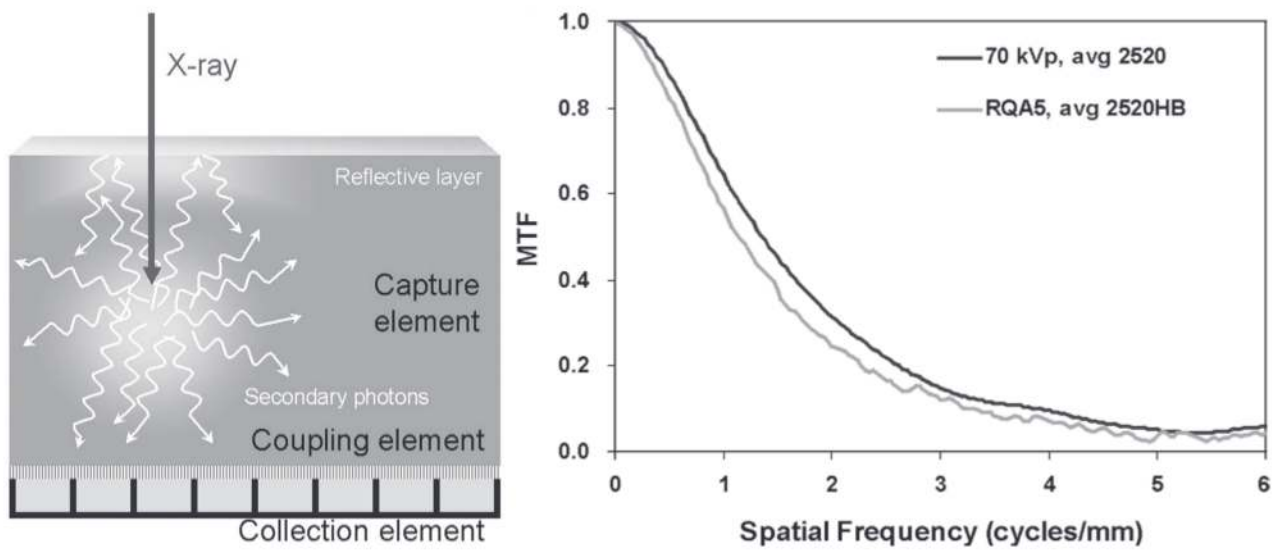
Coupling Element Blur

Sharpness loss may also occur from the coupling element of the detector. This loss occurs because of spreading of the secondary energy carriers (light or charge) emerging from the capture element before being collected by the collection layer. This form of blur is often not an issue in direct flat-panel detectors because charge dissipation is highly controlled by an imposed electric field, unless additional blur is intentionally introduced for other purposes (eg, reduction of noise aliasing) (7). Coupling element blur is also often not an issue for CR because CR sharpness is not dependent on the scattering of the emerging photostimulable photons. However, other phosphor-based DR systems, particularly lens-coupled CCD- and CMOS-based detectors, are potentially susceptible to this sharpness loss. In

these detectors, the sharpness response of the lens system has a direct effect on the overall sharpness of the detector (see Figs 14b, 15a). The sharpness of indirect flat-panel detectors may also be affected by the choice of the coupling material, as illustrated in Figure 8.

Collection Element Blur

Blur at the collection layer affects all types of digital detectors and serves as a fundamental limitation on achieving the maximum possible sharpness. This limitation is directly dictated by the finite size of the image elements (ie, the pixels). The Nyquist sampling theorem states that a digital system with a pixel size, p , cannot represent features with spatial frequencies higher than the cutoff (Nyquist) frequency, $1/2p$ (8). In the case of an ideal digital detector with no spatial



a. b.

Figure 8. (a) Schematic cross section showing effect of addition of a reflective layer to an indirect flat-panel detector. (b) Effect of additional reflective layer on the MTF (Varian 2520 detector, 0.127-mm pixel size, 70 kVp with 19-mm added Al filtration; and Varian 2520 high-bright [HB] detector, 0.127-mm pixel size, RQA5 technique).

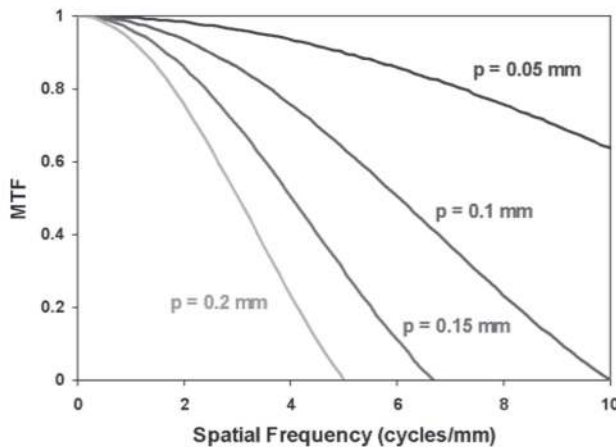


Figure 9. Maximum theoretical MTF for DR systems based on the pixel aperture size (p).

energy dissipation, the response of each pixel would be represented by an ideal rect function, a square aperture function with a value of unity within the spatial extent of the pixel and a value of zero elsewhere. The presampled MTF for such a detector will be the Fourier transform of a rect function, namely a sinc function, that goes to zero at $1/p$. Thus, theoretically, the presampled MTF of a digital system cannot exceed $\text{sinc } p$. Figure 9 illustrates the limiting MTF sinc functions for a variety of pixel sizes.

In popular technologies, and even in the scientific realm, the matrix size or the pixel size of a digital imaging device is often equated with its resolution or sharpness performance. However, this notion is only partly true because it only pertains to the collection element and does not include the other elements re-

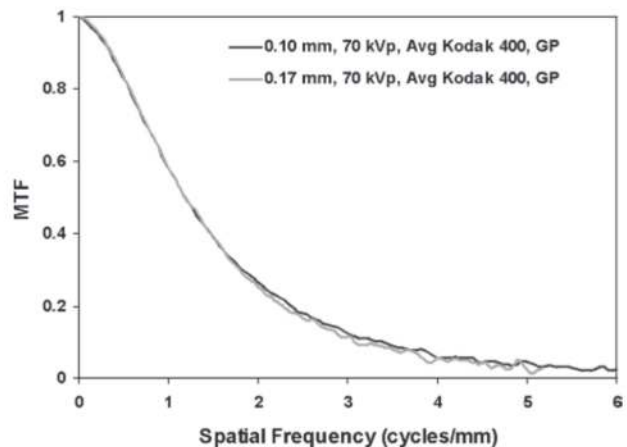


Figure 10. MTF of a CR detector (Kodak CR-400, GP screen) measured with 0.10-mm and 0.17-mm pixel size (MTFs in the laser scan and plate scan directions averaged, 70 kVp with 19-mm added Al filtration).

sponsible for the sharpness performance of the device. As noted previously, the Nyquist cutoff frequency is only the maximum theoretical frequency that can potentially be reproduced by sampling but is not representative of what the device can actually deliver. In digital detectors in particular, the dominant source of blur is often not the collection element. In most phosphor-based detectors, the capture element blur is much more dominant. Figure 10, for example, illustrates that the reduction of pixel size from 0.17 mm to 0.10 mm has only a slight (if any) effect on the presampled MTF from the detector. Thus, in detectors in which capture or coupling element blurs are dominant, further reduction of pixel size has only a marginal effect on the MTF.

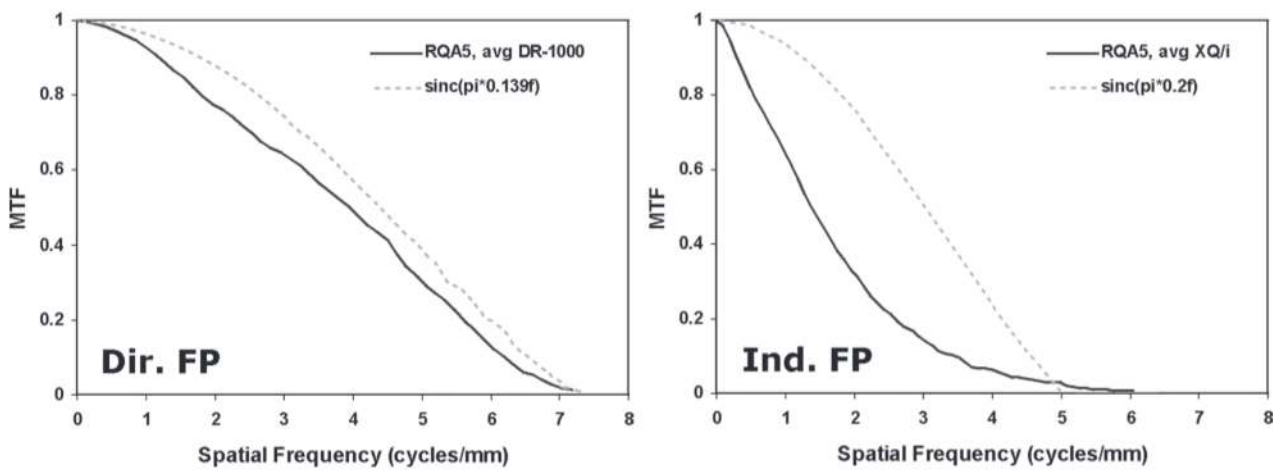
**a.**

Figure 11. MTFs of (a) a direct flat-panel detector (DRC/Hologic DR-1000, 0.139-mm pixel size) and (b) an indirect flat-panel detector (GE XQ/i, 0.2-mm pixel size), with their corresponding maximum theoretical limits (dashed lines) based on the pixel aperture size (RQA5 technique). *FP* = flat panel.

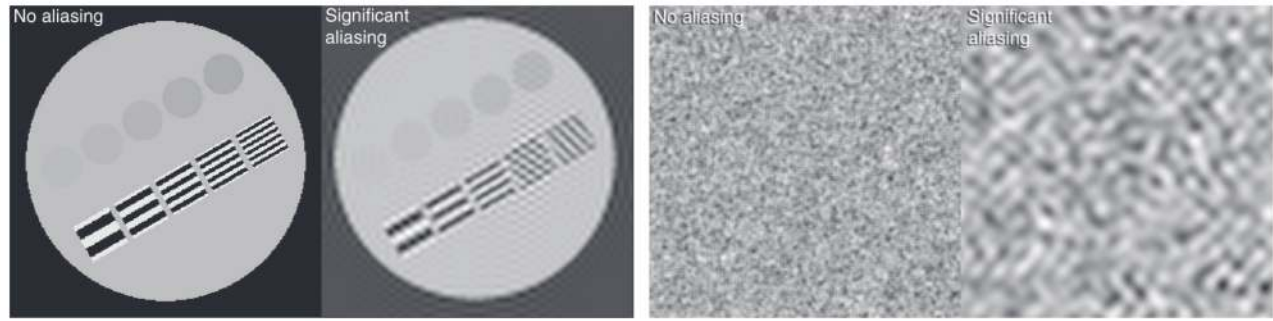
b.**a.**

Figure 12. Effect of aliasing on (a) signal and (b) noise. (Images courtesy of David M. Gauntt, PhD, Birmingham, Ala.)

In contrast to phosphor-based detectors, as noted previously, capture and coupling element blurs are negligible for direct flat-panel detectors. In those detectors, the collection element is thus the dominant source of blur. Figure 11 illustrates the MTFs of a direct and an indirect flat-panel detector in comparison with their associated limiting MTFs. The MTF of the direct system is nearly identical to that of the ideal sinc. The small difference may be attributed to backscattered fluorescent x-rays generated in the glass substrate of the detector, leading to a slight sharpness loss (9).

The high MTF of the direct flat-panel detectors has a direct implication in terms of signal and noise aliasing (10). Signal aliasing can occur if there is considerable power in the input signals to the detector at spatial frequencies higher than the cutoff frequency of the detector. Such signals would be shifted to lower frequencies, causing signal artifacts, as illustrated in Figure 12. The same process can take place for noise, causing higher-frequency noise components to be shifted to lower frequencies. Because of notable noise aliasing, the noise power spectra

for direct detectors are relatively flat, emulating white noise, as compared with the noise power spectra from phosphor-based detectors (Fig 13) (11). Specific detector designs have been suggested to somewhat reduce the sharpness of direct detectors and thus reduce the potential for signal and noise aliasing (7). However, the clinical effect of aliasing on specific clinical tasks has not yet been substantiated.

NOISE AND DQE FACTORS IN DR SYSTEMS

Generally speaking, radiographic noise in DR systems is composed of two types: (a) quantum noise caused by the limited number of photons forming the image and (b) instrumentation noise added by the additional statistically random and fixed processes underway in the detector during image formation. Similar to sharpness, the factors that affect the noise and DQE performance of DR detectors can be categorized in terms of the three components of the DR detector noted previously, namely, the capture element, the coupling element, and the collection element (Fig 11).

Capture Element Noise

Quantum noise and part of the instrumentation noise (conversion noise) are directly related to the capture element of the DR detector. Quantum noise is caused by the finite number of x-ray quanta forming the image. Conversion noise is due to the fluctuations in the number of secondary energy carriers generated per detected x-ray photon. Initially uncorrelated, both quantum noise and conversion noise produce a poorly correlated noise pattern within the image. The contribution of the capture element noise to these sources of noise can be formulated as follows.

In a radiographic system, the signal (S) from the detector is proportional to the number of x-ray photons used to form the image (N_0), the efficiency of detection (η), and the detector gain (g). Assuming Poisson processes, the signal, noise, and signal-to-noise ratio (SNR) for such a detector can be expressed as

$$S = N_0 \eta g, \quad (1)$$

$$\sigma_q^2 = N_0 \eta (g^2 + \sigma_g^2), \quad (2)$$

$$\text{SNR}^2 = N_0 \eta \frac{1}{1 + \sigma_g^2/g^2}, \quad (3)$$

where σ_q^2 is the image variance, and σ_g^2 is the variance associated with the detector gain (5). For detectors with multiple gain processes, the previous expressions can be expanded to include all of the gain factors and their associated fluctuations (12). In these expressions, the $N_0 \eta$ term represents the quantum noise, while the $g^2 + \sigma_g^2$ term and the σ_g^2/g^2 term represent the gain or conversion noise, a part of the instrumentation noise component.

As the SNR relationship in Equation (3) implies, the quantum noise in a DR system can be improved by using two means. Increasing radiation exposure increases N_0 and in turn improves the SNR and the noise equivalent quantum (NEQ). This improvement, however, is independent of the detector performance; the improvement in SNR is linearly proportional to an increase in the $\text{SNR}_{\text{ideal}}$, keeping the detector DQE constant. The SNR cannot readily be used to compare different detectors because its value is dependent on the exposures used. The SNR of two detectors may only be meaningfully compared for a constant radiation exposure and $\text{SNR}_{\text{ideal}}$.

The second way to improve the SNR is by improving the capture efficiency (η) of the detector. Capture efficiency can be improved by increasing either the atomic number or the thickness of the capture element, or both. Higher-atomic-number elements have a higher absorption coefficient for x-ray detection, which leads to a higher probability of interaction of incident x-rays

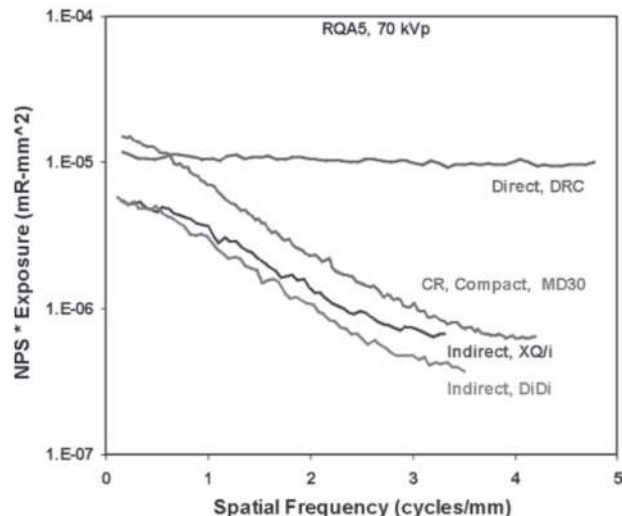


Figure 13. Exposure-scaled noise power spectra (NPS) of a direct flat-panel detector (DRC/Hologic DR-1000), two indirect flat-panel detectors (GE XQ/i and Philips Digital Diagnost [DiDi]), and a CR detector (Agfa ADC-Compact, MD-30 screen) at comparable exposures (RQA5 technique).

in the capture element, improved DQE and SNR, and reduced noise. The history of radiographic imaging shows a constant struggle to use higher-atomic-number capture media in radiographic detectors, from CaWO_4 to $\text{Gd}_2\text{O}_2\text{S}$ and CsI (in phosphor-based detectors), and from amorphous selenium to HgI_2 and CdZnTe (in photoconductor-based detectors). The challenge has been the ability to reproducibly manufacture these materials with high enough quality and in a large enough size for a commercial product.

Increasing the thickness of the capture element is another means to increase the efficiency of x-ray detection and reduce quantum noise. Figure 4d shows the DQE from two CR screens. The thicker screen has notably higher DQE, particularly at frequencies of less than 2 cycles/mm. However, as Figure 4c shows, that improvement comes with a marked reduction in the MTF. The associated loss in image sharpness has proved the primary limiting factor in improving the detector DQE and reducing noise by increasing capture element thickness. For a given detector, increasing the capture element thickness increases the DQE at the expense of reduced sharpness (MTF), particularly in phosphor-based detectors. The recent deployment of structured phosphors in these detectors has had a favorable effect on this trade-off, enabling increased capture element thickness and DQE, with MTFs equal to or better than those of thinner turbid phosphor detectors (6). Figures 6b and 7b illustrate the DQE improvements that are possible with the use of structured phosphors in indirect flat-panel and in CR detectors with even a slight improvement in the MTF (Figs 6a, 7a).

The gain or conversion noise is an important contributor to the overall image noise. This noise is intro-

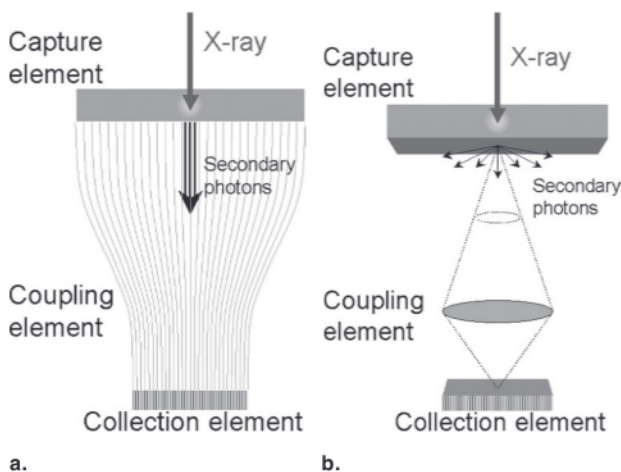


Figure 14. Schematic diagrams of a CCD- or CMOS-based DR detector with (a) fiberoptic coupling or (b) lens coupling.

duced by the statistical fluctuations in the number of generated (and collected) energy carriers that are produced when the energy of the x-ray photons is captured by the detector. As indicated previously, the secondary energy carriers are either (a) visible photons, in the case of phosphor-based detectors, or (b) electronic charges (electrons and holes) in direct flat-panel detectors. However, these are not the only energy carriers in the image formation process. Image formation often involves a chain of energy conversions in which energy carriers of one type are converted to another. The number of quanta involved at each stage determines the level of conversion noise at that stage. Ideally, the number of intermediate quanta should always be much higher than that of the detected x-ray photons in the capture element. If the number of carriers at any stage of the image formation process falls to less than that number, conversion noise can become more influential than quantum noise, a phenomenon commonly known as a secondary quantum sink (10,13).

Conversion noise can be reduced by generating and collecting more secondary energy carriers, leading to improved DQE. On the generating front, more efficient (higher-gain) production of secondary carriers improves the conversion noise. For example, both brighter phosphor screens in indirect flat-panel detectors and also higher-intensity scanning laser beams (balanced with increased laser scatter) in CR detectors would provide a higher number of generated and collected photons per detected x-ray, thus potentially improving the DQE. Furthermore, a smaller number of conversion stages would reduce conversion noise. From that standpoint, direct flat-panel detectors are potentially less susceptible to conversion noise than indirect flat-panel detectors because the former detectors require no light-to-charge conversion. Improved collection of the secondary energy carriers as a means to reduce conversion noise is discussed in the follow-

ing two sections, "Coupling Element Noise" and "Collection Element Noise."

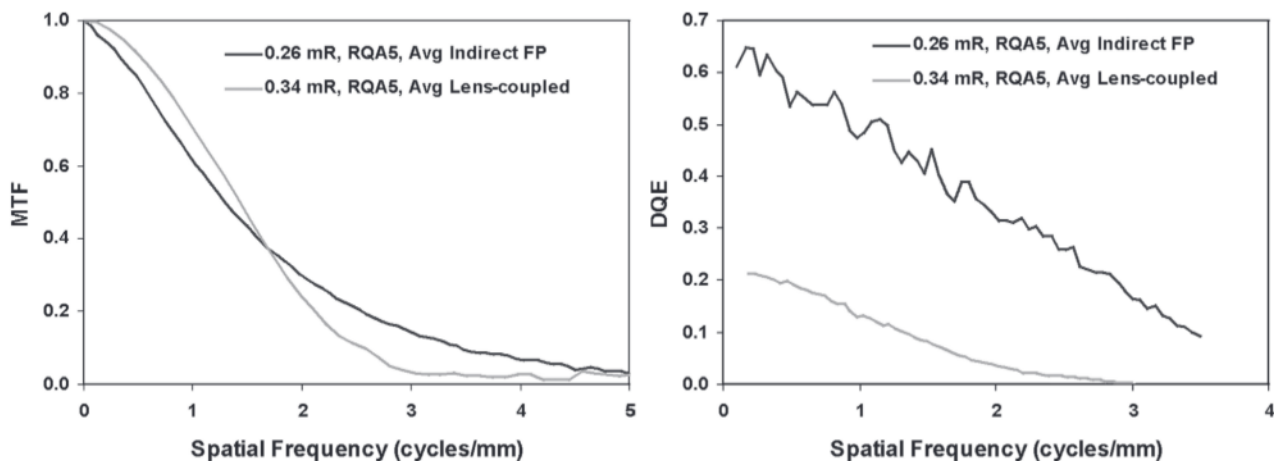
Coupling Element Noise

The coupling element noise is directly related to the efficiency with which secondary energy carriers are channeled from the capture element to the collection element. The dispersion or absorption of these carriers either in the bulk of the capture element or in the coupling element reduces their numbers, thus adding to the conversion noise. Improved optical coupling can thus improve the detector DQE. For example, in CCD- and CMOS-based detectors, a fiberoptic coupling (Fig 14a) provides a somewhat wider acceptance angle of incoming photons compared with a lens coupling (Fig 14b), which potentially improves the DQE of the detector. However, in both types of coupling, a large number of light photons generated in the phosphor screen are lost because they fall outside of the acceptance solid angle of the coupling element due to demagnification in the image formation process (14,15), which leads to a marked reduction in the number of detected light photons, potentially even to a secondary quantum sink. Figure 15 illustrates the magnitude of DQE improvement that can be achieved (at approximately equivalent sharpness) by direct coupling of the phosphor to the collection element with no intermediate lens system.

In CR devices, efforts have been made to continuously improve the channeling of the PSL light to the collection elements by increasing the acceptance solid angle of the light guide, even by using microlenses in the most recent designs. Another efficient method for PSL light detection has also been introduced for reduced conversion noise and improved DQE. In this method, instead of collecting the PSL light from only one side of the screen, light is collected from both sides with the use of a transparent screen support and a second light guide, as illustrated in Figure 16. The two images are then added together to form the final image. This method can notably improve the DQE, as illustrated in Figure 16b, especially at lower frequencies. The improvement at higher frequencies is limited by the blurriness of the "back" image caused by notably higher dispersion of the light photons that reach the back light collector.

Collection Element Noise

Collection element noise is composed of multiple components. The first component relates to the efficiency with which secondary energy carriers are detected by the collection element and, as such, is part of the conversion noise introduced previously. Matching the absorption efficiency of the collection element (eg, the spectral absorption) to the characteristics of the secondary carriers (eg, the wavelength of the light



a.

Figure 15. (a) MTF and (b) DQE of a lens-coupled CCD-based DR detector (0.167-mm pixel size) compared with an indirect flat-panel DR detector (0.143-mm pixel size) (RQA5 technique). Both detectors employ a 500- μm -thick CsI layer as the capture element. FP = flat panel.

photons) is one obvious design consideration to reduce collection element noise and conversion noise. A second design consideration is the extent of the sensitive area of the collection element. In flat-panel and in CCD- and CMOS-based detectors, not all of the “real estate” of a collection pixel is sensitive to the incoming light. The ratio of the sensitive area to the actual area of a pixel is known as the fill factor.

High fill factors are desirable to reduce collection noise and conversion noise. Fill factors of modern DR systems commonly range between 50% and 100%. In current indirect flat-panel technology, the minimum area required for pixel transistors serves as a fundamental limitation on achieving high fill factors, especially for small pixels. This limitation has direct implications for small-pixel mammographic and low-dose fluoroscopic applications of these panels. In direct flat-panel detectors, the secondary charge created by x-rays in the photoconductor material can be directed away from insensitive areas of the pixel by added local electric fields, achieving effective fill factors approaching 100%.

Additive electronic noise is another noise component in DR systems. Electronic noise is due to background fluctuations in electronic signals or to fluctuations in the readout process. It is often dominant at low exposures, leading to a drop in the DQE at low exposure values. This noise source has been one of the obstacles in real-time fluoroscopic application of digital solid-state detectors. Methods to reduce electronic noise include improved electronics and both passive and active cooling of the detector.

Structured noise is another type of unwanted “signal” in DR that can have an effect on diagnosis. This noise is due to (a) detector-response nonuniformities, (b) variations in pixel-to-pixel sensitivity and linearity, and (c) dead pixels. Structured noise often mani-

fests itself as a “fixed” spatial pattern superimposed on the image data. Because of its static nature, structured noise is markedly different from the other statistical noise sources described previously. As such, from a purely statistical standpoint, structured noise might perhaps not be considered to be true “noise.” Nevertheless, if noise is defined as any unwanted image details that interfere with the diagnostic task, structured noise definitely exerts a negative influence and thus, from a perceptual standpoint, should be considered noise and should be included in the assessment of detector noise and the DQE.

Structured noise is a dominant source of noise for DR detectors at high exposures, again leading to a drop in the DQE, as illustrated in Figure 17 (6,11). The DQE can be improved by improving the uniformity of the capture element. To further reduce structured noise, most DR systems use some form of detector-specific nonuniformity correction as part of the preprocessing. In flat-panel and in CCD- and CMOS-based detectors, such corrections are made by using offset and gain calibrations. Because the magnitude and characteristics of structured noise in these detectors may vary over time, the corrections may need to be repeated on a frequent basis. In CR, because the screens are interchangeable, the corrections are only applied to reduce nonuniformities associated with the scanning and light-collection processes. These preprocessing methods are further described in the next chapter.

CURRENT PERFORMANCE LEVELS

The performance levels of current commercial DR and mammographic systems are highly dependent on the radiographic techniques and on the methods used to determine the performance. Because the methods

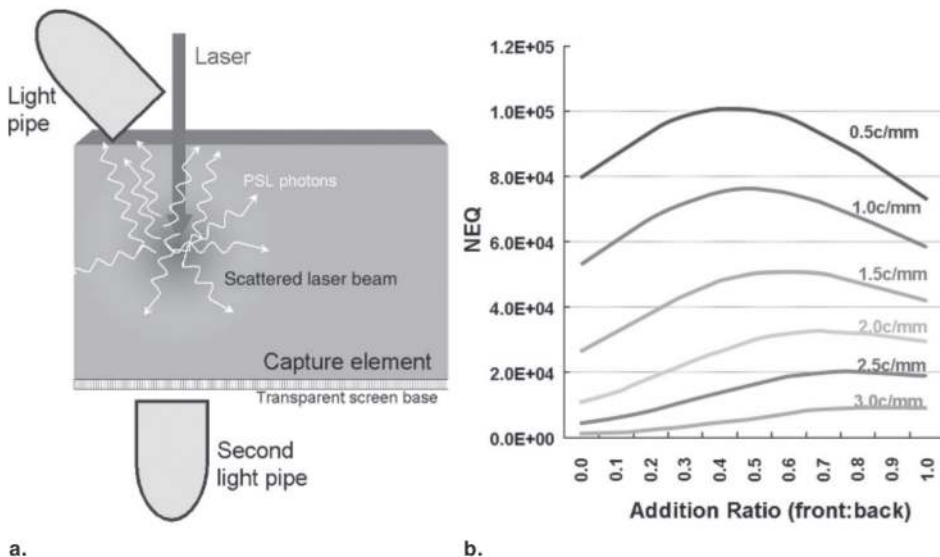


Figure 16. (a) Schematic cross section of a double-sided CR detector, in which the PSL signal is collected from both sides of a screen with a transparent base. (b) Noise equivalent quanta (*NEQ*) as a function of front-to-back addition ratio of the two generated CR images at multiple spatial frequencies. *c* = cycles. (Image b courtesy of Robert A. Uzenoff, BS, Stamford, Conn.)

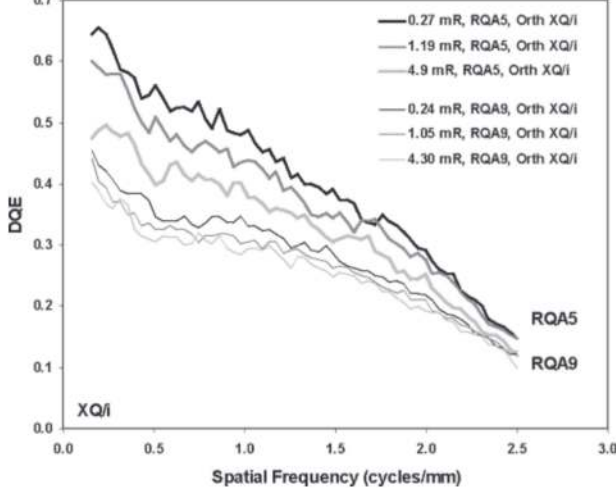


Figure 17. DQE of an indirect flat-panel detector (GE XQ/I, 0.2-mm pixel size) at multiple exposures with RQA5 technique (top three graph lines) or RQA9 technique (bottom three graph lines).

have not been fully standardized, it is often difficult to compare the performance of two systems that are evaluated by two different laboratories. Identical methods are a prerequisite for direct comparison of different systems.

Table 1 summarizes the MTF and DQE responses of some common commercial CR detectors used in radiographic applications, as measured in studies undertaken by the author. Identical methods were used in the studies. In general, current CR systems behave somewhat similarly, exhibiting 0.2 and 0.1 MTF values at frequency ranges of 1.9–2.3 cycles/mm and 2.6–3.3 cycles/mm, respectively. The DQEs of CR systems are also somewhat similar except at high frequencies. At 70 kVp, the DQEs range from 20% to 30% at 0.15 cycles/mm and from 2.5% to 7.8% at 2.5

cycles/mm. Corresponding DQEs at 115 kVp are 15%–23% at 0.15 cycles/mm and are 2%–6% at 2.5 cycles/mm. An exception to these similarities is the high-resolution CR screens, which offer improved high-frequency sharpness response (0.2 and 0.1 MTF at 3.5 and 4.7 cycles/mm) at the expense of a lower low-frequency DQE (17% at 0.15 cycles/mm at 70 kVp). A second exception is the new structured phosphor CR screen with line-scan technology, which can produce DQEs approaching those of flat-panel detectors at comparable sharpness.

Table 2 similarly summarizes the MTF and the DQE responses of some common commercial flat-panel detectors used in radiographic applications, which have been evaluated with identical methods. The indirect flat-panel detectors exhibit similar sharpness response with 0.2 and 0.1 MTF values at frequency ranges of 2.5–2.6 cycles/mm and 3.5–3.9 cycles/mm, respectively. The MTFs are modestly higher than those of conventional CR systems. The MTF of the only direct flat-panel detector that is listed exhibits superior response with 0.2 and 0.1 MTF at 5.6 and 6.2 cycles/mm, respectively.

In terms of the DQE, the CsI-based flat-panel detectors also exhibit similar response, with values ranging from 60% to 64% at 0.15 cycles/mm and from 15% to 24% at 2.5 cycles/mm (at ~70 kVp, RQA5 technique). Corresponding DQEs at approximately 120 kVp (RQA9 technique) are 45%–54% at 0.15 cycles/mm and 12%–20% at 2.5 cycles/mm. The differences at higher frequencies are mostly due to the pixel pitch of the detectors. These DQEs are markedly higher than those of a turbid phosphor-based indirect detector tested, which shows a performance (19% at 0.15 cycles/mm at ~70 kVp) similar to that of conventional CR. The only direct flat-panel detector that is listed exhibits lower DQE at lower frequencies (38% at 0.15

Table 1
MTF and DQE Performance of Some Commercial CR Detectors at 70 and 115 kVp with 19-mm Added Al Filtration

CR Reader	CR Screen	Frequency (mm^{-1}) at Specified MTF		Percent DQE at 70 kVp at Specified Frequency		Percent DQE at 115 kVp at Specified Frequency	
		0.1 MTF	0.2 MTF	0.15 mm^{-1}	2.5 mm^{-1}	0.15 mm^{-1}	2.5 mm^{-1}
Agfa ADC-Compact	Agfa MD-10	2.8	2.1	20.3	3.8	15.9	3.8
Agfa ADC-Compact	Agfa MD-30	2.6	2.0	22.9	4.1	18.5	3.7
Agfa ADC-Solo	Agfa MD-10	2.9	2.2	24.6	4.6	21.5	4.1
Agfa ADC-Solo	Agfa MD-30	2.7	1.9	28.6	4.9	21.8	3.5
Lumisys CR-2000	Lumisys MD-10	2.6	2.0	22.2	2.5	15.3	1.8
Fuji FCR-9501(HQ)	Fuji ST-Va	3.2	2.3	30.0	6.6	23.1	5.2
Kodak CR-400	Kodak GP-25	3.3	2.3	29.5	7.8	22.3	6.0
Mean*		2.9	2.1	25.4	4.9	19.8	4.0
SD*		0.3	0.2	3.9	1.8	3.2	1.3
Kodak CR-400	Kodak HR	4.7	3.5	17.3	8.7	13.8	7.3
Agfa Scan-head†	Agfa CsBr screen†	3.1	2.3	58.0	10.0	NA	NA

Note.—All systems were tested at equivalent exposure (~0.3 mR) with a pixel size in the 0.10–0.12-mm range. All results are averages of the response in the horizontal and vertical directions. NA = not available.

*Of the above values reflecting the CR response with standard-resolution turbid phosphor screens.

†Prototypic system using structured phosphor and line-scanning scan-head technology; preliminary results.

Table 2
MTF and DQE Performance of Some Commercial Flat-Panel Detectors at Equivalent Exposure (~0.3 mR) with RQA5 and RQA9 Techniques

Flat-Panel System	Detector Type	Pixel Size	Frequency (mm^{-1}) at Specified MTF		Percent DQE with RQA5 at Specified Frequency		Percent DQE with RQA9 at Specified Frequency	
			0.1 MTF	0.2 MTF	0.15 mm^{-1}	2.5 mm^{-1}	0.15 mm^{-1}	2.5 mm^{-1}
DRC/Hologic DR-1000	Direct, selenium	0.139	6.2	5.6	38	20	22	11
GE Revolution XQ/i	Indirect, CsI	0.2	3.5	2.6	64	15	45	12
Philips Digital Diagnost*	Indirect, CsI	0.143	3.4	2.6	60	24	NA	NA
Varian Paxscan 2520	Indirect, CsI	0.127	3.9	2.6	64†	20†	54‡	20‡
Varian Paxscan 4030	Indirect, $\text{Gd}_2\text{O}_3\text{S}$	0.127	3.8	2.5	20†	6†	19§	7§

Note.—All results are averages of the response in the horizontal and vertical directions. NA = not available; RQA5 = ~70 kVp, 21-mm Al filtration; RQA9 = ~120 kVp, 40-mm Al filtration.

*Trixell panel; preliminary results.

†70 kVp with 19-mm added Al filtration.

‡115 kVp with 19-mm added Al filtration.

§120 kVp with 19-mm added Al filtration.

cycles/mm at ~70 kVp), mostly because of the lower atomic number of selenium, but shows a somewhat higher response at higher frequencies (20% at 0.15 cycles/mm at ~70 kVp) because of its minimal blur and small pixel size.

Although not listed, lens-coupled CCD- and CMOS-based digital detectors usually exhibit a performance similar to that of CR, even with structured CsI phosphors, because of the reduced collection of the light photons, as discussed previously. The use of fiberoptic

coupling remedies this deficiency somewhat, notably improving the DQE of CCD- and CMOS-based detectors. The CCD-based detectors with slot-scanning geometry (now marketed for chest imaging and for mammography) enjoy the added advantage of not needing an antiscatter grid for scatter rejection, thus notably improving the effective DQE of the system. (Note that the DQE is always measured and reported without the grid; for a system with the grid, the effective DQE is equal to the measured DQE times the mean grid transmission.)

Digital mammographic detectors exhibit a notably different response because of their smaller pixel size and the applied x-ray energy. In particular, selenium, in spite of having a lower atomic number than most phosphors, including CsI, has a high absorption efficiency at mammographic energies. As a result, with equivalent thickness, selenium-based direct flat-panel detectors have higher DQE than CsI-based indirect detectors, opposite to the behavior observed at radiographic energies (>70 kVp) (16,17).

SUMMARY

The main sharpness limitation in DR systems is the spreading of secondary energy carriers in the bulk of the capture and coupling elements of the detectors, which can be improved by the use of thinner capture elements, improved coupling, structured phosphors (in phosphor-based detectors), or electric fields (in direct flat-panel detectors). The main noise limitation in DR systems is the inefficient detection and collection of x-ray photons and secondary energy carriers. Noise may be improved (reduced) by the use of structured phosphors and efficient coupling (in phosphor-based detectors) and by a reduction of electronic noise within the detector. Phosphor-based detectors that use structured phosphors (CR or flat-panel) exhibit superior MTF and DQE compared with turbid phosphor-based detectors (CR or flat-panel). In comparison, selenium-based direct flat-panel detectors exhibit considerably higher MTF (at all frequencies), with lower DQE (mostly at low frequencies) at radiographic energies and with higher DQE at mammographic energies.

Acknowledgment: The author thanks many colleagues for intellectual contributions and helpful discussions regarding materials presented in this chapter.

References

- Rossmann K. Point spread-function, line spread-function, and modulation transfer function: tools for the study of imaging systems. *Radiology* 1969; 93:257–272.
- Rossmann K. Spatial fluctuations of x-ray quanta and the recording of radiographic mottle. *Radiology* 1963; 90:863–869.
- Dobbins JT III. Image quality metrics for digital systems. In: Van Metter RL, Beutel J, Kundel HL, eds. *Handbook of medical imaging: physics and psychophysics*. Vol 1. Bellingham, Wash: SPIE, 2000; 161–222.
- Samei E, Flynn MJ. An experimental comparison of detector performance for computed radiography systems. *Med Phys* 2002; 29:447–459.
- Yaffe MJ, Rowlands JA. X-ray detectors for digital radiography. *Phys Med Biol* 1997; 42:1–39.
- Samei E. Image quality in two phosphor-based flat panel digital radiographic detectors. *Med Phys* 2003; 30:1747–1757.
- Rowlands JA, Ji WG, Zhao W, Lee DL. Direct conversion flat panel x-ray imaging: reduction of noise by presampling filtration. *Proc SPIE* 2000; 3977:446–455.
- Barrett HH, Swindell W. *Radiological imaging: the theory of image formation, detection, and processing*. New York, NY: Academic Press, 1981.
- Flynn M, Wilderman S, Kanicki J. Effect of secondary radiations on the performance of digital radiographic detectors. *Proc SPIE* 1998; 3336:326–336.
- Cunningham IA, Yao J, Subotic V. Cascaded models and the DQE of flat-panel imagers: noise aliasing, secondary quantum noise, and reabsorption. *Proc SPIE* 2002; 4682: 61–72.
- Samei E, Flynn MJ. An experimental comparison of detector performance for direct and indirect digital radiography systems. *Med Phys* 2003; 30:608–622.
- Rabbani M, Shaw R, Van Metter R. Detective quantum efficiency of imaging systems with amplifying and scattering mechanisms. *J Opt Soc Am A* 1987; 4:895–901.
- Cunningham IA. Applied linear-systems theory. In: Van Metter RL, Beutel J, Kundel HL, eds. *Handbook of medical imaging: physics and psychophysics*. Vol 1. Bellingham, Wash: SPIE, 2000; 79–159.
- Hejazi S, Trauernicht DP. System considerations in CCD-based x-ray imaging for digital chest radiography and digital mammography. *Med Phys* 1997; 24:287–297.
- Maidment AD, Yaffe MJ. Analysis of the spatial-frequency-dependent DQE of optically coupled digital mammography detectors. *Med Phys* 1994; 21:721–729.
- Zhao W, Ji WG, Debrrie A, Rowlands JA. Imaging performance of amorphous selenium based flat-panel detectors for digital mammography: characterization of a small area prototype detector. *Med Phys* 2003; 30:254–263.
- Vedantham S, Karella A, Suryanarayanan S, et al. Full breast digital mammography with an amorphous silicon-based flat panel detector: physical characteristics of a clinical prototype. *Med Phys* 2000; 27:558–567.

TABLE II. Testing devices required to perform the acceptance testing of a CR imaging device.

Testing device
Calibrated x-ray source
Calibrated hard/soft-copy display devices
Densitometer (if a hard-copy display is to be used)
Copper and aluminum filters
Calibrated ion chamber
Stand for the ion chamber
Screen cleaning solution and cloths
Two metric 30 cm steel rulers (for laser-beam function and spatial accuracy tests)
Three sector-type (0.4°) line-pair phantoms of up to 5 lp/mm frequency (≥ 0.05 mm lead thickness)
Low-contrast phantom (e.g., Leeds TO.12)
Screen-contact wire-mesh pattern
Screen-contact fine wire-mesh pattern (e.g., mammography screen-film contact tool)
Small lead block (>3 mm thick)
Antiscatter grid (10:1 or 12:1, 103 ln/in.) (if the x-ray system does not have one)
Anthropomorphic phantoms (foot, hand, pelvis, chest, etc.)
Timer
Measuring tape
Flashlight
Role of masking tape

devices. The lack of uniformity in measurement procedures among different manufacturers has introduced ambiguity in the meaning of the system specifications. For example, different manufacturers calibrate the response of the system to a given exposure value using different beam qualities and re-

port the response using indices which have different dependences on exposure. In a large medical institution in which CR devices of different kinds might be employed, it is important to assure that the patient images are acquired within a certain exposure range to prevent over- and underexposures. However, the lack of calibration uniformity makes the definition of the acceptable exposure ranges from the CR response values cumbersome.

In general, in order to achieve a consistent level of clinical performance, acceptance testing should utilize a uniform cross-platform methodology and uniform criteria so that the results of the tests can be correlated with clinical performance standards. Currently, Task Group No. 10 of the American Association of Physicists in Medicine (AAPM TG10)⁵ is making an effort to provide a comprehensive standardized testing protocol for acceptance testing and quality control of CR systems. In this work, we have used the preliminary guidelines established by the AAPM Task Group to evaluate the performance of CR systems currently in use at different institutions represented by the co-authors. The paper provides a summary of the tests recommended by the AAPM Task Group, delineates the specific technical aspects of the tests, suggests quantitative measures of the performance results, and recommends uniform quantitative criteria for satisfactory performance. The recommendations provided in this paper are a first step toward meeting a need perceived by practicing clinical medical physicists for quantitative guidelines to be used in conjunction with AAPM TG10 recommended testing procedures.

TABLE III. Testing protocol and acceptance criteria for the dark noise test.

	Agfa	Fuji	Kodak	Lumisys
Exposure condition	No exposures. Erase a single screen and read it without exposing it.			
Screen processing	System diagnostics/flat field, speed class=200	Test/sensitivity ($L=1$), fixed EDR ($S=10\,000$)	Pattern	Standard
Image postprocessing	None musica parameters=0.0 Sensitometry=linear	“Linear” (GA=1.0, GT=A, RE=0.0)	“Raw data” and “no edge enhancement” settings, window=512, level=exposure index	None
Measurements to be made	IgM, average pixel value (PV) and its standard deviation (PVSD), and scan average level (SAL) within 80% of the image	Avg. pixel value (PV) and its standard deviation (PVSD) within 80% of the image area	Exposure index (EI), average pixel value (PV), and its standard deviation (PVSD) within 80% of the image area	Average pixel value (PV) and standard deviation (PVSD) within 80% of the image area
Qualitative criteria for acceptance	Uniform image without any artifacts			
Quantitative criteria for acceptance	IgM<0.28 SAL<130 PV<350 PVSD<5	PV<280 ^a PVSD<4	EI _{GP} <80, EI _{HR} <380 PV _{GP} <80, PV _{HR} <80 PVSD<4	PV>3425 PVSD<4

^aFor those systems in which there is a direct relationship between PV and $\log(E)$. In the case of an inverse relationship, PV should be greater than 744.

TABLE IV. Testing protocol and acceptance criteria for uniformity (CR screen test).

	Agfa	Fuji	Kodak	Lumisys
Exposure condition	This test is applied to all the screens. Visually inspect the screens for physical defects. Verify that the cassette label matches the type of screen inside. Expose the screen to 10 mR ($2.58 \times 10^{-6} \text{ C/kg}$) ^a entrance exposure using 80 kVp, 0.5 mm Cu and 1 mm Al filtration, and 180 cm source-to-image distance (SID). If significant heel effect is present, test can be performed with two sequential half-exposures between which the orientation of the cassette is reversed.			
Screen processing	System diagnosis/flat field, speed class=200	Test/sensitivity ($L=1$), Semi EDR	Pattern	Standard
Image postprocessing	None, Musica parameters=0.0 Sensitometry=linear	“Linear” ($GA=1.0$, $GT=A$, $RE=0.0$)	“Raw data” and “no edge enhancement” settings, window=512, level=exposure index	None
Measurements to be made	Average pixel value (PV) and its standard deviation (PVSD) within 80% of the image area <i>Screen-to-screen variations:</i> Standard deviation of IgM (LMSDs), and mean and standard deviation of PV among screens (PVs and PVSDs)	Average pixel value (PV) and its standard deviation (PVSD) within 80% of the image area <i>Screen-to-screen variations:</i> Standard deviation/mean sensitivity (SD/Ss) and standard deviation of average PV among screens (PVSDs)	Average pixel value (PV) and its standard deviation (PVSD) within 80% of the image area <i>Screen-to-screen variations:</i> Standard deviation of exposure index among screens (EISDs)	Average pixel value (PV) and its standard deviation (PVSD) within 80% of the image area <i>Screen-to-screen variations:</i> Standard deviation of average PV among screens (PVSDs)
Qualitative criteria for acceptance			Uniform image without any artifacts	
Quantitative criteria for acceptance	PVSD<25 (single screen) LMSDs<0.02 PVSDs<25	PVSD<20 (single screen) SD/Ss<5% PVSDs<20	PVSD<20 (single screen) EISDs<20	PVSD<20 (single screen) PVSDs<20

^aThroughout these tables, for convenience, all exposures are expressed in units of mR ($1 \text{ mR} = 2.58 \times 10^{-7} \text{ C/kg}$).

II. METHODS AND RECOMMENDATIONS

As listed in Table I, CR devices in use at five different institutions from four major CR manufacturers were evaluated. The inventory of equipment used for testing is listed in Table II. Each system was evaluated for dark noise, screen uniformity, exposure indicator calibration, linearity and autoranging response, laser beam function, limiting resolution, noise and low-contrast resolution, spatial accuracy, erasure thoroughness, aliasing and grid response, and throughput.⁶ Special attention was paid to applying a uniform testing protocol for different CR systems, following the recommendations of the AAPM TG10 as closely as practicable. The data from different institutions were collected and processed in a single database. Prior to or shortly after the evaluations, each system's performance was judged clinically acceptable by attending radiologists based on image quality of clinical images acquired with the system. Tables III–XIII tabulate the testing protocol and the acceptance criteria derived from the results. For a full description of the tests and the rationale for performing each test, the reader is advised to consult the AAPM TG10 report.

The quantitative acceptance criteria were established based on the results of the tests performed on the clinical systems and a uniform level of tolerance in system response across different systems. Table XIV tabulates the response tolerance levels based upon which the acceptance criteria were established. These levels were translated to system-

specific parameters, as reported in Tables III–XIII, using the response relationships of the systems tabulated in Table XV. None of the clinically acceptable systems tested in this collaborative effort generated results beyond the established criteria. In most instances, the acceptance criteria were at least 20% beyond the extremes of the evaluation results, a reasonable margin considering that the evaluated systems were not operating at the borderline of clinical acceptability.

Several experimental precautions were observed in the evaluation of the systems. All the phosphor screens were cleaned and erased prior to executing the testing procedures. Consistent delay times between 1 to 15 min were observed between exposing and reading the screens. Care was taken to reduce backscattered radiation by utilizing cross-table exposures and significant interspace behind the screens. A large source-to-image distance (SID~180 cm) was used to minimize the heel effect. The “raw” signal values which were proportional to the log of the incident exposure without any postprocessing were used in the evaluations.

All exposures were measured in a consistent fashion: The collimators were set to expose the whole cassette with additional 7 cm margins on each side in the direction perpendicular to the anode–cathode axis. The ion chamber was then placed at the center of the beam at 2/3 of the SID. The exposure was measured in five consecutive exposures and the values averaged, E_1 . Keeping the ion chamber at 2/3 SID, the chamber was shifted on the central axis perpendicu-

TABLE V. Testing protocol and acceptance criteria for exposure indicator calibration.

	Agfa	Fuji	Kodak	Lumisys ^b
Recommended exposure condition ^a	Use multiple screens (at least three) of a given size/type. Expose the screens to approximately 1 mR (2.58×10^{-7} C/kg) enhance exposure using 80 kVp and 0.5 mm Cu/1 mm Al filtration. Screens should be read with a precise 10 min delay.			
Exposure condition (manufacturer specified ^a)	Expose a screen to approximately 1 mR (2.58×10^{-7} C/kg) entrance exposure using 75 kVp and 1.5 mm Cu filtration. Screen should be read promptly.	Expose a screen to approximately 1 mR (2.58×10^{-7} C/kg) entrance exposure using 80 kVp without filtration. Screen should be read with a precise 10 min delay.	Expose a screen to approximately 1 mR (2.58×10^{-7} C/kg) entrance exposure using 80 kVp and 0.5 mm Cu/1 mm Al filtration. Screen should be read with a precise 15 min delay.	Expose a screen to approximately 8 mR (2.064×10^{-6} C/kg) entrance exposure using 80 kVp with 1 mm Cu filtration. Screen should be read promptly.
Screen processing	System diagnosis/flat field, speed class=200	Test/sensitivity ($L=1$), semi-EDR	Pattern	Standard
Image postprocessing	None, musica parameters=0.0		Irrelevant	None
Measurements to be made	IgM and IgM normalized to exactly 1 mR exposure to the screen ($IgM_{1\text{mR}}$) using $IgM_{1\text{mR}} = IgM - \log(\text{exposure})$, SAL and SAL normalized to exactly 1 mR exposure to the screen ($SAL_{1\text{mR}}$) using $SAL_{1\text{mR}} = SAL / (\text{exposure})^{0.5}$	Sensitivity and sensitivity normalized to exactly 1 mR exposure to the screen ($S_{1\text{mR}}$) using $S_{1\text{mR}} = S / \text{exposure}$	Exposure index (EI) and exposure index normalized to exactly 1 mR exposure to the screen ($EI_{1\text{mR}}$) using $EI_{1\text{mR}} = EI - 1000 \times \log(\text{exposure})$	Mean pixel value (PV) within 80% of the image area normalized to exactly 1 mR ($PV_{1\text{mR}}$) or 8 mR ($PV_{8\text{mR}}$) exposure to the screen using $PV_{1\text{mR}} = PV + 1000 \log(\text{exposure})$ $PV_{8\text{mR}} = PV + 1000 \log(\text{exposure}/8)$
Qualitative criteria for acceptance			None	
Quantitative criteria for acceptance	$IgM_{1\text{mR}} - 2.2 < \pm 0.045$ single screen $IgM_{1\text{mR}} - 2.2 < \pm 0.023$ for all screens averaged $SAL_{1\text{mR}} - 1192 < \pm 60$ single screen $SAL_{1\text{mR}} - 1192 < \pm 30$ for all screens averaged	$S_{1\text{mR}} - 200 < \pm 20$ single screen $S_{1\text{mR}} - 200 < \pm 10$ for all screens averaged	$EI_{1\text{mR}} - 2000 < \pm 45$ single screen $EI_{1\text{mR}} - 2000 < \pm 23$ for all screens averaged	$PV_{8\text{mR}} - 600 < \pm 45$ single screen $PV_{1\text{mR}} - 1505 < \pm 45$ single screen $PV_{1\text{mR}} - 1505 < \pm 23$ for all screens averaged

^aThere is currently a strong consensus that CR systems should be calibrated with a standard filtered beam. Until such time as manufacturers change their recommendations, the calibration procedure can be performed both with the manufacturer-defined technique, to verify conformance with the manufacturer's specifications, and with 0.5 mm Cu/1 mm Al filtration and 10 min delay time, for benchmarking and constancy checks.

^bThe Lumisys ACR-2000 software did not make use of an exposure index at the time of testing. The system is calibrated to produce a pixel value of 600 in response to an 8 mR (2.064×10^{-6} C/kg) exposure to the screen.

lar to the anode–cathode axis toward the edge of the field just outside the useful beam area (the shadow of the ion chamber was still fully within the beam without projecting over the cassette area). The exposure was measured in five consecutive exposures again and the values were averaged, E_2 . The chamber was kept at the second location during the tests for verification of the exposure values. The average exposure to the cassette in each single exposure was calculated as $(E_1/E_2)(2/3)^2$ (measured exposure).

III. DISCUSSION

To achieve a consistent level of clinical performance from CR systems, acceptance testing procedures should be performed according to a uniform cross-platform methodology. As in any medical physics survey, the performance evaluation of a CR system is also more definitive and objective

when the evaluation is quantitative and the results are compared against specific quantitative acceptance criteria. In this work, an attempt was made to outline a cross-platform uniform methodology based on the guidelines being developed by the American Association of Physicists in Medicine Task Group 10. Furthermore, a first attempt was made to recommend quantitative acceptance criteria for satisfactory performance of a CR system based on the current state of practice. The criteria were established using uniform tolerance levels and test results acquired from CR systems in clinical use at five different institutions. The *user* specificity (as opposed to the conventional *manufacturer* specificity) of the acceptance criteria suggested in this paper was necessitated by the desired uniformity of the testing procedures. The criteria, however, do not guarantee optimal clinical performance, which may not be ascertained without comprehensive clinical trials.

TABLE VI. Testing protocol and acceptance criteria for linearity and autoranging response.^a

	Agfa	Fuji	Kodak	Lumisys
Exposure condition	Use a single screen (multiple screens may also be used if the screen-to-screen variations in the previous test were found minimal). Expose the screen to approximately 0.1, 1, and 10 mR (2.58×10^{-8} , 2.58×10^{-7} , 2.58×10^{-6} C/kg) entrance exposures in a sequence of three exposure-reading cycles using 80 kVp, 0.5 mm Cu and 1 mm Al filtration, and 180 cm SID. Each time read the screen with a consistent delay time.			
Screen processing	System diagnosis/flat field, speed class=200	Test/ave 4.0 Semi-EDR and fixed EDR=200 repeat also with Test/contrast semi-EDR and fixed EDR=200	Pattern	Standard
Image postprocessing	None, musica parameters=0.0	“Linear” (GA=1.0, GT=A, RE=0.0)	“Raw data” and “no edge enhancement” settings	None
Measurements to be made	IgM, average pixel value (PV), and scan average level (SAL) within 80% of the image area. Slopes and correlation coefficients (CCs) of linear fits to log(SAL) vs log(E), PV vs log(E), and IgM vs log(E)	<i>For Semi EDR</i> , correlation coefficient (CC) of a linear fit to log(S) vs log (E) plot. <i>For fixed EDR</i> , avg. pixel value (PV) within 80% of the image area, slope and correlation coefficient (CC) of a linear fit to PV vs log(E)	Exposure index (EI) and avg. pixel value (PV) within 80% of the image area. Slope and correlation coefficient (CC) of a linear fit to EI vs log(E) and PV vs log (E) plots	Mean pixel value (PV) within 80% of the image area. Slope, intercept, and correlation coefficient (CC) of a linear fit to P vs log(E)
Qualitative criteria for acceptance	SAL vs exposure on a linear-log plot should result in a straight line	<i>For semi-EDR</i> , slope and correlation, sensitivity vs exposure on a log-log plot should result in a straight line. <i>For fixed EDR</i> , to PV vs exposure on a linear-log plot should result in a straight line	The plot of EI and PV vs exposure on a linear-log scale should result in straight lines	The plot of PV vs exposure on a linear-log scale should result in a straight line
Quantitative criteria for acceptance	Slope _{IgM} -1 < ± 0.1 Slope _{SAL} /0.5 - 0.1 < ± 0.1 Slope _{PV} /1250 - 0.1 < ± 0.1 CCs > 0.95	Slope _s +1 < ± 0.1 Slope _{PV} /256 - 1 < ± 0.1 (Ave 4) ^b Slope _{PV} /511 - 1 < ± 0.1 (Con.) ^b CCs > 0.95	Slope _{EI} /1000 - 1 < ± 0.1 Slope _{PV} /1000 - 0.1 < ± 0.1 CCs > 0.95	Slopes/1000 + 1 < ± 0.1 CCs > 0.95

^aIf this test is performed with hard copy prints, the relationship between the pixel value (PV) and optical density (OD) should be established beforehand using an electronic test pattern. The relationship between OD and PV should then be incorporated as a transformation in the quantitative analysis of the results.

^bNote that in some Fuji systems, there is an inverse relationship between PV and log(E). For those systems, the polarity of the slope in these equations should be reversed.

TABLE VII. Testing protocol and acceptance criteria for the laser beam function.

	Agfa	Fuji	Kodak	Lumisys
Exposure condition	Place a steel ruler roughly perpendicular to the laser-scan direction on a screen. Expose the screen to about 5 mR (1.29×10^{-6} C/kg) entrance exposure using a 60 kVp beam without any filtration (SID=180 cm). Examine the edges of the ruler on the image for laser beam jitters using 10–20× magnification.			
Screen processing	System diagnosis/flat field, speed class=200	Test/sensitivity Semi-EDR	Pattern	Standard
Image postprocessing	None, musica parameters=0.0, sensitometry=linear	“Linear” (GA=1.0, GT=A, RE=0.0)	“Raw data” and “no edge enhancement” settings, window=512, level=exposure index	None
Measurements to be made		If any jitter is present, jitter dimension using workstation’s “measurement” or ROI tool.		
Qualitative criteria for acceptance		Ruler edges should be straight and continuous without any under- or overshoot of the scan lines in light to dark transitions.		
Quantitative criteria for acceptance		There should not be more than occasional ±1 jitters.		

TABLE VIII. Testing protocol and acceptance criteria for the limiting resolution and resolution uniformity.^a

	Agfa	Fuji	Kodak	Lumisys
Exposure condition	This test should be done for each type and size of the screens. Use a 60 kVp, unfiltered x-ray beam (SID=180 cm). Place three line-pair pattern devices on the cassette, two in orthogonal directions and one at 45°. Expose the screen with an exposure of about 5 mR (1.20×10^{-6} C/kg). Also acquire an image of a fine wire mesh (e.g., mammography screen-film contact test tool) in contact with the cassette to examine the consistency of the resolution response across the image.			
Screen processing	System diagnosis/flat field, speed class=200	Test/sensitivity semi-EDR	Pattern	Standard
Image postprocessing	None, musica parameters=0.0 sensitometry=linear	“Linear” (GA=1.0, GT=A, RE=0.0)	“Raw data” and “no edge enhancement” settings, window=512, level=exposure index	None
Measurements to be made	Maximum discernible spatial frequencies in the three directions (R_{hor} , R_{ver} , R_{45}) using a magnified ($>10\times$), narrowly windowed presentation of the images			
Qualitative criteria for acceptance	The image of the wire mesh should be uniform without any blurring across the image			
Quantitative criteria for acceptance		$R_{\text{hor}}/f_{\text{Nyquist}} > 0.9$ $R_{\text{ver}}/f_{\text{Nyquist}} > 0.9$ $R_{45}/1.41 f_{\text{Nyquist}} > 0.9$		

^aNote that the spatial resolution response of a CR system can be more comprehensively evaluated by measuring the modulation transfer function (MTF) of the system (Refs. 7–9, 11–14).

TABLE IX. Testing protocol and acceptance criteria for noise and low-contrast resolution.^a

	Agfa	Fuji	Kodak	Lumisys
Exposure condition	This test should be done for each type and size of the screens. A low-contrast resolution pattern is used (e.g., Leeds TO.12, 75 kVp beam with 1 mm of Cu filtration). For each screen type/size, acquire three images of the low-contrast phantom using 0.1, 1, and 10 mR (2.58×10^{-8} , 2.58×10^{-7} , 2.58×10^{-6} C/kg) exposures to the screens. Use a constant delay time of 10 min in reading each of the screens.			
Screen processing	System diagnosis/flat field, speed class=200	Test/contrast Semi-EDR	Pattern	Standard
Image postprocessing	None, musica parameters=0.0 Sensitometry=linear	“Linear” (GA=1.0, GT=A, RE=0.0)	“Raw data” and “no edge enhancement” settings, window=512, level=4096–EI (for GP screens) or level=3796–EI (for HR screens)	None
Measurements to be made	Minimum discernible contrast for each object size (contrast detail threshold), Standard deviation of pixel value (PVSD) within a fixed (size and location) small region of the images, correlation coefficient (CC) of the linear fit to log(PVSD) vs log(E). ^b			
Qualitative criteria for acceptance	Contrast-detail threshold should be proportionately lower at higher exposures.	Contrast-detail threshold should be proportionately lower at higher exposures, with higher contrast thresholds for standard-resolution screens.	Contrast-detail threshold should be proportionately lower at higher exposures.	
Quantitative criteria for acceptance		CC>0.95 ^b		

^aNote that the noise response of a CR system can be more comprehensively evaluated by measuring the noise power spectrum (NPS) and the detective quantum efficiency (DQE) of the system at different exposure levels (Refs. 8 and 9, 11–14).

^bThe quantitative evaluation is more valid with uniform images acquired for the linearity test (Table VI) because of the absence of scattering material in the beam. The expected quantitative response is based on the assumption of a logarithmic relationship between pixel value and exposure (Table XV).

TABLE X. Testing protocol and acceptance criteria for spatial accuracy.

	Agfa	Fuji	Kodak	Lumisys
Exposure condition	Place a regular wire-mesh screen-film contact test tool over cassette. Expose the cassette to about 5 mR (1.29×10^{-6} C/kg) entrance exposure using a 60 kVp beam without any filtration (SID=180 cm). Repeat the acquisition with two steel rulers in the vertical and the horizontal directions.			
Screen processing	System diagnosis/flat field, speed class=200	Test/contrast Semi-EDR	Pattern	Standard
Image postprocessing	None musica parameters=0.0	“Linear” (GA=1.0, GT=A, RE=0.0)	“Raw data” and “no edge enhancement” settings, window=512, level=EI	None
Measurements to be made	Distances in the orthogonal directions (15 cm minimum length) measured using the measurement tool of the workstation. ^a			
Qualitative criteria for acceptance		Grid pattern spacing should be uniform without any distortion across the image.		
Quantitative criteria acceptance		Measured distance should be within 2% of the actual values.		

^aAlternatively, length measurements can be made on a hard-copy film printed in “true-size.”

TABLE XI. Testing protocol and acceptance criteria for erasure thoroughness.

	Agfa	Fuji	Kodak	Lumisys
Exposure condition	Place a thick lead block at the center of a 14×17 cassette and expose the screen to about 50 mR (1.29×10^{-5} C/kg) using a 60 kVp x-ray beam without any filtration (SID=180 cm). Read the screen, and expose it a second time to 1 mR (2.58×10^{-7} C/kg) entrance exposure without the lead object using the same beam quality collimated in by about 5 cm on each side of the screen. For a quantitative test <i>re-read</i> the screen after the second exposure <i>without exposing it</i> .			
Screen processing	System diagnosis/flat field, speed class=200	Test/sensitivity semi-EDR	Pattern	Standard
Image postprocessing	None, musica parameters=0.0 Sensitometry=linear Window setting default or equivalent to 1 log(exposure) unit	“Linear” (GA=1.0, GT=A, RE=0.0) Window setting default or equivalent to 1 log(exposure) unit	“Raw data” and “No edge enhancement” settings, level=EI, window setting default or equivalent to 1 log(exposure) unit	Window setting default or equivalent to 1 log(exposure) unit
Measurements to be made	IgM, average pixel value (PV) and its standard deviation (PVSD), and scan average level (SAL) within 80% of the reread/unexposed image	Avg. pixel value (PV) and its standard deviation (PVSD) within 80% of the reread/unexposed image	Exposure index (EI), average pixel Value (PV), and its standard deviation (PVSD) within 80% of the reread/unexposed image	Average pixel value (PV) and standard deviation (PVSD) within 80% of the reread/unexposed image
Qualitative criteria for acceptance		Absence of a ghost image of the lead block from the first exposure in the reexposed image. ^{a,b}		
Quantitative criteria for acceptance	IgM=0.28 SAL<130 PV<630 PVSD<5	PV<280 ^c PVSD<4	EI _{GP} <80, EI _{HR} <380 PV _{GP} <80, PV _{HR} <80 PVSD<4	PV>3425 PVSD<4

^aIn our tests on the ACR-2000 system, the length of the standard erasure cycle was sufficient for exposures up to 32 mR (8.256×10^{-6} C/kg). Higher exposures to the screen required an additional erasure cycle for complete screen erasure.

^bNote that erasure time in some systems (e.g., Agfa) is configurable on an exam-by-exam basis.

^cFor those systems in which there is an direct relationship between PV and log(E). In the case of inverse relationship, PV should be greater than 744.

TABLE XII. Testing protocol and acceptance criteria for the aliasing/grid response.

	Agfa	Fuji	Kodak	Lumisys
Exposure condition	This test should be performed for each type and size of screens that will be commonly used. Place the screen in a bucky that contains an antiscatter grid so that the grid lines are parallel to the laser-scan direction. Alternatively, a grid may be placed directly on the screen. Make sure the grid movement is disabled. Expose the screen to 1 mR (2.58×10^{-7} C/kg) using an 80 kVp beam filtered with 0.5 mm Cu/1 mm Al filter and a SID according to the specification of the grid. Repeat, placing the screen perpendicular to the laser-scan direction. Repeat the exposures with a moving grid.			
Screen processing	System diagnosis/flat field, Speed class=200	Test/contrast semi-EDR	Pattern	Standard
Image postprocessing	None, musica parameters=0.0 sensitometry=linear A narrow window setting	“Linear” (GA=1.0, GT=A, RE=0.0) A narrow window setting	“Raw data” and “no edge enhancement” settings, level=EI, a narrow window setting	None
Measurements to be made		None		
Qualitative criteria for acceptance	Moiré pattern should not be present when the grid lines are perpendicular to the laser-scan direction. For moving grids, no moiré pattern should be apparent when the screen is placed in either direction. ^a			
Quantitative criteria for acceptance		None		

^aMoiré patterns caused by display sampling (not addressed in this protocol) can be distinguished by their changing behavior with changing the magnification of the image on the soft-copy display device.

In light of this limitation, the recommended quantitative criteria should only be considered as helpful suggestions that require further clinical validation in the future.

Another limitation of the current work is the fact that many of the evaluation procedures were not fully quantitative or can be influenced by the subjectivity of the examiner. The evaluations of limiting resolution and noise performance (Tables VIII and IX) are two important examples. The resolution tests used do not evaluate the system transfer characteristics but only establish that some modulation can be detected at the limiting frequency. The noise tests subjectively evaluate the contrast-detail characteristics of the system, and

the proposed quantitative test does not evaluate the spatial characteristics of image noise. Ideally, the resolution and noise characteristics of a CR system should be more objectively evaluated by measuring the frequency-dependent modulation transfer function, the noise power spectrum, and the detective quantum efficiency of these systems. A number of investigators have been able to successfully and reproducibly characterize the resolution and noise performance of CR systems using these indices,^{11–13} and more recently reproducible measurements have been made in the field.^{7,14} However, a routine implementation of these measurements awaits further standardization of measurement methods, and the de-

TABLE XIII. Testing protocol and acceptance criteria for the throughput.

	Agfa	Fuji	Kodak	Lumisys
Exposure condition	Expose 4 screens to 80 kVp, 2 mR (5.18×10^{-7} C/kg). Process the screens sequentially without delay. ^a			
Screen processing	System diagnosis/flat field, speed class=200	Test/contrast semi-EDR	Pattern	Standard
Image postprocessing	musica parameters typical of those in clinical usage		Irrelevant	None
Measurements to be made	Time interval (t , in minutes) between putting the first screen in and the last image appearing on the CR viewing station ^b Throughput (screens/h)= $60 \times 4/t$			
Qualitative criteria for acceptance		None		
Quantitative criteria for acceptance		Throughput should be within 10% of the system’s specifications.		

^aThe test can be performed multiple times with different size cassettes.

^bContribution of the network configuration is not considered.

TABLE XIV. The CR response tolerance levels based upon which the uniform quantitative acceptance criteria were derived (using the equations tabulated in Table XV). All signal levels and standard deviations are expressed in terms of corresponding exposure (E) values deduced from those quantities.

Characteristics	Quantity of interest	Acceptable tolerance
Dark noise	Average signal and its standard deviation within 80% of the image area	$E < 0.012 \text{ mR}$ ($E < 3.1 \times 10^{-9} \text{ C/kg}$) $\sigma_E/E < 1\%$
Uniformity	Signal standard deviation within 80% of the image area, and the standard deviation of the average screen signal among screens	$\sigma_E < 5\%$
Exposure calibration	The exposure indicator response (expressed in terms of exposure) to 1 mR ($2.58 \times 10^{-7} \text{ C/kg}$) entrance exposure	$E_{\text{measured}} - 1 < \pm 10\%$
Linearity and autoranging	The slope of the system response (expressed in terms of logarithm of exposure) vs logarithm of actual exposure	Slope $-1 < \pm 10\%$ Correlation coefficient > 0.95
Laser beam function	Jitter dimension in pixels	Occasional jitters $< \pm 1 \text{ pixel}$
Limiting resolution	Maximum discernible spatial frequencies of a high-contrast line-pair pattern in two orthogonal and 45° angle directions	$R_{\text{hor}}/f_{\text{Nyquist}} > 0.9$ $R_{\text{ver}}/f_{\text{Nyquist}} > 0.9$ $R_{45}/1.41f_{\text{Nyquist}} > 0.9$
Noise and low-contrast resolution	A linear fit of system noise (expressed in terms of logarithm of corresponding σ_E/E) to logarithm of actual exposure	Correlation coefficient > 0.95
Spatial accuracy	The difference between the measured (d_m) and actual distances (d_0) in the orthogonal directions	$(d_m - d_0)/d_0 < 2\%$
Erasure thoroughness	Average signal and its standard deviation within 80% of the reread/unexposed image	$E < 0.012 \text{ mR}$ ($E < 3.1 \times 10^{-9} \text{ C/kg}$) $\sigma_E/E < 1\%$
Aliasing/grid response	No quantitative tolerance levels	
Throughput	Measured throughput in screens per hours (T_m) and the specified throughput (T_0)	$(T_0 - T_m)/T_0 < 10\%$

velopment of automated commercial QC products.

In this study, the exposures for quantitative measurements were made with 0.5 mm copper and 1 mm additive aluminum filtration in the beam. The use of filtration was based on prior studies^{10,15,16} indicating that the use of 0.5 mm Cu filter minimizes the dependency of the results on the kVp inaccuracy and on the variations in the x-ray generator type, as the filter attenuates the "soft" portion of the spectrum, predominantly responsible for tube-to-tube variations (Fig. 1). The use of this filtration also makes the spectrum a more accurate representative of primary x rays incident on the detector in clinical situations (Fig. 2). The additional post-Cu, 1-mm-thick Al filter is used to attenuate any potential secondary low-energy x rays generated in the Cu filter. The use of 0.5 mm Cu/1 mm Al filtration, therefore, is advised for checking the consistency of the response in the acceptance testing and annual compliance inspections of CR systems.

This paper outlines the steps for only the *physical* evaluation of CR systems. In a newly installed system, after completion of the physical acceptance testing and prior to a full clinical utilization, the system should also be evaluated for its *clinical* performance. The appearance of CR images

may vary as a function of radiographic technique factors, the specific recipe of image processing parameters applied to the images, and the type and calibration of the display media. The default image processing parameters of the system for various anatomical sites and views (e.g., chest PA, chest lateral, chest portable, knee, etc.) should be tested and customized by the application specialists of the manufacturer with assistance of the diagnostic medical physicist and under the direction of the radiologist who is ultimately responsible for the clinical acceptability of the images. Using radiographic techniques provided by the manufacturer, images of various anthropomorphic phantoms should be acquired with various combinations of collimation and positioning, utilizing the appropriate prescribed anatomical menus of the system. In each case, the proper processing of the image and the absence of unexpected positioning and collimation errors should be verified. Attending radiologists should be consulted for acceptability of the image processing parameters for each anatomical menu. Since standard anthropomorphic phantoms have a limited ability to represent human anatomy and patient-to-patient variations, the clinical evaluation and cus-

TABLE XV. The relationship between exposure and pixel value/exposure indicator responses of various CR systems. The relationships which were provided by the manufacturers or derived from their literature, were verified against experimental measurements at 80 kVp with 0.5 mm Cu/1 mm Al filtration. In these relationships, PV is the pixel value, E is the exposure in mR, B is the speed class, and L is the latitude of the system.

	Agfa	Fuji	Kodak	Lumisys
Exposure indicator quantities	IgM and scan average level (SAL)	Sensitivity (S)	Exposure index (EI)	None
Exposure indicator relationship	$\text{SAL} = 90\sqrt{0.877cBE}$ $\text{IgM} = 2\log(\text{SAL}) - 3.9478$ $= \log(cBE) - 0.0963$ $c = 1.0 \text{ for MD10 screens}$	$S = 200/E$	$\text{EI} = 1000 \log(E) + 2000$	None
Pixel value relationships	$\text{PV} = 2499 \log(\text{SAL}) - 4933$ $= 1250 \log(cBE) - 121^a$ $c = 1.0 \text{ for MD10 screens}$	$\text{PV} = (1024/L) \times (\log E + \log(S/200)) + 511^b$	$\text{PV} = 1000 \log(E) + c_0$ $c_0 = 2000 \text{ for GP screens}$ $c_0 = 1700 \text{ for HR screens}$	$\text{PV} = 1000 \log(32/E)$
Exposure/reading condition	75 kVp and 1.5 mm Cu filtration, no reading delay	80 kVp without filtration, 10 min reading delay	80 kVp and 0.5 mm Cu/1 mm Al filtration, 15 min reading delay	80 kVp with 1 mm Cu filtration, no reading delay

^aUsing a 12 bit, linear $\log(E)$ data transfer from Agfa QC workstation.

^bAssuming a direct relationship between exposure and pixel value.

tomization of the image processing parameters should include actual clinical images.

Care should be taken that in the validation of the system settings, all examinations performed at the facility are represented. The final customized image processing parameters and system settings for different anatomical menus should be loaded into all units from the same manufacturer in place at the institution or associated medical facilities, where the same exam may be performed on different machines, to assure consistency of image presentations. They should also be documented in a list for future reference.

Patient dose is one of the important implementation considerations in the use of CR in a traditional film-based radiology department.¹⁷ In screen-film radiography, film density is a direct indicator of patient dose. In CR, however, because of the dissociation of the detection and the display functions of the imaging system, optical density can no longer be used as an indicator of the patient dose. In reading a CR screen, almost all CR systems provide an index that reflects the average exposure received by the screen during the image acquisition (Table XV). This exposure indicator can be used to define and monitor patient exposures. Based on the manufacturer's recommendations regarding the intrinsic speed of the system and on the applicable standards of practice, the user should establish, monitor, and enforce the acceptable range of exposure indicator values for the clinical operation in the facility. Note, however, that if a filtration other than that suggested by the manufacturer is used for the exposure calibration of the CR system, as suggested previously, the accepted range of exposure indicator values should be derived based on the comparative results of the two filtration conditions.

Automatic exposure control (AEC) is the primary means for controlling patient exposure in general radiography practice. For screen-film systems, the AEC is calibrated for consistency in optical density resultant from varying exposure techniques. Because of the dissimilarity between x-ray ab-

sorption characteristics and radiographic speed of CR and conventional screen-film radiography systems, an AEC calibrated for screen-film radiography is unlikely to be suitable for CR usage.¹⁸ For CR usage, the AEC can be calibrated using an approach similar to that for screen-film imaging using the exposure indicator value of the system as the target variable to be controlled. The AEC should be adjusted to result an exposure indicator value within a narrow acceptable range (10%–15%) when the kVp or phantom thickness is varied within clinical operational limits. It may also be set to provide a constant change in the exposure indicator value

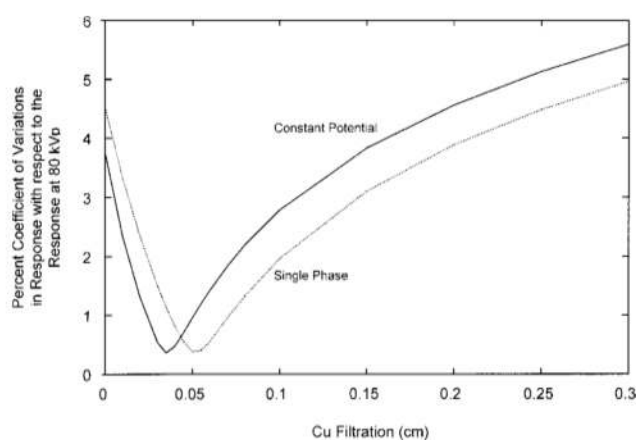


FIG. 1. The relative variation in the response of a CR system (signal per unit exposure), where the energy of the beam is varied within $80 \text{ kVp} \pm 10\%$ range, as a function of Cu filtration in the beam for both single phase and high-frequency/constant-potential generator x-ray systems (12° anode angle, 2.6 mm intrinsic Al filtration). The data were generated by a computational model for simulation of the x-ray spectra, filter attenuation, and absorption characteristics of $\text{BaFBr}_{0.85}\text{I}_{0.15}:\text{Eu}$ phosphor screens (98 mg/cm² phosphor coating weight). The model accuracy has been previously verified against experimental measurements (Refs. 8, 10, 14). Note that Agfa CR systems use a slightly different phosphor material ($\text{Ba}_{0.86}\text{Sr}_{0.14}\text{F}_{1.1}\text{Br}_{0.84}\text{I}_{0.06}$) than the one modeled here.

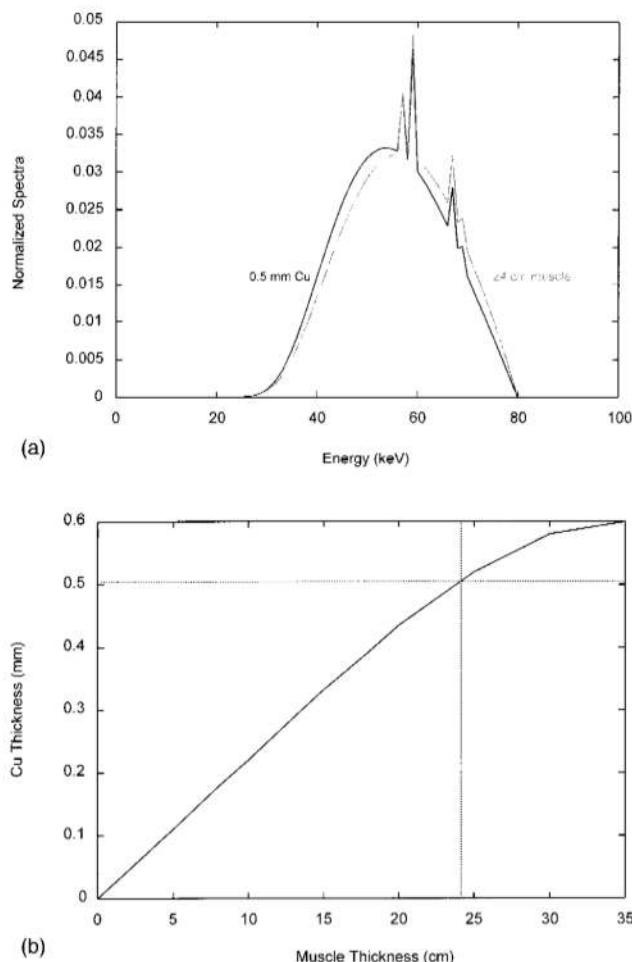


FIG. 2. (a) The model-calculated primary x-ray spectra emerging from a 0.5 mm Cu filter and 24 cm tissue-equivalent material. The spectra were normalized to have the same total area. b) The model-calculated equivalency of the CR signal per unit exposure for various Cu and tissue-equivalent material (see Fig. 1 caption).

when plus or minus density steps are applied. Because the CR exposure indicator is a quantity derived from analysis of the image histogram, care must be exercised in the selection of phantoms and processing menus. The phantoms should produce image histograms representative of clinical images, not a very trivial requirement. Otherwise, inaccurate exposure indicator values may result, leading to faulty AEC calibration. Further work on AEC calibration methodology for CR is warranted.

IV. CONCLUSIONS

The methods and acceptance criteria for the performance evaluation of CR systems were presented in a comprehensive tabular form for imaging systems from four major CR manu-

facturers. The materials can be used as a handbook for acceptance testing and quality control inspection of CR systems to assure the consistency and reliability of their clinical operation.

^{a)}Electronic mail: samei@duke.edu

- ¹R. Schatzing, B. R. Whiting, A. R. Lubinsky, and J. F. Owen, "Digital radiography using storage phosphors," in *Digital Imaging in Diagnostic Radiology*, edited by J. D. Newall and C. A. Kelsey (Churchill Living Stone, 1990), pp. 107–138.
- ²M. Sonoda, M. Takano, J. Miyahara, and H. Kato, "Computed radiography utilizing scanning laser stimulated luminescence," *Radiology* **148**, 833–838 (1983).
- ³J. A. Seibert, "Photostimulable phosphor system acceptance testing," in *Specification, Acceptance Testing and Quality Control of Diagnostic X-ray Imaging Equipment*, edited by J. A. Seibert, G. T. Barnes, and R. G. Gould (AIP, New York, 1994), pp. 771–800.
- ⁴C. E. Willis, R. G. Leckie, J. Carter, M. P. Williamson, S. D. Scotti, and G. Norton, "Objective measures of quality assurance in a computed radiography-based radiology department," *SPIE Med. Imaging* **2432**, 588–599 (1995).
- ⁵J. A. Seibert *et al.*, "Acceptance testing and quality control of photostimulable phosphor imaging systems," Report of the American Association of Physicists in Medicine (AAPM) Task Group No. 10 (unpublished, in the final review process).
- ⁶A. R. Cowen, A. Workman, and J. S. Price, "Physical aspects of photostimulable phosphor computed radiography," *Br. J. Radiol.* **66**, 332–345 (1993).
- ⁷E. Samei, M. J. Flynn, and D. A. Reimann, "A method for measuring the presampled MTF of digital radiographic systems using an edge test device," *Med. Phys.* **25**, 102–113 (1998).
- ⁸E. Samei and M. J. Flynn, "Physical measures of image quality in photostimulable phosphor radiographic systems," *SPIE Med. Imaging* **3032**, 338 (1997).
- ⁹J. T. Dobbins III, D. L. Ergun, L. Rutz, D. A. Hinshaw, H. Blume, and D. C. Clark, "DQE(f) of four generations of computed radiography acquisition devices," *Med. Phys.* **22**, 1581–1593 (1995).
- ¹⁰E. Samei, D. J. Peck, P. L. Rauch, E. Mah, and M. J. Flynn, "Exposure calibration of computed radiography imaging systems (abstract)," *Med. Phys.* **25**, A155 (1995).
- ¹¹C. D. Bradford, W. W. Peppler, and J. T. Dobbins III, "Performance characteristics of a Kodak computed radiography system," *Med. Phys.* **26**, 27–37 (1999).
- ¹²W. Hillen, U. Schiebel, and T. Zaengel, "Imaging performance of a digital storage phosphor system," *Med. Phys.* **14**, 744–751 (1987).
- ¹³C. E. Floyd, H. G. Chotas, J. T. Dobbins III, and C. E. Ravin, "Quantitative radiographic imaging using a photostimulable phosphor system," *Med. Phys.* **17**, 454–459 (1990).
- ¹⁴M. J. Flynn and E. Samei, "Experimental comparison of noise and resolution for 2k and 4k storage phosphor radiography systems," *Med. Phys.* **26**, 1612–1623 (1999).
- ¹⁵C. E. Willis, J. C. Weiser, R. G. Leckie, J. Romlein, and G. Norton, "Optimization and quality control of computed radiography," *SPIE Med. Imaging* **2164**, 178–185 (1994).
- ¹⁶D. M. Tucker and P. S. Rezentes, "The relationship between pixel value and beam quality in photostimulable phosphor imaging," *Med. Phys.* **24**, 887–893 (1997).
- ¹⁷M. Freedman, E. Pe, S. K. Mun, S. C. B. La, and M. Nelson, "The potential for unnecessary patient exposure from the use of storage phosphor imaging systems," *SPIE Med. Imaging* **1897**, 472–479 (1993).
- ¹⁸C. E. Willis, "Computed Radiography: QA/QC," in *Practical Digital Imaging and PACS*, Medical Physics Monograph No. 28 (Medical Physics Publishing, Madison, 1999), pp. 157–175.

Intercomparison of methods for image quality characterization. I. Modulation transfer function^{a)}

Ehsan Samei

Duke Advanced Imaging Laboratories, Departments of Radiology, Biomedical Engineering, and Physics,
Duke University, Durham, North Carolina 27710

Nicole T. Ranger

Duke Advanced Imaging Laboratories, Department of Radiology, Duke University, Durham,
North Carolina 27710

James T. Dobbins III and Ying Chen

Duke Advanced Imaging Laboratories, Departments of Radiology and Biomedical Engineering,
Duke University, Durham, North Carolina 27710

(Received 8 April 2005; accepted for publication 17 February 2006; published 28 April 2006)

The modulation transfer function (MTF) and the noise power spectrum (NPS) are widely recognized as the most relevant metrics of resolution and noise performance in radiographic imaging. These quantities have commonly been measured using various techniques, the specifics of which can have a bearing on the accuracy of the results. As a part of a study aimed at comparing the relative performance of different techniques, in this paper we report on a comparison of two established MTF measurement techniques: one using a slit test device [Dobbins *et al.*, Med. Phys. **22**, 1581-1593 (1995)] and another using a translucent edge test device [Samei *et al.*, Med. Phys. **25**, 102-113 (1998)], with one another and with a third technique using an opaque edge test device recommended by a new international standard (IEC 62220-1, 2003). The study further aimed to substantiate the influence of various acquisition and processing parameters on the estimated MTF. The slit test device was made of 2 mm thick Pb slabs with a 12.5 μm opening. The translucent edge test device was made of a laminated and polished Pt_{0.9}Ir_{0.1} alloy foil of 0.1 mm thickness. The opaque edge test device was made of a 2 mm thick W slab. All test devices were imaged on a representative indirect flat-panel digital radiographic system using three published beam qualities: 70 kV with 0.5 mm Cu filtration, 70 kV with 19 mm Al filtration, and 74 kV with 21 mm Al filtration (IEC-RQA5). The latter technique was also evaluated in conjunction with two external beam-limiting apertures (per IEC 62220-1), and with the tube collimator limiting the beam to the same area achieved with the apertures. The presampled MTFs were deduced from the acquired images by Fourier analysis techniques, and the results analyzed for relative values and the influence of impacting parameters. The findings indicated that the measurement technique has a notable impact on the resulting MTF estimate, with estimates from the overall IEC method 4.0% \pm 0.2% lower than that of Dobbins *et al.* and 0.7% \pm 0.4% higher than that of Samei *et al.* averaged over the zero to cutoff frequency range. Over the same frequency range, keeping beam quality and limitation constant, the average MTF estimate obtained with the edge techniques differed by up to 5.2% \pm 0.2% from that of the slit, with the opaque edge providing lower MTF estimates at lower frequencies than those obtained with the translucent edge or slit. The beam quality impacted the average estimated MTF by as much as 3.7% \pm 0.9% while the use of beam limiting devices alone increased the average estimated MTF by as much as 7.0% \pm 0.9%. While the slit method is inherently very sensitive to misalignment, both edge techniques were found to tolerate misalignments by as much as 6 cm. The results suggest the use of the opaque edge test device and the tube internal collimator for beam limitation in order to achieve an MTF result most reflective of the overall performance of the imaging system and least susceptible to misalignment and scattered radiation. Careful attention to influencing factors is warranted to achieve accurate results. © 2006 American Association of Physicists in Medicine. [DOI: 10.1118/1.2188816]

Key words: Modulation transfer function (MTF), linear systems analysis, digital radiography, image quality, resolution, glare, edge, slit, IEC 62220

I. INTRODUCTION

Commencing with the commercial introduction of computed radiography (CR) in 1983, the past two decades have witnessed a gradual transition from analog to digital radiography.^{1,2} This transition has been largely fueled by the

practical advantages of digital technology, including electronic image transmission, image post-processing, and soft-copy display. Concerned about the adequacy of image quality, the scientific community has taken up the task of quantifying the performance of these new digital systems in

TABLE I. Characteristics of the beam qualities and exposure conditions used in the study (No APT = no apertures; Ext APT = external apertures; Int APT = internal collimator apertures).

Method	Test device	Beam quality			Apertures	
		Designation	kV	Filtration		
A (Dobbins <i>et al.</i>)	Slit	A	70	0.5 mm Cu	6.7 mm Al	No
B (Samei <i>et al.</i>)	Translucent edge	B	70	19 mm Al	6.6 mm Al	No
		C (IEC RQA5) No APT				No
C (IEC)	Opaque edge	C (IEC RQA5) Ext APT	74	21 mm Al	7.1 mm Al	2 external (per IEC) internal
		C (IEC RQA5) Int APT				

terms of conventional analog metrics of image quality, now adapted to digital systems. The principle metrics include the modulation transfer function (MTF), the noise power spectrum (NPS), and the detective quantum efficiency (DQE), for which results have been documented in prior publications for many commercial digital radiography systems.^{3–8}

A review of the literature indicates that various investigators have used slightly different approaches to measure the MTF, the NPS, and the DQE. The differences can easily influence the results, and, as a consequence, results from various laboratories obtained for different systems cannot be easily compared. The comparison of published results have also often been complicated by the fact that prior studies have been performed using different test devices, acquisition conditions (e.g., spectral qualities, filtration, and kilovoltage), or processing conditions (e.g., different filtering approaches and algorithmic implementations), even within a chosen method. Partly to address this problem, an international committee recently developed a standard for measuring these quantities.⁹ However, that by itself has added yet another method to the list, making it difficult to compare newly published results with those previously published in the literature. The investigators represented in the authorship of this paper have themselves over the years been involved with many such measurements using two separately developed methods. While those methods have been the basis of numerous prior publications,^{1,5,7,8,10–29} there has never been a side-by-side comparison of the two methods. Furthermore, without a side-by-side investigation, it is difficult to compare the results of those methods to those obtained using the new international standard.

To assess the MTF of radiographic systems, two general approaches have been used in the past: angulated slit and angulated edge. Both techniques use the detector response to a predefined input to measure the MTF.^{3,10} The edge method is typically implemented by using either a translucent edge or an opaque edge, which are characterized primarily by the difference in their radiolucency.^{9,25} The opaque edge method is the technique endorsed by the IEC standard.⁹ Given the differences in the methods that are based on three different test tools, it is not possible to compare results from different

MTF measurements without knowing the extent of the variation that might have been caused by the specific differences within the methods themselves.

We recently undertook a comprehensive study aimed at comparing the relative performance of the three aforementioned methods, a method by Dobbins *et al.*⁷ (hereafter denoted as method A), a method by Samei *et al.*^{4,25} (hereafter denoted as method B), and the IEC method⁹ (hereafter denoted as method C). In the current study we focused not only on the methods as a whole, but also on each method's various acquisition and processing components. The study further aimed to serve as the first independent scientific evaluation of the new standard, placing it in the context of prior established methods. The results of the study were organized into two papers. This paper is focused on the MTF methods. Similar intercomparisons of the NPS are reported in the subsequent concurrent paper.³⁰

II. METHODS

The three MTF methods compared in this paper differed in terms of their various acquisition and processing components (e.g., beam quality, test device, analysis technique). Table I provides a list of some of these differing components. This study was designed to compare not only the methods (including all of their differing components), but also the relative impact of each individual component defining a MTF method. In the following sections we describe the details of the employed test devices, imaging system, beam conditions, image acquisition, and the MTF processing.

A. Test devices

Three MTF test devices were used in the study: a slit for method A, a translucent edge for method B, and an opaque edge for method C. The slit test device⁷ was constructed of two 2 mm thick pieces of Pb with polished edges placed at a small distance from each other forming a slit 35 mm long and 12.5 μm wide. The translucent edge test device⁵ was constructed of a 0.1 mm thick Pt_{0.9}Ir_{0.1} alloy foil, laminated between two thin slabs of acrylic and polished on all four sides to form a 5 \times 5 cm² square test device. The opaque

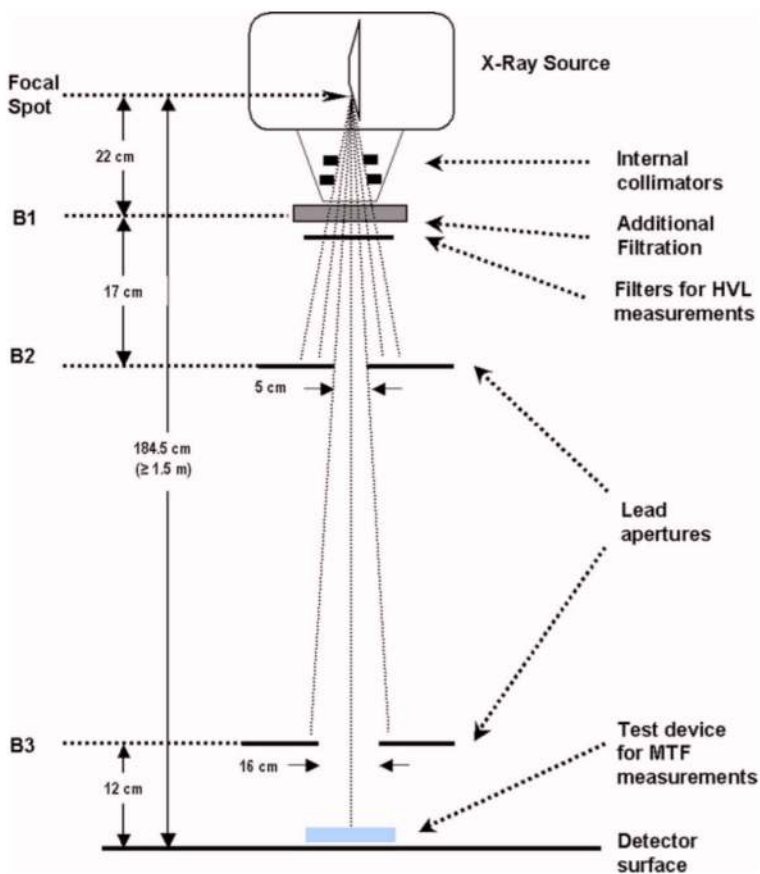


FIG. 1. A schematic of the data acquisition set up including the two apertures recommended by the IEC standard.

edge (TX5 W Edge Test Device, Scanditronix Wellhöffer, Schwarzenbruck, Germany) was made of a 2 mm thick W slab, $5 \times 10 \text{ cm}^2$, polished on one side and surrounded on the other three sides by a 3 mm thick Pb frame. This device was used to measure the MTF according to method C (IEC standard) requiring a test device with thickness greater than or equal to 1 mm.⁹

B. Imaging system

All the MTF measurements and comparisons were made on a prototype indirect flat-panel imaging device. Since the focus of the study was a comparison across different methods and not across different imaging devices, a single representative imaging device was used. The device, similar to its commercial equivalent (Revolution XQ/i, GE Healthcare) and coupled to a standard x-ray tube and generator, is currently used in our laboratory for radiographic research. The detector had a 0.2 mm pixel pitch, and provided a $41 \times 41 \text{ cm}^2$ (2048×2048 pixels) field of view. The device was initially calibrated for gain nonuniformities and defective pixels following the manufacturer's recommendations. The calibration produced a gainmap that was used by the manufacturer's acquisition and processing software to correct for pixel-to-pixel variations in detector response. The calibration and subsequent image acquisitions were performed without

the originally installed antiscatter grid, faceplate, and automatic exposure control sensor. All images were acquired using the same calibration gain map.

C. Beam conditions

Three beam qualities were employed corresponding to those used historically by two of the coauthors (method A used by Dobbins *et al.* and method B by Samei *et al.*), and the IEC-specified RQA5 beam quality (method C). All techniques, listed in Table I, used a tube voltage of approximately 70 kilovoltage (kV) with various amounts of external tube filtration. Beam qualities for methods A and B used 70 kV with the specified amount of Cu and Al filtration, respectively. Beam quality for method C, per the IEC requirement, was achieved by using a specific amount of Al filtration (i.e., 21 mm) while altering the nominal voltage of 70 kV to obtain a required half-value layer (HVL) (i.e., 0.485–0.515 transmission) of 7.1 mm Al. The desired HVL was achieved at 74 kV.

Both Al-based techniques used an Al type-1100 filtration since higher purity Al metals, as specified by the IEC requirement for the RQA5 technique,³¹ were not found to have adequate uniformity.³² The IEC guidelines further required the use of two beam-limiting Pb apertures for the MTF measurement. Based on those guidelines, 2 mm thick Pb sheets were used to construct a $5 \times 5 \text{ cm}^2$ and a $16 \times 16 \text{ cm}^2$ aper-

ture. The two apertures were placed on the beam axis at 39 cm from the focal spot and at 12 cm from the detector, respectively (Fig. 1). To investigate the impact of beam limitation on the MTF estimate, the RQA5 beam quality was used under three conditions: without the external apertures (i.e., no APT), with the external apertures (i.e., Ext APT), and with the tube collimator limiting the beam to the same area as that of the external apertures (i.e., Int APT).

D. System response function

Prior to image acquisition, the linearity of detector response, given by the relationship between digital units and exposure, was determined for methods A, B, and C independently. No external apertures were used in this determination, except for the fact that the beam was tightly collimated to maintain a narrow beam condition ($5.5 \times 6.5 \text{ cm}^2$ at 90.5 cm).

Exposures were measured using a calibrated ionization chamber (MDH Model 1015, 10X5-6 ionization chamber, Radcal, Monrovia, CA) positioned at the approximate center of the beam axis at 90.5 cm from the focal spot. The detector was removed from the field of view. The probe was irradiated using the narrow beam geometry at various exposures (E) over a range of tube output from 0.25 to 64 mAs. For $E \geq 1 \text{ mR}$, the exposure was determined from an average of three exposure measurements. For $0.5 < E < 1 \text{ mR}$ and $E \leq 0.5 \text{ mR}$, the exposure was determined from averages of five and ten integrated exposures, respectively, repeated three times. For all measurements, exposure in the detector plane was estimated using the inverse square law.

Using the same narrow beam geometry, three uniform images were acquired at each of the mAs settings at which the exposures were measured. In these image acquisitions, the ionization probe was positioned within the beam but off the central axis for quality control purposes. This process was repeated for all three beam qualities. No image processing was applied, except for gain and bad pixel corrections noted earlier. From each acquired image, the mean pixel value was calculated within a centrally positioned 100×100 pixel ROI. System response functions were then computed from a linear fit of the averaged mean pixel values versus measured average exposures at each mAs setting over the range of 0 to 2 mR.

The linear fit to the data used a zero intercept. This choice was due to the precision limits of the exposure meter, which made it difficult to accurately measure the low-exposure response. Such inaccuracies at low exposure substantially impact the determination of the tails of LSF measurements in the slit method. Thus, in keeping with our previous experience with this detector and based on information from the manufacturer, we assumed a zero intercept, further substantiated by the fact that pixel values behind Pb-masked areas were essentially zero (i.e., within the noise).

E. Image acquisition

Each test device was placed in contact with the detector cover (or nearly so for the case of a slit; noted below),

aligned with the central axis of the x-ray beam, and then imaged at the specified beam qualities. The approximate exposure to the detector (without the device present) was 7.7, 3.7, and 4.0 mR for beam qualities associated with methods A, B, and C, respectively. Note that for the opaque edge device, these exposures were higher than those recommended by the IEC standard.⁹ However, since the MTFs of indirect flat-panel detectors rarely show an exposure dependency,^{25,33} higher exposure values were used to reduce the amount of noise in the image. All image processing was turned off except for gain and bad pixel corrections noted earlier. All the images were acquired using a 184.5 cm source-to-detector distance (SDD) and a 0.6 mm nominal focal spot.

For the slit test device, the slit was 6 mm away from the detector cover, and about 16 mm from the actual internal detector surface. The device was precisely aligned using an iterative technique in which the test device was sequentially rotated until a maximum slit transmission was obtained, corresponding to the best alignment.⁷ The rotation axis was parallel to the plane of the detector and roughly parallel to the slit itself. The slit was placed at an approximate angle of 2 degrees with respect to the detector pixel array to enable the determination of the presampled MTF. Once aligned, the slit was imaged 20 times.

For the edge test devices, the devices were simply placed such that a polished edge was projected at the visual center of the field of view. The edge was on the detector cover about 10 mm from the actual internal detector surface. The edge was otherwise angled by 2° – 3° with respect to the detector pixel array. The edge test devices were then imaged three times at each of the specified beam conditions. In order to further investigate the influence of edge misalignment on the results, the edges were also sequentially shifted by up to 10 cm away from the center of the field of view.

To minimize detector lag effects, images were acquired with a minimum time interval of 2 min. In addition, apertures were used in a progression from full field to limited field of view with a minimum interval of 10 min between aperture configurations and a minimum of 12 h between MTF evaluations employing different devices. All MTF data were acquired within a short time span using the same detector gain and bad pixel calibration maps.

F. MTF processing

The slit and edge images acquired above were processed using established analysis routines. For the slit images, a previously documented analysis method (method A) was used.^{1,7} The 20 acquired images were summed to provide adequate noise properties in the tails of the line spread function (LSF). An initial evaluation of the transmission through the slit was made to determine three segments along the length of the slit, where the MTF could be reliably determined. With the slit oriented vertically, the angle of the slit pattern within the image was then determined by evaluating the x and y locations of the uppermost and lowermost parts of the image of the slit. This angle information was then used

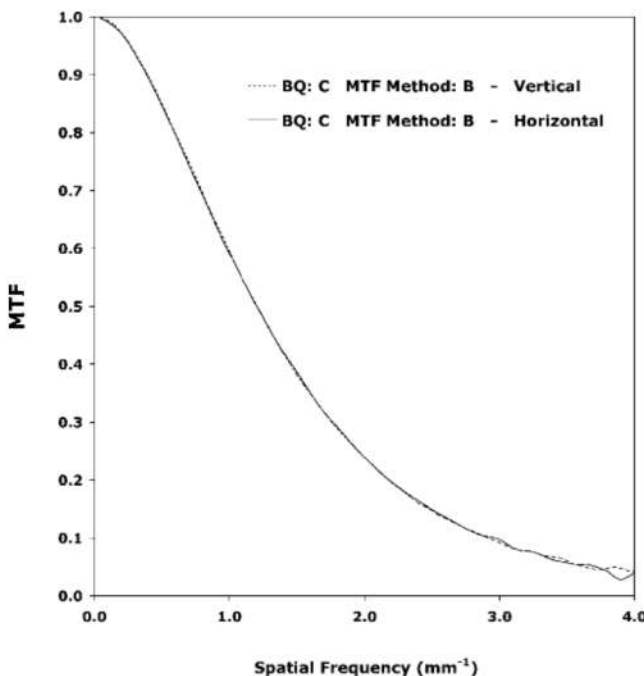


FIG. 2. MTF estimate in the horizontal and vertical directions obtained with a translucent edge (method B) at 74 kV and 21 mm Al filtration (method C) beam quality (BQ). Error bars $<\pm 0.003$.

to sort individual pixels from a 25 (vertical) \times 200 (horizontal) pixels (5×40 mm) region around the slit into a vector of the pixel value versus the perpendicular distance from the slit center, forming the LSF. The integral of exposure values across each row perpendicular to the slit was used to normalize out slight imperfections along the slit. In order to improve the estimate of that integral, pixel values less than a threshold of 4 (values essentially within the noise) were excluded.

The finely sampled LSF from the slit was resampled and interpolated to ensure no missing data values, and then the tails were extrapolated exponentially for all data values below 1% of the LSF peak. The LSF data were Fourier transformed and the absolute value of Fourier transform was normalized by the zero-frequency component to give the MTF. The MTF estimates determined from three slit segments were averaged to improve precision of the measurement. The resulting MTF estimate was divided by a sinc function to account for the estimated 18 μm width of the x-ray projection of the slit (including the estimated focal spot blur).

The image processing techniques used for processing the edge images were identical to those disclosed previously.²⁵ First, the portion of image containing the edge transition was extracted. The extracted region for the translucent edge was 34 \times 34 mm. The extracted region for the opaque edge was 50 mm along the edge and 100 mm perpendicular to the edge per the IEC specification.⁹ The exact angle of the edge was then determined by thresholding and gradient operations followed by a double Hough transformation. The original edge data in the extracted region were then projected along the edge line and binned into 0.02 mm spacing forming the

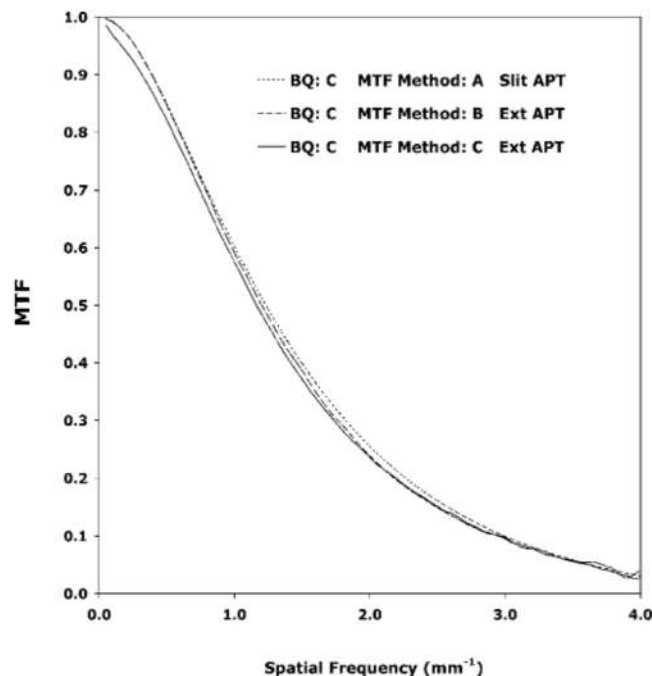


FIG. 3. Dependence of the MTF estimate on the measurement method, independent of beam quality. Test instruments included a slit (method A), a translucent edge (method B), and an opaque edge (method C). All data correspond to method C beam quality (BQ) (IEC RQA5) with two IEC-specified apertures, but method A had its own inherent aperture (slit APT). Error bars $<\pm 0.0002$, ± 0.003 , and ± 0.004 for methods A, B, and C, respectively.

edge spread function (ESF). This process is similar to the method used for slit data in which the distances between the pixels and the slit were used to form the LSF. The ESF was modestly smoothed using a moving Gaussian-weighted polynomial fit. This process was essentially equivalent to convolution with an appropriately chosen kernel. The smoothed ESF was differentiated to obtain the LSF. The LSF was then Fourier transformed and its absolute value normalized at zero frequency to obtain the presampled MTF. The MTF estimates obtained from the three repeated edge images were averaged to achieve a higher precision in the MTF estimate. All MTF data were averaged into 0.05 mm⁻¹ bins per the IEC specification to facilitate a comparison of the data.

G. Simulated slit and edge images

In order to evaluate the absolute accuracy of the processing algorithms, in addition to the experimental images, synthetic slit and edge images were created with an analytically predetermined MTF.³⁴ A perfect 512 \times 512 edge image was formed, assuming a 0.2 mm pixel size, a maximum pixel value of 16 383, a minimum pixel value of 10, a 2° edge angle, and a blur on the edge only associated with that of the partial pixel coverage by the edge. To form simulated slit images, two translationally offset ideal edge images were subtracted from each other, forming a synthetic image of a slit with a nominal 20 μm opening. No further blurring was applied to these synthetic images, and thus both simulated

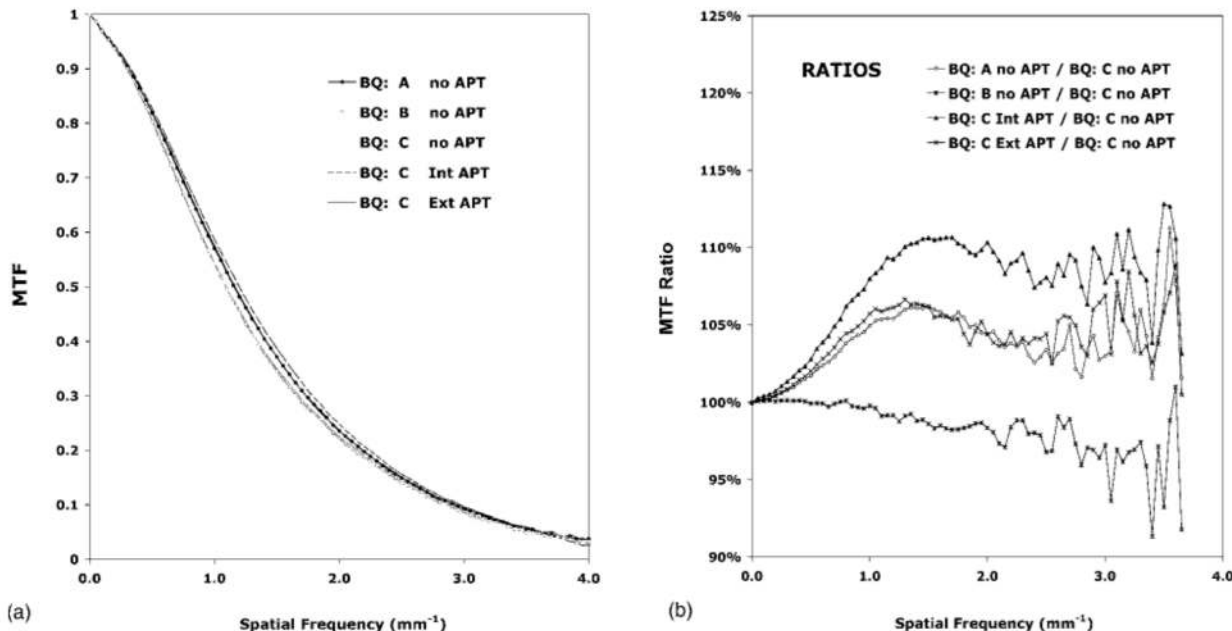


FIG. 4. MTF dependence on beam quality (BQ) using an opaque edge. The five plotted lines in (a) correspond to 70 kV with added 0.5 mm Cu filtration (method A), 70 kV with added 19 mm Al filtration (method B), and 74 kV with 21 mm Al (IEC RQA5, method C) with IEC-specified apertures (Ext APT), without IEC-specified apertures (no APT), and with beam limiting achieved by the internal tube collimator (Int APT) giving the same field size as that of the IEC aperture technique (Ext APT). Error bars <±0.004. (b) Ratios of MTF estimates with respect to the MTF obtained with method C, no aperture. Error bars <±0.9%.

images had a MTF that could be represented with a sinc function associated with a 0.2 mm pixel size.

Actual radiographic images of test devices include fluctuations associated with quantum and instrumentation noise as well as broad-range, low-frequency signal spreading processes often referred to as glare or veiling glare.^{35–37} In order to further characterize the impact of image noise and glare on the accuracy of the MTF estimates, additional versions of the simulated edge and slit images were thus created by adding noise and glare to the simulated images. Noisy versions of the simulated images were formed by adding uncorrelated Poisson noise to the images with a standard deviation equal to the square root of the pixel value. For degradation by the glare, the simulated noiseless images were convolved with a Gaussian glare function,

$$G(f) = \exp\left[-\frac{1}{\ln(2)}\left(\frac{\pi w f}{2}\right)^2\right], \quad (1)$$

where f is the spatial frequency, and w is the full-width at half maximum of the Gaussian function, characterizing the glare in the spatial domain. An ad hoc value of 5 mm was assumed for the parameter w as a likely spatial representation of the extent of glare in a structured phosphor detector. That corresponds to a glare MTF of 0.5 at approximately 0.1 mm⁻¹. The convolution, performed in the spatial frequency space, used a MTF modification routine previously developed in our laboratories.³⁸ Strictly speaking, the convolution of sampled data is not equivalent to sampling convolved data. However, in our case, the sampling was sufficiently fine compared to w that this effect could be considered negligible. The convolved edge and slit images

were then added to the simulated images using

$$I_{wg} = cI_{glare} + (1 - c)I_{ideal}, \quad (2)$$

where I_{wg} is the simulated resultant image including glare, I_{glare} is the image convolved with the glare function, I_{ideal} is the simulated original image, and c is a factor indicating the amount of added glare, set equal to 0.1 for the purpose of this study.

The simulated edge and slit images were processed similarly according to their respective methods described previously. For the slit images, a 30 (vertical) × 200 (horizontal) pixel region was used, with pixel values less than a threshold of 20 excluded from analysis (a higher threshold than the previous value of 4 was used due to a nonzero background in the simulated slit images). For the edge images, a default analysis area of 40 × 40 mm was used. The simulated edge images with glare were further processed multiple times using different analysis areas, from 20 to 100 mm squared, to assess the impact of the analysis area on the estimated glare in the resultant MTF estimates.

III. RESULTS

Overall comparisons of MTF estimates using methods A, B, and C are presented in this section, along with results of subcomparisons of various factors that influence MTF estimates.

A. System response function

The system response function demonstrated excellent linearity ($R^2 > 0.9999$ in all cases) within the evaluated expo-

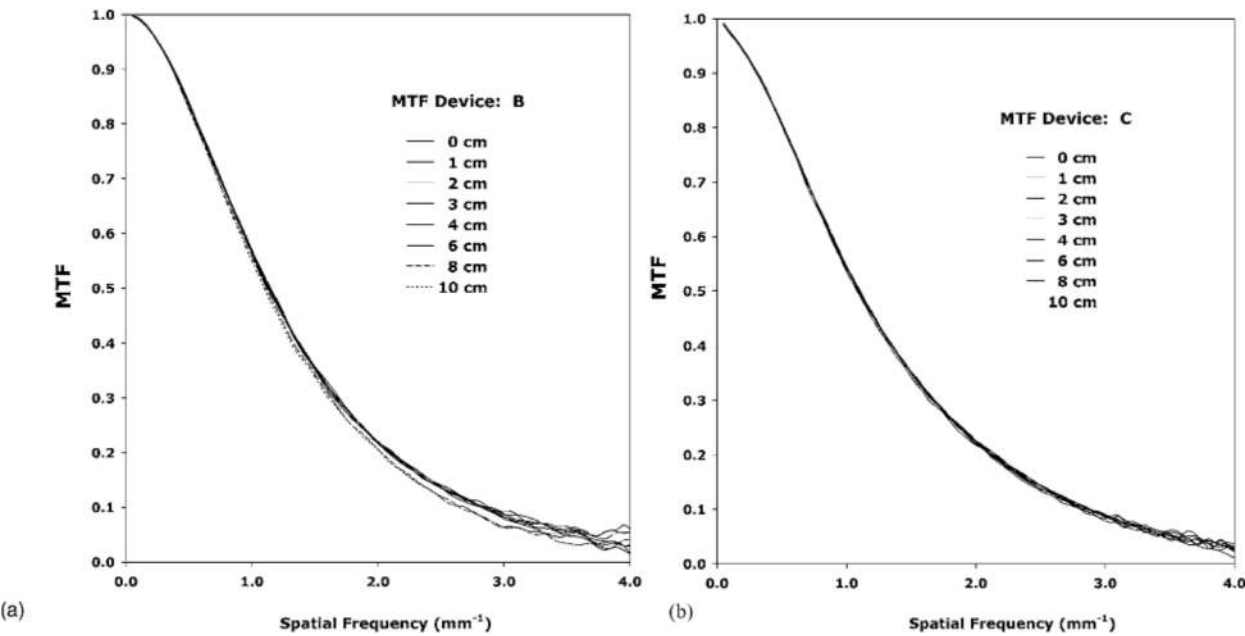


FIG. 5. Impact of edge alignment on MTF estimate for (a) method B translucent and (b) method C opaque edges using method C beam quality (74 kV and 21 mm Al filtration). The ratios of misaligned edge MTF estimates and perfect alignment MTF estimates are tabulated in Table II. Error bars $<\pm 0.004$.

sure range of interest. The original data showed an exposure intercept very close to zero, further confirming the assumed zero intercept for the fits to the system response functions, as noted earlier. The method C (IEC RQA5) beam quality exhibited a slightly higher slope than that obtained using either the beam qualities of methods A or B. The slopes for the beam qualities of methods A, B, and C were 1771.3, 1772.6, and 1841.9 digital value per mR, respectively.

B. Directional dependence

Figure 2 illustrates the directional dependence of the MTF estimate. In general, there is very little difference between the MTF estimates in the horizontal and vertical directions ($0.4\% \pm 0.4\%$ averaged over the zero to cutoff frequency). Slight differences are due to the fluctuations typical of the MTF estimates obtained using the edge method at high spatial frequencies. As the DQE is limited to the cutoff frequency (f_c) of 2.5 mm^{-1} , these minimal differences in MTF estimate due to directional dependence have virtually no impact on the DQE estimate. As a result, only horizontal MTF data are reported in the remainder of the paper.

C. Impact of measurement method independent of beam quality

Figure 3 illustrates a comparison of the MTF estimates obtained by the three measurement methods using the same beam quality (IEC RQA5, per method C). At low spatial frequencies ($< 1 \text{ mm}^{-1}$), the translucent edge and slit results are identical while the MTF estimate from the opaque edge is slightly lower. In the $1\text{--}2 \text{ mm}^{-1}$ range, the results from the translucent edge gradually shift downward toward those of the opaque edge. In the $2\text{--}4 \text{ mm}^{-1}$ range, the slit results

similarly shift to meet the other two MTF estimates. The estimated MTF from the slit measurement was higher than those from the translucent and opaque edges by $7.6\% \pm 0.6\%$ and $7.8\% \pm 0.6\%$ at the cutoff frequency, respectively. Averaged over frequencies up to f_c , the corresponding average relative differences were $3.2\% \pm 0.3\%$ and $5.2\% \pm 0.2\%$, respectively.

D. Impact of beam quality

Isolating the impact of beam quality alone, Fig. 4 illustrates the measured MTF estimates using the opaque edge at different beam qualities. The beam quality appears to have a modest impact on the MTF estimate. When averaged over all frequencies up to f_c , the MTF estimates for the beam qualities of method A (70 kV with 0.5 mm Cu filtration) and method B (70 kV with 19 mm Al) differed from those of method C (IEC RQA5, 74 kV, 21 mm Al) by $+3.7\% \pm 0.9\%$ and $-0.9\% \pm 0.9\%$, respectively (without external beam apertures).

E. Impact of external beam apertures

Referring again to Fig. 4, the presence of external apertures increased the MTF estimate by an average of $4.0\% \pm 0.9\%$ compared to the condition without apertures. The use of the tube internal collimator as the beam-limiting device had even a greater impact, increasing the MTF estimate by $7.0\% \pm 0.9\%$, averaged over frequency, relative to the condition without apertures. The impact of apertures may be attributed to the reduction of scattered radiation generated in the filtration from the beam, enhancing the edge sharpness. However, it is likely that some scattered radiation might still be created from the edges of the external aperture

TABLE II. The ratio of the MTF acquired with translational misalignment of an edge to that obtained with no misalignment averaged over the frequency range of $0\text{--}2.5\text{ mm}^{-1}$.

Misalignment	Translucent edge ($\pm 0.4\%$)	Opaque edge ($\pm 0.3\%$)
1 cm	1.01	0.98
2 cm	1.00	1.01
3 cm	0.99	0.98
4 cm	0.97	0.99
6 cm	1.01	0.99
8 cm	0.97	0.96
10 cm	0.96	1.00

closest to the detector degrading the MTF. This is consistent with the observed slight increase in the estimated detector exposure with added external apertures noted in the concurrent paper.³⁰

F. Impact of edge alignment

Figure 5 illustrates the impact of edge alignment on the resulting MTF estimate for both the translucent and opaque edge devices (per methods B and C) using the method C beam quality (RQA5, 74 kV, 21 mm Al filtration). For both devices, the MTF estimate remains relatively stable at up to 6 cm of misalignment above which the translucent edge exhibits a reduction in the MTF estimate. To further illustrate this finding, Table II tabulates the ratio of each MTF estimate obtained in a misaligned edge condition to that of perfect alignment, averaged over the frequency range of interest. While the average relative difference is in the range of 0%–2% ($\pm 0.4\%$) for both devices with small amounts of misalignment, that estimate exceeds 3.0% $\pm 0.4\%$ beyond 8 cm misalignment. The increased sensitivity to misalignment of the translucent edge is not intuitive because its reduced thickness (compared to the thickness of the opaque edge device) would suggest that it might be less susceptible to the degradation of the MTF estimate resulting from the edge partial-penetration penumbra. However, the behavior may be explained by the partial-penetration penumbra associated with the 2 mm thick acrylic laminate of the device.⁵

G. Overall comparison of the methods

Considering all factors combined, Fig. 6 illustrates the overall comparisons of methods A, B, and C. The results of the three methods converge at about 3.5 mm^{-1} . However, below that frequency, method A provides a consistently higher MTF estimate than the other two methods. Between 0 and 0.85 mm^{-1} , method B provides a MTF estimate higher than that of method C, but vice versa beyond 0.85 mm^{-1} . Most of the differences observed may be attributed to the three underlying differences: the differences in the test device, the beam quality, and the beam limitation technique outlined earlier. At the cutoff frequency, the estimated MTF from method C was $3.7\% \pm 0.6\%$ lower than that of method A, and $9.7\% \pm 0.9\%$ higher than that of method A. Averaged

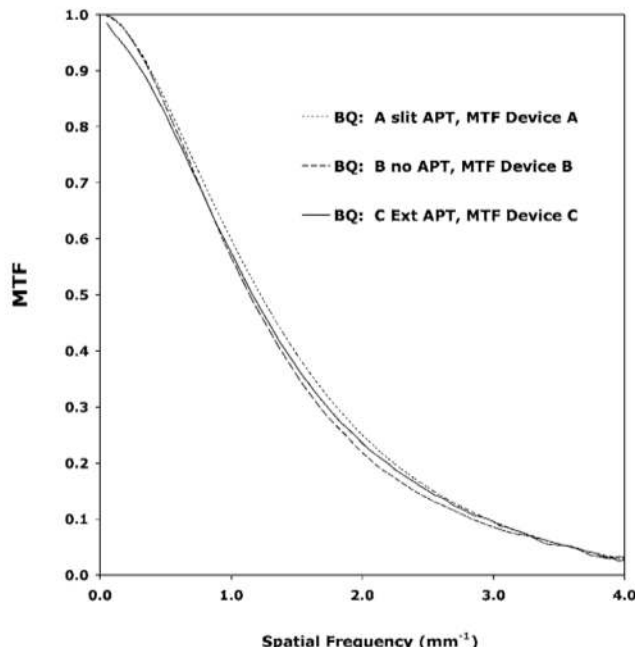


FIG. 6. Dependence of the MTF overall method on the MTF estimate. Methods employed a slit (method A), a translucent edge (method B), and an opaque edge (method C), each with its own associated beam quality (BQ): 70 kV with added 0.5 mm Cu filtration (method A), 70 kV with added 19 mm Al filtration (method B), and 74 kV with 21 mm Al (IEC RQA5, method C); with the inherent beam limiting achieved by the slit test device (Slit APT) for method A, without beam limitation (no APT) for method B, and with IEC-specified apertures (Ext APT) for method C. Error bars $<\pm 0.0002$, ± 0.003 , and ± 0.004 for methods A, B, and C, respectively.

over frequencies up to the cutoff frequency, the corresponding average relative differences were $4.0\% \pm 0.2\%$ and $0.7\% \pm 0.4\%$, respectively.

H. Absolute accuracy as determined by simulated edge and slit

A question, which naturally arises from the above results, is which analysis method provides a MTF estimate closest to the true MTF of the device. Figure 7(a) illustrates the results of the three analysis methods applied to the simulated edge and slit data in the absence of image glare. The MTF estimate from the edge method is generally lower than the expected true MTF, approaching a difference of 5.2% at the cutoff frequency. In comparison, the MTF estimate from the slit is very close to the true MTF, differing by only 0.3% at the cutoff frequency. The lower performance of the edge MTF estimate may be attributed to the LSF smoothing process documented previously.²⁵ The edge method is also more susceptible to noise within the image caused by the differentiation process involved in the analysis.^{25,39}

The above observations are relevant to the situation in which no image glare is present. Figure 7(b) presents the MTF estimates using the simulated edge and slit in the presence of simulated glare. The MTF estimate from the slit method does not change appreciably when glare is in the image, while the edge method MTF estimates are much more sensitive to the presence of glare. The sensitivity of the edge

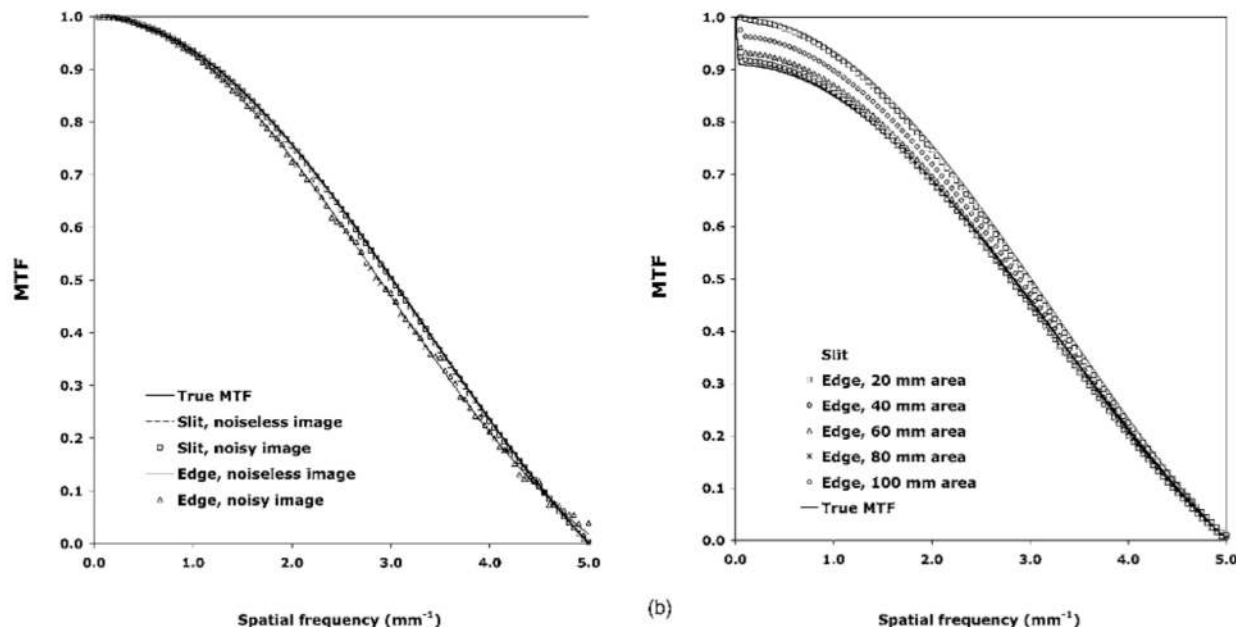


FIG. 7. Presampled MTF estimates from the simulated slit and edge images with and without added uncorrelated noise. Also shown is a sinc function depicting the true MTF (a). A presampled MTF estimate obtained with the simulated noiseless edge and slit images with 10% added glare (b). The edge image was analyzed using different square analysis areas, 20–100 mm in size.

method to glare is a direct function of the size of the image area used for analysis, with the best depiction of the glare indicated when a large area of the image ($>8 \times 8 \text{ cm}^2$) is used. As a larger area of the edge image is analyzed, a larger extent of the broad glare is included in the analysis, leading to increased low-frequency content; after normalizing the MTF by the zero-frequency value, the low-frequency glare causes a general reduction of the MTF estimate across all frequencies. Using an $8 \times 8 \text{ cm}^2$ region of analysis in the presence of 10% simulated glare, the edge method gives a maximum error of 1.7% relative to the true MTF, whereas the slit method has a maximum error of 10.0%.

IV. DISCUSSION

The MTF has been recognized as the established metric for characterizing the resolution performance of an imaging system.^{3,40,41} For many years, the slit technique was considered the state-of-the-art method to measure the MTF of radiographic imaging systems.^{7,16,42–46} However, given its somewhat cumbersome alignment requirements, an alternative MTF measurement technique using an edge test device was employed by a number of investigators.^{25,28,34,47,48} The edge technique, while less precise,³⁹ had a less rigorous alignment requirement and could provide an excellent definition of the low frequency MTF. Two types of edges were used by investigators, a translucent edge, which would transmit 10%–50% of x rays impinging upon it, and an opaque edge that would essentially absorb all x rays. The opaque edge technique was recently endorsed by the IEC international standard,⁹ while the use of slit and translucent edge methods has continued in parallel.

In this study, we performed a comprehensive investigation to determine the relative accuracy of the slit and edge methods using data obtained from a single but representative digital radiographic system. We further investigated the impact of potential influencing factors such as beam quality, MTF device alignment, size of the analysis area, and the use of beam-limiting devices, both external (via IEC-specified apertures) and internal (via collimator). The results of this study enable the comparison of previously published MTF results obtained using two established methods (methods A and B) with one another and with those from the new IEC-specified method (method C).

Our findings indicate that measurement technique has a notable impact on the resulting MTF estimate, with estimates from the overall method C $4.0\% \pm 0.2\%$ lower than that of method A and $0.7\% \pm 0.4\%$ higher than that of method B averaged over the zero to cutoff frequency range. Isolating the impact of the test device alone, the MTF estimates obtained with the edge devices were a maximum of $7.8\% \pm 0.6\%$ ($5.2\% \pm 0.2\%$ averaged over the zero to cutoff frequency range) lower than that of the slit. The use of beam-limiting devices increased the frequency-averaged MTF estimate by as much as $7.0\% \pm 0.9\%$. Isolating the impact of beam quality alone, at typical nominal 70 kV radiographic energies, the spectrum of method A was found to yield a higher MTF estimate than that of method B ($4.7\% \pm 0.9\%$ averaged over frequency). The results of the method C spectrum were only slightly higher than those of method B ($\sim 0.9\% \pm 0.9\%$). The size of the analysis area of an opaque edge was found to impact the MTF estimate, while both edge techniques were found to tolerate misalignments by as much as 6 cm. These dependencies and trends should be taken into

consideration when comparing published results based on various methods and beam qualities. Furthermore, even though the impact of the parameters studied in this work on estimated MTF is relatively modest, even a modest impact should not be overlooked, as the resulting effect would be much more pronounced in the DQE, since the DQE is proportional to the square of the MTF.

While the slit was found to give MTF estimates that were both more precise and more accurate than those of the edge technique in the absence of glare, in the presence of glare, the opaque edge gave substantially better accuracy than either the slit or translucent edge at low frequencies. It is worthwhile to note that the poorer precision of the edge technique in estimating the high-frequency component of the MTF is not an inherent limitation of the technique. In this study, we applied a smoothing operation to the edge data in order to reduce the noise enhanced by the differentiation process. However, in lieu of smoothing, a larger number of edge images could be averaged to reduce uncertainty in edge response measurements, and thus this disadvantage of the edge technique can be minimized. However, such is not the case with the low-frequency disadvantage associated with the use of the slit technique. The low-frequency components with the slit are dependent on the long tails of the LSF. Those tails are difficult to estimate due to the difficulty in recording enough exposure to adequately represent the tails. It is possible to characterize these long tails better with computed radiography (CR) detectors than flat-panel receptors if one exposes the CR screen with multiple high exposures prior to readout. It is not possible to do such an on-the-plate integration with flat panel receptors. Even with CR, the plate can get close to saturation in the center of the slit before the tails are adequately recorded. Thus, the limitations of the slit technique at low frequencies are not easily overcome, and the opaque edge is seen to provide the most accurate results in the presence of glare.

Notwithstanding the findings of this study, their scope and limitations should be clearly recognized. This investigation was limited to only one type of image receptor, namely an indirect flat panel for general and chest radiographic applications, because the goal of the study was not an intercomparison of methods across *different* imaging technologies, but rather the comparison of different methods applied to the *same* imaging system. An important question arises as to how the relative differences between MTF methods noted in this paper can be related to the MTF measurements reported in other studies, particularly those using different imaging systems. We believe the most appropriate claims are the following: (1) For other studies using the same type of flat-panel system as used here, a quantitative correction could be applied to relate other MTF measurements to the three MTF measurement methods described in this paper. (2) The percent differences between MTF methods shown in this work are likely to be reflective of the general magnitude of differences to be expected due to measurement methods when applied to other types of imaging systems. (3) It cannot be determined quantitatively what magnitude of difference could be expected if method A on System X were compared

to method B on System Y. Furthermore, the comparisons are only applicable to the beam qualities examined in this study and cannot be readily extrapolated to notably higher (e.g., chest radiography) or lower (e.g., mammography) x-ray energy ranges.

V. CONCLUSIONS

In this study we compared MTF measurement techniques using historical slit and edge techniques as well as the new edge technique recommended by a recent international standard. The findings suggest that the MTF estimate can be moderately impacted by the method used and by image acquisition parameters such as beam quality, beam limitation, and processing technique. Thus, as we have demonstrated, the MTF estimate is dependent on the methodology, and as a result, care must be exercised when comparing MTF results obtained using different methodologies.

Our findings have multiple implications in terms of a preferred method for proper measurement of the MTF.

- (1) The opaque edge method appears to yield MTF results that are the most accurate of the three methods evaluated in the presence of glare. The opaque edge was found to be unaffected by misalignments by as much as 6 cm. At higher energies, a translucent edge is more prone to generating secondary radiation that could impact the estimated MTF,⁴⁹ and thus the opaque edge is the preferred technique for measuring the MTF at kVs higher than 70.
- (2) When using the edge technique, the size of the analysis area has a direct impact on the representation of possible glare in the resultant MTF estimate. An analysis area of about $8 \times 8 \text{ cm}^2$ is close to ideal. Larger sizes would lead to an averaging resolution response across a larger area of the detector, thereby making the measurement prone to the heel effect, detector nonuniformities, and defects in the straightness of the edge. Smaller sizes would not adequately include the glare of the detector.
- (3) Compared to the other two techniques, the slit method appears to provide the highest precision, with a very small uncertainty of measurement, even at high frequencies. The slit method was also the most accurate of the three methods in the absence of glare. However, the slit method did not account for glare. This was due to the fact that the method employs an exponential extrapolation of the LSF below 1% of the peak amplitude, which tends to mask long-range glare attributes of the image. As the opaque edge method provides a better definition of low-frequency drop in the MTF due to glare and is easier to align, the opaque edge method is recommended over the slit method. Averaging multiple images, similar to that done with the slit, may be used to increase the precision of the opaque edge technique.
- (4) The beam quality, even at generally comparable kV and filtrations, does impact the MTF estimate, although modestly, and that should be taken into consideration when planning a measurement or comparing results with other studies.

- (5) Beam-limitation increases the MTF estimate by as much as about 8% likely due to the reduction of scattered x rays. Thus, it is encouraged. However, the x-ray tube collimator does a more effective job in that regard than external apertures required by the IEC standard. Given the fact that the setup of the external apertures is cumbersome and time consuming, the use of tube collimators is preferred.

ACKNOWLEDGMENTS

The authors wish to thank the following individuals: Dr. Carl Ravin of the Duke Radiology Department for his support and assistance during the course of this study; Dr. Cornelia Lipfert of Scanditronix Wellhöfer GmbH for providing an opaque edge test device for the experiment; and Robert Saunders of Duke University for his assistance with the formation of simulated edge data. The flat-panel detector used for evaluation in this study was provided through a research agreement with GE Healthcare. This work was supported in part by grants from the National Institutes of Health (R01 CA80490 and R01 CA109074).

^aThis paper is part of a two-paper series. The readers are advised to also review the concurrent manuscript (Ref. 30).

- ¹C. E. Floyd, Jr., R. J. Warp, J. T. Dobbins III, H. G. Chotas, A. H. Baydush, R. Vargas-Voracek, and C. E. Ravin, "Imaging characteristics of an amorphous silicon flat-panel detector for digital chest radiography," *Radiology* **218**, 683–688 (2001).
- ²M. J. Yaffe and J. A. Rowlands, "X-ray detectors for digital radiography," *Phys. Med. Biol.* **42**, 1–39 (1997).
- ³E. Samei, "Performance of digital radiography detectors: quantification and assessment methodologies," in *Advances in Digital Radiography* [Radiological Society of North America (RSNA) Publication, Oak Brook, IL, 2003], pp. 37–47.
- ⁴E. Samei, J. G. Hill, G. D. Frey, W. M. Southgate, E. Mah, and D. Delong, "Evaluation of a flat panel digital radiographic system for low-dose portable imaging of neonates," *Med. Phys.* **30**, 601–607 (2003).
- ⁵E. Samei and M. J. Flynn, "An experimental comparison of detector performance for computed radiography systems," *Med. Phys.* **29**, 447–459 (2002).
- ⁶P. R. Granfors and R. Aufrichtig, "Performance of a 41×41-cm² amorphous silicon flat panel x-ray detector for radiographic imaging applications," *Med. Phys.* **27**, 1324–1331 (2000).
- ⁷J. T. Dobbins III, D. L. Ergun, L. Rutz, D. A. Hinshaw, H. Blume, and D. C. Clark, "DQE(f) of four generations of computed radiography acquisition devices," *Med. Phys.* **22**, 1581–1593 (1995).
- ⁸K. A. Fetterly and N. J. Hangiandreou, "Effects of x-ray spectra on the DQE of a computed radiography system," *Med. Phys.* **28**, 241–249 (2001).
- ⁹IEC publication, "Medical electrical equipment—Characteristics of digital x-ray imaging devices - Part 1: Determination of the detective quantum efficiency," IEC 62220-1, Geneva, Switzerland, 2003.
- ¹⁰J. T. Dobbins III, "Image Quality Metrics for Digital Systems," in *Handbook of Medical Imaging*, edited by H. K. J. Beutel, H. L. Kundel, and R. L. V. Metter (SPIE, Bellingham, WA, 2000), Vol. 1, pp. 163–222.
- ¹¹J. T. Dobbins III, "Effects of undersampling on the proper interpretation of modulation transfer function, noise power spectra, and noise equivalent quanta of digital imaging systems," *Med. Phys.* **22**, 171–181 (1995).
- ¹²J. T. Dobbins III, H. G. Chotas, and H. Benveniste, "Direct digitization of optical images using a photostimulable phosphor system," *Med. Phys.* **19**, 1071–1080 (1992).
- ¹³R. J. Warp and J. T. Dobbins III, "Quantitative evaluation of noise reduction strategies in dual-energy imaging," *Med. Phys.* **30**, 190–198 (2003).
- ¹⁴H. G. Chotas, C. E. Floyd, Jr., J. T. Dobbins III, and C. E. Ravin, "Digital chest radiography with photostimulable storage phosphors: signal-to-noise ratio as a function of kilovoltage with matched exposure risk," *Radiology* **186**, 395–398 (1993).
- ¹⁵C. D. Bradford, W. W. Peppler, and J. T. Dobbins III, "Performance characteristics of a Kodak computed radiography system," *Med. Phys.* **26**, 27–37 (1999).
- ¹⁶C. D. Bradford, W. W. Peppler, and J. M. Waidelich, "Use of a slit camera for MTF measurements," *Med. Phys.* **26**, 2286–2294 (1999).
- ¹⁷E. Samei, J. Y. Lo, T. T. Yoshizumi, J. L. Jesneck, J. T. Dobbins III, C. E. Floyd, Jr., H. P. McAdams, and C. E. Ravin, "Comparative scatter and dose performance of slot-scan and full-field digital chest radiography systems," *Radiology* **235**, 940–949 (2005).
- ¹⁸E. Samei, R. S. Saunders, J. Y. Lo, J. T. Dobbins III, J. L. Jesneck, C. E. Floyd, and C. E. Ravin, "Fundamental imaging characteristics of a slot-scan digital chest radiographic system," *Med. Phys.* **31**, 2687–2698 (2004).
- ¹⁹E. Samei and M. J. Flynn, "An experimental comparison of detector performance for direct and indirect digital radiography systems," *Med. Phys.* **30**, 608–622 (2003).
- ²⁰E. Samei, "Image quality in two phosphor-based flat panel digital radiographic detectors," *Med. Phys.* **30**, 1747–1757 (2003).
- ²¹E. Samei, M. J. Flynn, H. G. Chotas, and J. T. Dobbins III, "DQE of direct and indirect digital radiographic systems," *Proc. SPIE* **4320**, 189–197 (2001).
- ²²E. Samei, M. J. Flynn, J. T. Dobbins III, and H. G. Chotas, "Comparative assessment of image quality in three flat-panel digital radiographic systems," *Radiology* **221**, 462–463 (2001).
- ²³E. Samei, J. A. Seibert, C. E. Willis, M. J. Flynn, E. Mah, and K. L. Junck, "Performance evaluation of computed radiography systems," *Med. Phys.* **28**, 361–371 (2001).
- ²⁴E. Samei and M. J. Flynn, "Comparison of image quality characteristics in three storage phosphor radiography systems," *Radiology* **213P**, 235–235 (1999).
- ²⁵E. Samei, M. J. Flynn, and D. A. Reimann, "A method for measuring the presampled MTF of digital radiographic systems using an edge test device," *Med. Phys.* **25**, 102–113 (1998).
- ²⁶E. Samei and M. J. Flynn, "Physical measures of image quality in photostimulable phosphor radiographic systems," *Proc. SPIE* **3032**, 328–338 (1997).
- ²⁷K. A. Fetterly and B. A. Schueler, "Performance evaluation of a "dual-side read" dedicated mammography computed radiography system," *Med. Phys.* **30**, 1843–1854 (2003).
- ²⁸K. A. Fetterly and N. J. Hangiandreou, "Image quality evaluation of a desktop computed radiography system," *Med. Phys.* **27**, 2669–2679 (2000).
- ²⁹K. A. Fetterly and N. J. Hangiandreou, "Effects of x-ray spectrum on the NPS of a computed radiography system," *Proc. SPIE* **3977**, 632–639 (2000).
- ³⁰J. T. Dobbins III, E. Samei, N. T. Ranger, and Y. Chen, "Inter-comparison of methods for image quality characterization: 2. Noise power spectrum," *Med. Phys.* **33**, 1466–1475 (2006), following paper.
- ³¹IEC publication, "Medical diagnostic x-ray equipment—Radiation conditions for use in the determination of characteristics," IEC 1267, Geneva, Switzerland, 1994.
- ³²N. T. Ranger, J. T. Dobbins III, and C. E. Ravin, "Measurement of the detective quantum efficiency in digital detectors consistent with the IEC 62220-1 standard: practical considerations regarding the choice of filter material," *Med. Phys.* **37**, 2305–2311 (2005).
- ³³S. Boyce, A. Chawla, and E. Samei, "Physical Evaluation of a high frame rate, extended dynamic range flat panel imager for real-time cone beam computed tomography applications," *Proc. SPIE* **5745**, 591–599 (2005).
- ³⁴E. Buhr, S. Gunther-Kohfahl, and U. Neitzel, "Accuracy of a simple method for deriving the presampled modulation transfer function of a digital radiographic system from an edge image," *Med. Phys.* **30**, 2323–2331 (2003).
- ³⁵M. Flynn, S. Wilderman, and J. Kanicki, "Effect of secondary radiations on the performance of digital radiographic detectors," *Proc. SPIE* **3336**, 326–336 (1998).
- ³⁶I. A. Cunningham, J. Yao, and V. Subotic, "Cascaded models and the DQE of flat-panel imagers: noise aliasing, secondary quantum noise, and reabsorption," *Proc. SPIE* **4682**, 61–72 (2002).
- ³⁷J. A. Seibert, O. Nalcioglu, and W. W. Roeck, "Characterization of the veiling glare PSF in x-ray image intensified fluoroscopy," *Med. Phys.* **11**, 172–179 (1984).

- ³⁸R. S. Saunders and E. Samei, "A method for modifying the image quality parameters of digital radiographic images," *Med. Phys.* **30**, 3006–3017 (2003).
- ³⁹I. A. Cunningham and B. K. Reid, "Signal and noise in modulation transfer function determinations using the slit, wire, and edge techniques," *Med. Phys.* **19**, 1037–1044 (1992).
- ⁴⁰E. Samei, "Performance of digital radiography detectors: factors affecting sharpness and noise," in *Advances in Digital Radiography*, edited by [Radiological Society of North America (RSNA) Publication, Oak Brook, IL, 2003], pp. 49–61.
- ⁴¹K. Rossmann, "Point spread-function, line spread-function, and modulation transfer function. Tools for the study of imaging systems," *Radiology* **93**, 257–272 (1969).
- ⁴²K. Doi, K. Strubler, and K. Rossmann, "Truncation errors in calculating the MTF of radiographic screen-film systems from the line spread function," *Phys. Med. Biol.* **17**, 241–250 (1972).
- ⁴³H. Fujita, K. Doi, and K. G. Chua, "Computerized analysis of stenotic lesions in dsa images by an iterative deconvolution technique," *Med. Phys.* **12**, 505 (1985).
- ⁴⁴F. F. Yin, M. L. Giger, and K. Doi, "Measurement of the presampling modulation transfer function of film digitizers using a curve fitting technique," *Med. Phys.* **17**, 962–966 (1990).
- ⁴⁵H. Fujita, K. Doi, and M. L. Giger, "Investigation of basic imaging properties in digital radiography. 6. MTFs of IL-TV digital imaging systems," *Med. Phys.* **12**, 713–720 (1985).
- ⁴⁶M. L. Giger and K. Doi, "Investigation of basic imaging properties in digital radiography. 1. Modulation transfer function," *Med. Phys.* **11**, 287–295 (1984).
- ⁴⁷J. G. Mainprize, N. L. Ford, S. Yin, T. Turner, and M. J. Yaffe, "Image quality of a prototype direct conversion detector for digital mammography," *Proc. SPIE* **3659**, 398–406 (1999).
- ⁴⁸J. M. Boone and J. A. Seibert, "An analytical edge spread function model for computer fitting and subsequent calculation of the LSF and MTF," *Med. Phys.* **21**, 1541–1545 (1994).
- ⁴⁹U. Neitzel, E. Buhr, G. Hilgers, and P. R. Granfors, "Determination of the modulation transfer function using the edge method: influence of scattered radiation," *Med. Phys.* **31**, 3485–3491 (2004).

Intercomparison of methods for image quality characterization. II. Noise power spectrum^{a)}

James T. Dobbins III

Duke Advanced Imaging Laboratories, Departments of Radiology and Biomedical Engineering, Duke University, Durham, North Carolina 27710

Ehsan Samei

Duke Advanced Imaging Laboratories, Departments of Radiology, Biomedical Engineering, and Physics, Duke University, Durham, North Carolina 27710

Nicole T. Ranger

Duke Advanced Imaging Laboratories, Department of Radiology, Duke University, Durham, North Carolina 27710

Ying Chen

Duke Advanced Imaging Laboratories, Departments of Radiology and Biomedical Engineering, Duke University, Durham, North Carolina 27710

(Received 8 April 2005; accepted for publication 17 February 2006; published 28 April 2006)

Second in a two-part series comparing measurement techniques for the assessment of basic image quality metrics in digital radiography, in this paper we focus on the measurement of the image noise power spectrum (NPS). Three methods were considered: (1) a method published by Dobbins *et al.* [Med. Phys. **22**, 1581–1593 (1995)], (2) a method published by Samei *et al.* [Med. Phys. **30**, 608–622 (2003)], and (3) a new method sanctioned by the International Electrotechnical Commission (IEC 62220-1, 2003), developed as part of an international standard for the measurement of detective quantum efficiency. In addition to an overall comparison of the estimated NPS between the three techniques, the following factors were also evaluated for their effect on the measured NPS: horizontal versus vertical directional dependence, the use of beam-limiting apertures, beam spectrum, and computational methods of NPS analysis, including the region-of-interest (ROI) size and the method of ROI normalization. Of these factors, none was found to demonstrate a substantial impact on the amplitude of the NPS estimates ($\leq 3.1\%$ relative difference in NPS averaged over frequency, for each factor considered separately). Overall, the three methods agreed to within $1.6\% \pm 0.8\%$ when averaged over frequencies $> 0.15 \text{ mm}^{-1}$. © 2006 American Association of Physicists in Medicine. [DOI: 10.1118/1.2188819]

Key words: Noise power spectrum (NPS), linear systems analysis, digital radiography, image quality, noise, IEC 62220-1

I. INTRODUCTION

This paper is part of a two-part series comparing measurement methodologies for the modulation transfer function (MTF) and noise power spectrum (NPS). The NPS is one of the most common metrics describing the noise properties of imaging systems. The measurement of the NPS is conceptually straightforward but difficult to carry out experimentally, and there has not been universal agreement on the best methods for these measurements. Recently, there have been efforts by several bodies, including the AAPM¹ and the International Electrotechnical Commission (IEC),² to develop standards for these measurements. Despite the laudable effort to reach a consensus on the best measurement methodology, there is still a sizable literature of measurements made on various devices by a variety of methods.^{3–19} Because of the variety of methods used, it is difficult to compare previously published NPS results using different methodologies. Therefore, there is a need for an intercomparison of these previously reported methods, as well as a comparison with the new IEC standard, so that investigators may know how to

interpret the results of different studies obtained using these various techniques. In this paper we describe a comparison of methods for a measurement of the NPS reported by Dobbins *et al.*^{3,20} (hereafter, method A), Samei *et al.*^{4,5,14–17} (hereafter, method B), and the IEC standard² (hereafter, method C). In a companion paper we report similar comparisons of methods for measuring the MTF.²¹

II. BACKGROUND

The frequency-dependent NPS, $NPS(f)$, is defined as the variance per frequency bin of a stochastic signal in the spatial frequency domain. For a complete treatment of the derivation of the NPS formula, the interested reader is referred to another text.²⁰ Although it may be computed as the Fourier Transform of the autocovariance function by use of the Wiener-Kintchin Theorem,²² the NPS is most commonly computed directly from the squared Fourier amplitude of two-dimensional image data using

$$\begin{aligned}
 \text{NPS}(u_n, v_k) &= \lim_{N_x, N_y \rightarrow \infty} (N_x N_y \Delta x \Delta y) \langle |\text{FT}_{nk}[I(x, y) - \bar{I}]|^2 \rangle \\
 &= \lim_{N_x, N_y \rightarrow \infty} \lim_{M \rightarrow \infty} \frac{N_x N_y \Delta x \Delta y}{M} \sum_{m=1}^M |\text{FT}_{nk}[I(x, y) - \bar{I}]|^2 \\
 &= \lim_{N_x, N_y, M \rightarrow \infty} \frac{\Delta x \Delta y}{M \cdot N_x N_y} \sum_{m=1}^M \left| \sum_{i=1}^{N_x} \sum_{j=1}^{N_y} [I(x_i, y_j) - \bar{I}] e^{-2\pi i (u_n x_i + v_k y_j)} \right|^2,
 \end{aligned} \tag{1}$$

where $I(x_i, y_j)$ is the image intensity at the pixel location (x_i, y_j) , \bar{I} is the global mean intensity, u and v are the spatial frequencies conjugate to x and y , N_x and N_y are the numbers of pixels in the x and y directions of the digital image, Δx and Δy are the pixel spacings in the x and y directions, and M is the number of regions used for analysis in the ensemble average. Conventionally, the Fourier transform is normalized by dividing by $N_x N_y$.

The zero-frequency component is difficult to measure accurately, and is therefore almost always excluded from analysis. With that exclusion, the subtraction of the global mean in Eq. (1) may be eliminated, and thus only the squared Fourier amplitudes of raw noise data are considered.

Many factors influence the choice of methodology for measuring the NPS. Unfortunately, there is not a universal, standard method that will apply equally well to all situations, and some compromises are necessary, depending on the type of system being measured and the amount of data available. There are two principal difficulties in determining the best method for NPS analysis. The first such difficulty is that only a limited amount of data is available for analysis. The summations in the discrete Fourier transforms in Eq. (1) extend over an infinite spatial domain, but there is clearly not an infinite extent of data available for measurement. Also, the ensemble average in Eq. (1) requires an infinite number of samples to determine the true NPS, but again, an infinite amount of data is not available. Thus, some compromises must be made in order to get the “best” estimate of the NPS from the finite amount of available data. For two-dimensional image data, this compromise involves a trade-off between the size and number of the regions of interest (ROIs) used for analysis. A thorough treatment of the issues in selecting ROI size is beyond the scope of this paper, but another reference may be consulted for additional details.²⁰ In simplest terms, the size of the ROI should contain just enough pixels to adequately demonstrate the structure in the NPS curve. If the NPS curve is smoothly varying with frequency, then a very small ROI may be used; if there are spikes in the power spectrum, then the ROI must contain more pixels in order to have adequate sampling in frequency space so that the shape of the spikes is not adversely impacted. Some investigators have used data windowing (defined as the application of spatial weighting to image data) to further refine the resolution of NPS data in frequency space. Data windowing was not used with one of the methods de-

scribed in this paper (method A in which all pixels analyzed had the same weighting), but a Hamming window was used on the data for the other two analysis approaches (methods B and C).

The second difficulty in making accurate NPS measurements is that practical data contains some static artifactual components in addition to the stochastic noise that one desires to measure. This artifactual structure may manifest itself as background shading due to the heel effect or inverse square exposure variation, or as a fixed pattern due to the structure in the detector. It is almost always desirable to remove shading artifacts because these contribute to the squared Fourier components at low frequency, but do not represent stochastic noise. Various approaches are used in this paper to eliminate background shading artifacts, depending on the NPS measurement method being used. Fixed pattern noise should not be removed from the image used to compute NPS if the noise is spatially stochastic (even though temporally constant), because it contributes to the noise pattern in a given image, hampering an observer’s ability to discern the desired signal from noise. The flat-panel detector used for the NPS measurements in this paper does a gain and offset correction that inherently eliminates a large amount of the stochastic fixed pattern noise; however, a small amount remains, particularly at low frequencies. A subtraction method can be used to determine the amount of residual fixed pattern noise in the NPS.

It is important when evaluating the NPS on a given device to consider the entire two-dimensional NPS. There can be spikes or other noise artifacts that do not show up adequately if a simple one-dimensional plot is examined.³ However, due to the number of intercomparisons in this paper, and due to the fact that the detector being used for measurement has no discernable off-axis noise artifacts, only one-dimensional plots will be presented here. In order to improve the standard error of one-dimensional NPS curves, it is customary to average data from a thick band through two-dimensional frequency space near the axes; methods described herein differ as to whether the on-axis data is included in those averages, and such differences will be noted.

III. METHODS

The three NPS methods compared in this article differ in various acquisition and processing parameters [beam quality, ROI size, configuration and number of ROIs, background

TABLE I. Standard parameters for the NPS methods evaluated. Methods A, B, and C represent methods published by Dobbins *et al.* (Refs. 3 and 20), Samei *et al.* (Refs. 4, 5, and 14–17), and the IEC (Ref. 2), respectively. Method B has historical and current versions differing by the number of ROIs used. The beam spectrum for method C was set at a 70 kV nominally, with kilovoltage adjusted to give a HVL of 7.1 mm Al according to the IEC procedure for the RQA5 beam quality. ROIs were either in overlapping (OL) or nonoverlapping (NOL) patterns. For detrending, method A used a 2-D first-order fit to the data within a ROI, while methods B and C used a 2-D second-order polynomial fit to ROI data. Data rows averaged indicate how many adjacent rows of data in the two-dimensional NPS were averaged to give the one-dimensional NPS plot. Method B included the data along the axis in the two-dimensional NPS, whereas methods A and C excluded the on-axis data. Methods A and B used no external beam apertures, but method C included IEC-specified external beam apertures.

Method	kV	Filtration	# ROIs	ROI size	Detrending	Data rows averaged
Method A	70	0.5 mm Cu	64 NOL	128 × 128	2-D (first order)	8 (w/o axis)
Method B (historical)	70	19 mm Al	100 NOL	128 × 128	2-D (second order)	15 (w/ axis)
Method B (current)	70	19 mm Al	343 OL	128 × 128	2-D (second order)	15 (w/ axis)
Method C	74	21 mm Al	160 OL	256 × 256	2-D (second order)	14 (w/o axis)

detrending, and methods of extracting one-dimensional (1-D) NPS data from the 2-D NPS]. Table I lists the standard acquisition and processing parameters associated with these three methods. In addition to comparing the three methods directly, a number of subcomparisons were performed to elucidate the influence of the various parameter choices associated with NPS methodology. Table II lists the combinations of parameters for image acquisition and analysis for each of the sub-comparison evaluations performed. In the following

sections we describe the details of the imaging system, beam conditions, image acquisition, and the NPS processing employed in this study.

A. Imaging system

A commercial-grade α :Si/CsI flat-panel radiographic detector (equivalent to that in the Revolution XQ/i system, GE Healthcare, Milwaukee, WI) was used for all measurements.

TABLE II. Acquisition and processing parameters for each measurement condition evaluated. Beam spectra: Method A (70 kV, 0.5 mm Cu), method B (70 kV, 19 mm Al), and method C (IEC RQA5, 74 kV, 21 mm Al).

Beam spectrum	Analysis method	Apertures	No. images	No. indep. image pixels	Analysis area	ROI size	Overlapping vs nonoverlapping
C	C	External (per IEC)	1	409 600	640 × 640	256	OL
			3	1 228 800			
			10	4 096 000			
C	C	External (per IEC)	1	262 144	512 × 512	256	NOL
			3	786 432			
			10	2 621 440			
C	C	None	3	1 228 800	640 × 640	256	OL
			10	4 096 000			
C	A	External (per IEC)	10	4 096 000	640 × 640	128	NOL
C	B (Historical)	External (per IEC)	10	4 096 000	640 × 640	128	NOL
C	B (Current)	External (per IEC)	3	1 228 800	640 × 640	128	OL
A	A	None	1	1 048 576	1024 × 1024	128	NOL
A	C	None	3	1 228 800	640 × 640	256	OL
B	B (Historical)	None	1	1 638 400 ^a	1280 × 1280 ^a	128	NOL
B	B (Current)	None	1	1 638 400 ^a	1280 × 1280 ^a	128	OL
B	C	None	3	1 228 800	640 × 640	256	OL

^aPreviously published historical analysis areas were 1664 × 1664 (2 768 896 pixels) NOL and 1728 × 1728 (2,985,984 pixels) OL; current evaluation area was modified due to limited field of view as a result of the ionization detector placement.

The detector, with a 0.2 mm pixel pitch and a 41×41 cm 2 overall field of view, was mounted in a prototype research radiographic system and was coupled to a standard x-ray tube and generator. The antiscatter grid, system faceplate, and automatic exposure control sensors were removed for all measurements, in keeping with the IEC standard. The details of the detector calibration performed prior to acquisition of imaging data are outlined in a concurrent paper.²¹ As the intent of this paper was not to characterize the NPS performance of a specific device *per se*, but rather to identify the way in which three NPS measurement methods compare, the choice of detector used for these measurements was not critical. However, in order to make this intercomparison of methods as generalizable as possible, the imaging system used was selected as representative of contemporary digital radiographic systems.

B. Beam conditions

The three NPS methods compared in this paper all used roughly comparable beam spectra (70 kV nominal with added filtration). Method A used 70 kV with 0.5 mm Cu filtration; method B used 70 kV with 19 mm Al filtration; and method C used 74 kV (70 kV nominal) with 21 mm Al filtration. Spectra for each method matched those reported in previous publications. Method C (the IEC method) specified an initial Al filtration and a given half-value layer (HVL) rather than a specific tube kilovoltage. The kilovoltage for method C was thus adjusted to 74 kV to achieve an IEC-specified HVL of 7.1 mm Al with a 21 mm added Al filter. Measured HVLs of the 70 kV beams for methods A and B were 6.7 and 6.6 mm Al, respectively. Further details of the beam conditions are provided in a concurrent paper.²¹

C. System response function

System response functions were measured for the spectra of methods A, B, and C to verify detector linearity and to determine the exposure associated with each NPS estimate. The method of measuring response curves is described in detail in a companion paper.²¹ Briefly, response curves were generated by acquiring flat-field images for each of the three spectra over a range of mAs settings. Mean pixel values were determined in a 100×100 pixel region near the center of each image. Exposure values were measured with a narrow-beam geometry using a calibrated ion chamber (MDH Model 1015, 10X5-6 ionization chamber, Radcal, Monrovia, CA) placed 90.5 cm from the focal spot with the detector moved vertically out of the beam field of view (i.e., exposure measured free in air with no backscatter from the detector). Exposure values at the plane of the detector were then computed by using the inverse square law. For each beam quality, a linear fit to the mean pixel value versus exposure was used to estimate exposure in the flat-field images used for the NPS estimation.

D. Image acquisition

For all measurements, flat-field images were acquired with nothing in the beam but the required filtration (and IEC-specified apertures, where indicated). The filtration was placed on the exit side of the collimator. The focal spot to detector distance was 184.5 cm. Method C measurements were made with apertures, in keeping with the IEC standard (illustrated in Fig. 1 of a concurrent paper²¹) and without apertures for comparison purposes. For Methods A and B, no apertures were used, but the beam was collimated to just beyond the edge of the detector panel.

Images were acquired for the different spectra at various levels of incident exposure. The IEC standard specifies that exposures of approximately $E_{nl}/3.2$, E_{nl} , and $3.2E_{nl}$ be used, where E_{nl} is the “normal level” exposure for a particular imaging application for a given device. In consultation with the manufacturer of the flat-panel device, a value E_{nl} of approximately 0.4 mR (3.5 μ Gy) was used. Three images were acquired for the beam spectra of methods A and B and ten images for method C (based on the IEC requirement to use 4 000 000 independent measurement pixels).

To minimize detector lag effects, a minimum interval of 2 min was employed between image acquisitions in a progression from low to high exposures and from open field of view to a restricted field of view. A minimum interval of 10 min was used between aperture configurations. All NPS data acquisitions were completed within 24 h of the detector calibration.

E. NPS processing

The flat-field image data were processed using the NPS processing methods specified by methods A, B, and C. The methods differed in terms of various parametric choices and algorithmic implementations. Among those, the number, size, and overlapping of the ROIs varied by measurement method (Table II). Method A used ROIs of size 128×128 pixels; 64 such nonoverlapping ROIs were used in a 1024×1024 region near the center of the image, in keeping with the previously published results with this method. Two configurations were used for method B: the B-historical method used nonoverlapping 128×128 ROIs and the B-current method used overlapping ROIs of the same size, reflecting a modification of method B over time. (Historically, method B used a total area of 1664×1664 pixels for analysis, but in these experiments the total area of analysis was restricted to 1280×1280 due to the placement of the ion chamber). For method C, ROIs of size 256×256 were used in a 640×640 pixel region near the center of each image; the ROIs were arranged in four different overlapping patterns, each pattern offset by one-half the ROI size in each dimension, in keeping with the IEC standard, giving a total of 16 overlapped ROIs per image. In this arrangement, 16% of pixels appeared in only one ROI, 48% appeared in two ROIs, and 36% appeared in four ROIs. Other combinations of ROI size and overlapped/nonoverlapped orientation were used for certain specific data analyses in order to elucidate effects due to the ROI size and the number of ROIs.

The methods also differed in terms of detrending techniques. Each method used a detrending technique to correct for possible background gradients in individual ROIs. For method A, a two-dimensional first-order fit (i.e., planar ramp) was subtracted from the data prior to NPS analysis. It should be noted that because method A excludes data on the u and v axes when generating the one-dimensional NPS plots, this subtraction does not change the measured one-dimensional curves, as a ramp subtraction only affects the data on the frequency axes. Method B employed a quadratic (2-D second-order polynomial) surface fit to the data in each ROI and then subtracted that surface prior to NPS analysis. For method C, the same NPS detrending technique used for method B was also employed, satisfying all requirements of the IEC standard.

In addition to detrending individual ROIs, the methods also included the means to correct for small regional variation in exposure from ROI to ROI. Such regional variations are often caused by the heel and inverse square law effects across the detector's field of view. Correcting for these variations provides an estimate of NPS that is less biased by such regional exposure variations. For all three methods, the correction involved normalizing the pixel values in each ROI by a function of the ROI mean relative to some reference mean. Method A normalized the pixel values in each ROI by the ratio of the square root of the ROI mean to the global mean. Methods B and C normalized pixel values in each ROI by the ratio of ROI mean to the mean of a reference ROI (located in the upper left corner of the image). The effect of the normalization procedure was determined by comparing NPS estimates with both of these approaches to normalization.

The NPS is often used as an input to the computation of detective quantum efficiency (DQE). In the DQE computation, it is necessary to correct for the gain of the system, and the NPS (given in units of digital value squared times mm²) is divided by the square of the mean value of the pixels used for analysis (in units of digital value). This ratio is referred to as the normalized noise power spectrum (NNPS), and has units of mm²:

$$\text{NNPS}(u,v) = \frac{\text{NPS}(u,v)}{(\text{large area signal})^2}. \quad (2)$$

This ratio assumes that the pixel values have been linearized with respect to exposure. Because the NNPS has been historically reported in earlier work by Dobbins *et al.* and Samei *et al.*, it was used as the basis of the results reported in this paper. It should be noted that in the literature, the terms "NPS" and "NNPS" are often used interchangeably to refer to the normalized noise power spectrum.

The Fourier transform used for method A was a FFT adapted from the method of Bracewell,²³ and hand-coded by the author. The FFT used for the data analysis with methods B and C was hand coded and adapted from the work of Brigham.²⁴ For method A, 4 lines of data just above and 4 lines just below the u -axis in the 128 × 128 two-dimensional NPS space were used to generate the one-dimensional NPS curves, with the on-axis data excluded. For each datum in

this 8-row set, the radial frequency given by $\sqrt{(u^2+v^2)}$ was used; all data in this 8-row set were then averaged into bins of interval 0.05 mm⁻¹. The result was an approximation of the one-dimensional NPS along the direction of the u axis from a band through the two-dimensional NPS space. For method B, data were similarly processed, but a total of 15 rows (7 rows above and 7 below, *including* the on-axis row) was used to determine an approximation of the one-dimensional NPS along the direction of the u axis. Method C used a total of 14 rows (7 rows above and 7 below, *excluding* the on-axis row). For methods B and C, data were also averaged into bins of interval 0.05 mm⁻¹. A subsequent analysis of data along the v axis for one measurement condition found essentially no difference between the u - and v -axis directions; therefore, only the u -axis data were processed for the remaining measurements.

IV. RESULTS

Results are described in this section for each subcomparison performed as well as for an overall comparison of methods A, B, and C.

A. Precision of NPS estimate

The NPS defined in Eq. (1) is an ensemble average over an infinite number of noise realizations; for a finite number of noise realizations, there will be an uncertainty associated with the NPS estimate. The standard deviation of an NPS estimate is proportional to the NPS; therefore, the relative uncertainty (i.e., the coefficient of variation) of NPS estimates is independent of frequency. This uncertainty has been shown by Wagner and Sandrik²⁵ to vary as $1/\sqrt{N}$, where N is the number of independent frequency bin measurements associated with a given NPS value. As a validation of the predicted uncertainty values, we measured the relative uncertainty in NNPS using the method A processing technique with 25,128 × 128 nonoverlapping ROIs and 8 rows of data averaged, and found it to be $6.48\% \pm 0.25\%$; this value agreed well with the value of 6.25% predicted by Wagner and Sandrik.

In the case of overlapping ROIs, the uncertainty in the ensemble average does not decrease as the square root of the number of ROIs, because the overlapping ROIs do not contain statistically independent data. To determine the relative uncertainty between overlapping and nonoverlapping ROIs, we measured the relative uncertainty using the method C processing technique with 256 × 256 ROIs and 14 rows of data averaged in configurations of 4 nonoverlapping or 16 overlapping ROIs per image. When no Hamming window was used, the relative uncertainty, averaged over all frequencies, in the overlapping ROI case relative to the nonoverlapping ROI case had a ratio of 0.80, which is equal to the square root of the reciprocal number of independent pixels in the two cases. When the Hamming window was used, the relative uncertainty in both the overlapping and nonoverlapping ROI cases was worse, although the uncertainty in the overlapping case relative to the nonoverlapping case differed by a greater amount (a ratio of 0.54). This larger difference

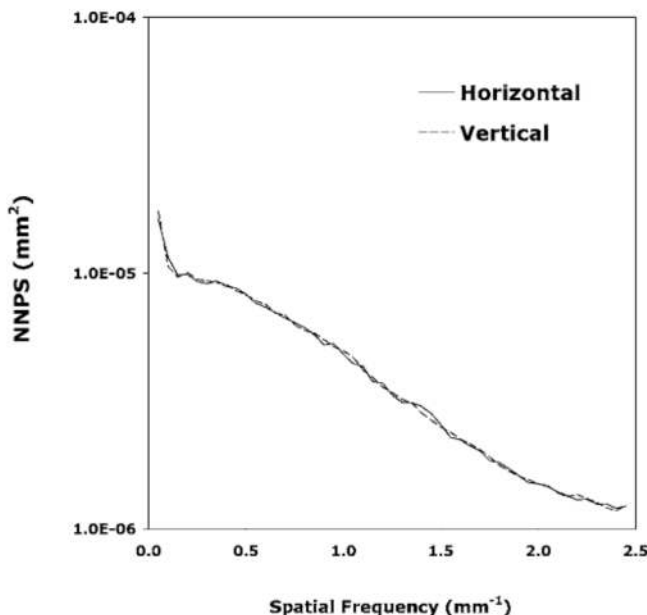


FIG. 1. NNPS directional dependence. Method C spectrum (IEC RQA5, 74 kV, 21 mm Al filtration) with apertures. Incident exposure was 0.53 mR. Ten images used for analysis with 160 total overlapping ROIs of size 256×256 , using the method C analysis procedure. Error bars: $\pm 2.3\%$.

between overlapping and nonoverlapping ROIs with the Hamming window is likely due to the better statistical independence of values in the overlapping ROIs resulting from nonuniform pixel weighting introduced by the Hamming window.

The factors relating to overlapping ROIs and a Hamming window were used to adjust the relative uncertainty predicted by the method of Wagner and Sandrik for all subsequent data reported below.

B. Directional dependence

Figure 1 depicts the directional dependence of the measured NNPS in the horizontal and vertical directions for one of the measurement conditions. The method C (IEC) spectrum with apertures was used, at an incident exposure of 0.53 mR. The average NNPS estimate from ten images was computed using method C data analysis procedures, with overlapping ROIs of size 256×256 . The two curves were virtually identical (0.3% relative difference between curves, averaged over all frequencies; estimated standard error of average: $\pm 0.5\%$) with no discernable trend of the difference between curves, and hence only horizontal data are reported for the remainder of the graphs.

C. Impact of beam quality

The effect of beam spectrum is shown in Fig. 2 for the spectra of methods A–C (without apertures). Because the mean exposure in each case is slightly different, the product of exposure and normalized noise power (E^*NNPS) is plotted in order to produce a quantity that in the absence of additive noise is independent of incident exposure, and there-

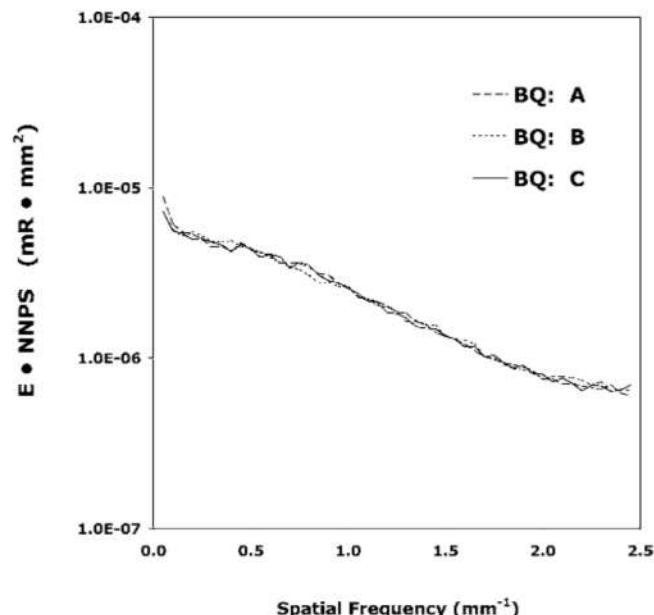


FIG. 2. NNPS dependence on beam spectrum. Plotted is incident exposure times NNPS for method A spectrum (70 kV, 0.5 mm Cu filtration), method B spectrum (70 kV, 19 mm Al filtration), and method C spectrum (IEC RQA5, 74 kV, 21 mm Al filtration), all without apertures. Incident exposures were 0.49 mR (A), 0.40 mR (B), and 0.43 mR (C, no apertures). Three images used for analysis with 48 total overlapping ROIs of size 256×256 , using method C (IEC) analysis procedure. Error bars: $\pm 4.2\%$. BQ=beam quality.

fore, more easily compared across spectra.¹⁰ The incident exposures (E) were 0.49, 0.40, and 0.43 mR for the spectra of methods A, B, and C (without apertures), respectively. The average NNPS estimate from three images was computed for each case, using the method C data analysis procedure and overlapping ROIs of size 256×256 . The E^*NNPS data demonstrated very little dependence on the spectrum ($\leq 0.9\%$ relative difference between curves, averaged over all frequencies; estimated standard error of average: $\pm 0.8\%$).

D. Impact of beam limitation

The impact of including the IEC-required apertures in the method C measurement procedure is demonstrated in Fig. 3. The method C spectrum and analysis technique were used in both cases. The product of exposure and normalized noise power is plotted. Incident exposures were 0.53 and 0.56 mR for the images with and without apertures, respectively. The average NNPS estimate from ten images was computed for each case, using overlapping ROIs of size 256×256 . Little difference was noted between the E^*NNPS measured with and without apertures (2.3% relative difference between curves, averaged over all frequencies; estimated standard error of average: $\pm 0.5\%$).

E. Impact of analysis method

The effect of the noise power analysis method, independent of spectrum, is shown in Fig. 4. The same beam condition was used for all curves (method C spectrum, with aper-

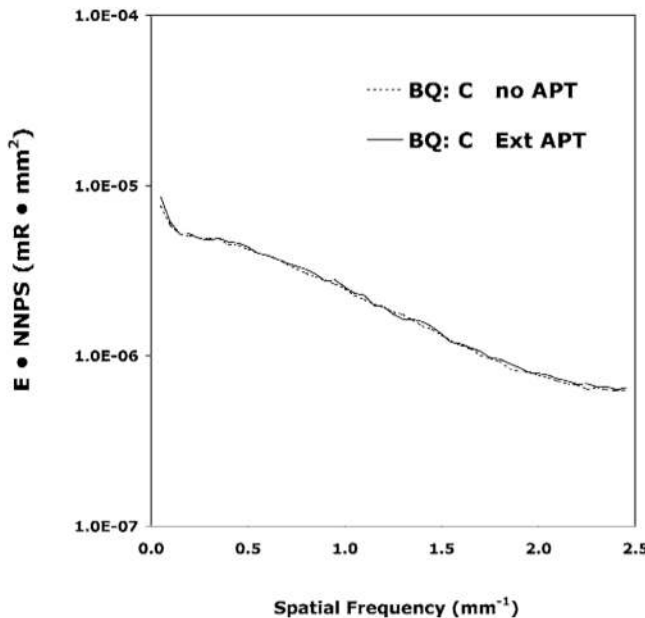


FIG. 3. NNPS dependence on IEC-specified apertures with method C (IEC) spectrum. Incident exposures were 0.53 mR (with apertures—Ext APT) and 0.56 mR (without apertures—no APT). Ten images used for an analysis with 160 total overlapping ROIs of size 256×256 , using method C analysis procedure. Error bars: $\pm 2.3\%$. BQ=beam quality.

tures), but with four different methods of analysis, as specified by methods A, B-historical, B-current, and C. A different number of images was used for the four methods in order to maintain approximately equivalent statistics (ten images for methods A and B-historical; three images for meth-

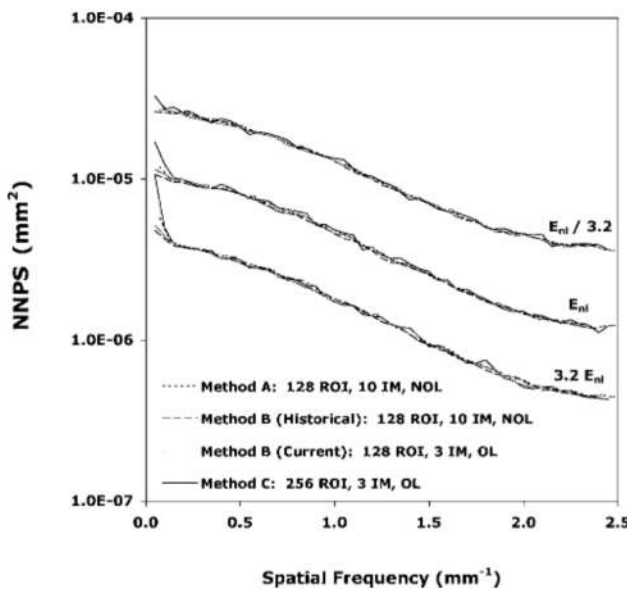


FIG. 4. NNPS dependence on analysis method. “Normal level” exposure (E_{nl}) is approximately 0.4 mR. Method C spectrum with apertures. ROIs used were 250 total nonoverlapping (NOL) ROIs of size 128×128 (A), 250 total nonoverlapping ROIs of size 128×128 (B-historical), 219 total overlapping (OL) ROIs of size 128×128 (B-current), and 48 total overlapping ROIs of size 256×256 (C). IM indicates the number of images used. Error bars: $<\pm 4.2\%$.

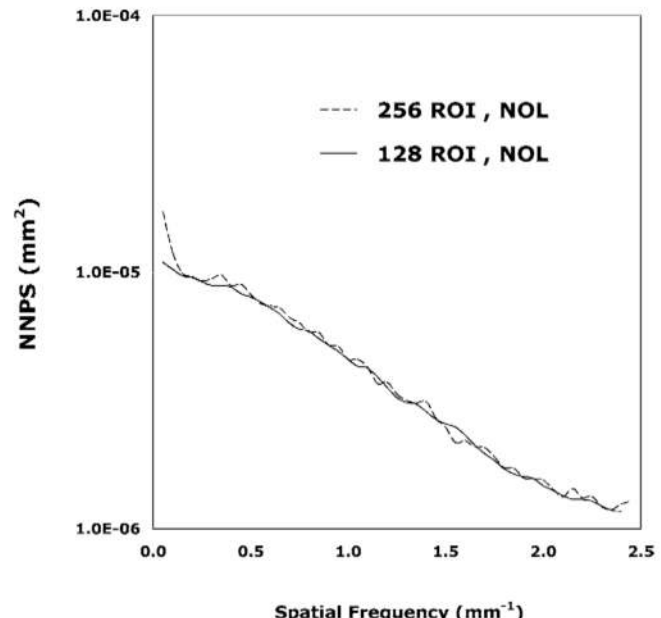


FIG. 5. NNPS dependence on ROI size using the method C spectrum with apertures. Ten images used for analysis. ROIs used were 160 total nonoverlapping (NOL) ROIs of size 128×128 and 40 total nonoverlapping ROIs of size 256×256 , both using the method C analysis procedure. Error bars: $<\pm 4.3\%$.

ods B-current and C). The average NNPS estimate from these images was computed in each case. The ROI sizes for the four methods were 128×128 nonoverlapped ROIs for methods A and B-historical, 128×128 overlapped ROIs for method B-current, and 256×256 overlapped ROIs for method C. Data are shown for the three exposure levels specified by the IEC (method C). There was only a small difference in the NNPS estimates produced by the four analysis methods for frequencies $>0.15 \text{ mm}^{-1}$. For example, at the middle exposure there was a $\leq 3.1\%$ relative difference between curves, averaged over all frequencies above 0.15 mm^{-1} (estimated standard error of average $<\pm 0.8\%$). The differences were slightly lower when comparing only between methods A and B ($\leq 1.2\%$ average relative difference between curves, averaged over all frequencies above 0.15 mm^{-1}).

F. Impact of ROI size

Figure 5 shows the dependence of the NNPS on the ROI size used for analysis. Nonoverlapping ROIs of size 128×128 and 256×256 were used, with data taken from a 512×512 region near the center of the image in both cases. The method C spectrum (IEC RQA5, 74 kV, 21 mm Al) with apertures and Method C analysis technique were used. Fourteen rows of data in the two-dimensional NNPS were averaged (excluding the axis) for both the 128×128 and 256×256 size ROIs. Ten images were used for an analysis of both ROI sizes, and the NNPS results from the ten images averaged. For the smoothly varying NNPS curves obtained in these experiments, there was very little difference in the NNPS estimate with either ROI size (1.8% relative differ-

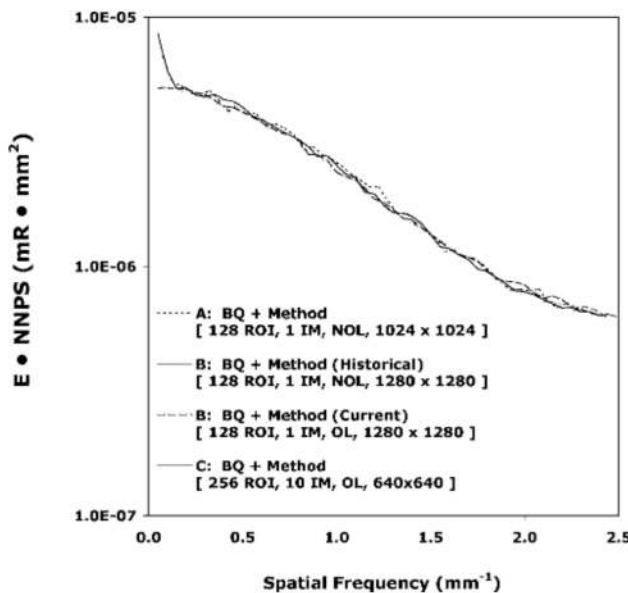


FIG. 6. Overall comparison of NNPS methods. Plotted is the incident exposure times NNPS for the method A spectrum (70 kV, 0.5 mm Cu filtration), method B spectrum (70 kV, 19 mm Al filtration), and the method C spectrum (IEC RQA5, 74 kV, 21 mm Al, with apertures). Incident exposures were 0.49 mR (A), 0.40 mR (B), and 0.53 mR (C, with apertures). ROIs used were 64 nonoverlapping ROIs of size 128×128 (A), 100 nonoverlapping ROIs of size 128×128 (B-historical), 343 overlapping ROIs of size 128×128 (B-current), and 160 total overlapping ROIs of size 256×256 (C). IM indicates the number of images used for analysis. BQ=beam quality. Error bars: $\leq \pm 3.9\%$.

ence between curves, averaged over all frequencies; estimated standard error of average $<\pm 0.9\%$). In this particular case, the larger ROI size demonstrated worse precision of measurement; however, if the number of data rows analyzed were adjusted for ROI size, such that comparable areas in the two-dimensional NNPS were used for analysis, then the identical precision of measurement would be found for both ROI sizes.

G. Overall comparison of methods

Figure 6 shows the final overall comparison of methods A, B, and C, including all components of the differences between the methods (each used its own historical ROI size, spectrum, number of acquired images, and analysis method). The exposure conditions used were 70 kV with 0.5 mm Cu (no apertures) for method A; 70 kV with 19 mm Al (no apertures) for method B; and 74 kV with 21 mm Al (with apertures) for method C. ROI conditions were the following: 1 image using 64 nonoverlapping ROIs of size 128×128 for method A; 1 image using 100 nonoverlapping ROIs of size 128×128 for method B-historical; 1 image using 343 overlapping ROIs of size 128×128 for method B-current; and 10 images using 160 overlapping 256×256 ROIs (16 per image) for method C. The data is plotted in terms of the product of exposure and NNPS in order to account for the impact of minor differences in incident exposure in each case. There were very small differences between the four curves above

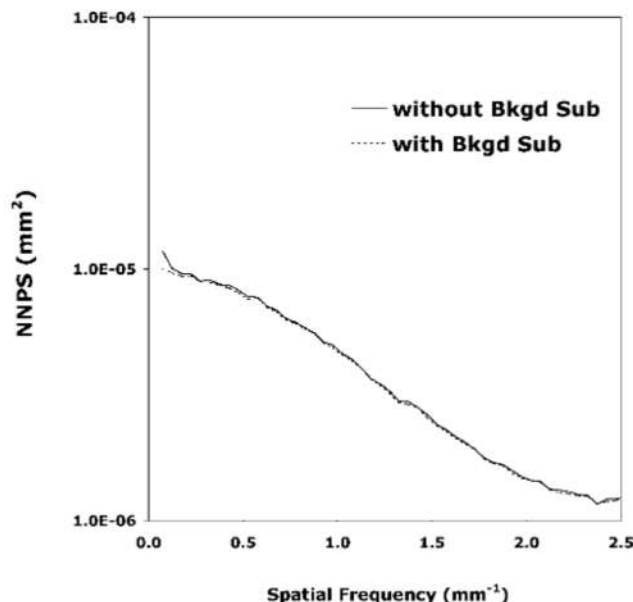


FIG. 7. Impact of background subtraction on the NNPS. Method C spectrum (IEC RQA5 74 kV, 21 mm Al filtration) with apertures at an incident exposure of 0.53 mR. Ten images were used for the analysis with 250 total nonoverlapping ROIs of size 128×128 , using the method A analysis procedure. A fixed background was determined as the mean of the ten images, subsequently subtracted from original images. The NNPS was computed with and without background subtraction.

0.15 mm^{-1} ($\leq 1.6\%$ relative difference between curves, averaged over all frequencies above 0.15 mm^{-1} ; estimated standard error of average $<\pm 0.8\%$).

H. Influence of fixed pattern noise

All of the NNPS data depicted above include the effects of fixed patterns in the images in addition to the stochastic components from the x-ray flux and electronic noise. The fixed patterns that are stochastic (such as from random spatial variation in the detector response) should be included in the total NPS. However, as indicated earlier, a flat image may contain fixed patterns that are artifactual and not stochastic. In order to gain an appreciation for the amplitude of the fixed pattern components in the NPS estimates, an average of 10 flat-field images was performed and subtracted from each image to yield a set of images with the suppression of spatially fixed patterns common to all. Figure 7 demonstrates the relationship between the subtracted and the unsubtracted NNPS estimates using method A on the IEC beam spectrum (with apertures). It can be seen that the subtracted and unsubtracted NNPS estimates are virtually identical above about 0.15 mm^{-1} , indicating that the detector pixel-to-pixel gain correction adequately eliminates fixed pattern noise and any systematic effect in the NNPS estimate from nonstochastic patterns is only important at the very lowest spatial frequencies. This finding does not speak directly to the comparisons of the three NNPS methods, but demonstrates an important way of distinguishing systematic effects in the reported NNPS measurements.

I. Impact of normalization technique

As noted earlier, an additional detail of evaluation relates to the technique used to correct for small variations in regional exposure. In method A, the mean of each ROI was measured and used to adjust the pixel values of each ROI by the square root of the ROI mean; this permitted a normalization of the NPS across ROIs for slight variations in regional exposure (such as from the heel effect). Methods B and C corrected the data in each ROI by the ROI mean, rather than the square root of the mean, with the intent of accomplishing the same goal. An evaluation of the difference due to the two normalization procedures was conducted on one image acquired with the method C spectrum at 0.53 mR. Method A analysis was performed using 25 nonoverlapping ROIs of size 128×128 . The maximum difference between NNPS values at any given frequency for the two normalization methods was 0.02%. Therefore, it was concluded that differences in the method of normalization had a negligible effect on the measured NNPS.

V. DISCUSSION

Overall, the NNPS estimates were comparable to previously obtained results^{7,16} using the same detector. The NNPS curves demonstrated a very small additive noise component (manifested as a white noise pedestal) with a component associated with a MTF² smoothly varying above about 0.15 mm^{-1} . The subtraction of the mean of ten images revealed that the systematic rise in the NNPS estimate for frequencies below $<0.15 \text{ mm}^{-1}$ was likely due to fixed pattern features in the images uncorrected by the detector's pixel-by-pixel gain correction. For nonsubtraction methods, this low-frequency rise is typical of the NNPS curves reported in the literature.^{3,7} The low-frequency rise was less with method B processing methods; these used a second-order detrending that suppressed the low-frequency rise in comparison to method A (which used first-order detrending) or method C (which also used a second-order polynomial fit but larger ROIs, and hence, worse detrending).

All of the various acquisition and processing factors evaluated were found to have relatively little influence on the measured NNPS. The beam spectrum, the use of the IEC apertures, the method of ROI normalization for regional exposure variation, and the ROI size all had $\leq 2.3\%$ effect on the measured NNPS estimates, on average, across frequency. A factor that influenced the NNPS estimates in a slightly greater way, though still small, was the NPS analysis routine used. There was $\leq 3.1\%$ difference on average, across frequency, between the three analysis routines. This difference was likely due to differences in ROI size and the width of the band of data in the two-dimensional NNPS averaged to yield the 1-D NNPS.

A factor that greatly influenced the very lowest spatial frequencies was the choice of detrending method used to correct for residual artifacts in the ROIs. It should be noted that while detrending introduces an element of arbitrariness to the determination of the NPS response, it does reduce the presence of low-frequency nonstochastic artifacts. The

second-order polynomial fit used by method B (in conjunction with 128×128 ROIs) provided the best elimination of low-frequency artifacts. However, it is important to assess the prevalence of low-frequency artifacts for a given system, so it is recommended that a second analysis of the data be performed using a mean-image subtraction method on non-detrended data. By comparing the low-frequency NPS values with and without mean-image subtraction, one can ascertain the magnitude of any low-frequency artifacts.

All of the measured average relative differences between curves were found to be greater than the standard errors of the average, except for the differences due to directional dependence and method of regional exposure normalization. Thus, while most of the comparisons yielded differences that are likely statistically significant, for practical purposes, the absolute magnitude of differences was so small that the various methods can be considered roughly equivalent.

Methods A and B (including spectrum and analysis) agreed very well overall, differing by only $\leq 0.8\%$ on average for frequencies above 0.15 mm^{-1} . The greatest difference between the two methods was at the very lowest frequencies, likely due to the difference in detrending methods. Thus, when comparing historical NPS data acquired and analyzed by these two methods, one would expect less than 1% error in the NNPS due to the method used.

Method C (including spectrum and analysis) agreed well with both methods A and B (0.9% difference, on average, between methods A and C above 0.15 mm^{-1} and $\leq 1.6\%$ difference, on average, between methods B and C above 0.15 mm^{-1}). Approximately the same trends were noted at the three exposure levels measured ($E_{nl}/3.2$, E_{nl} , and $3.2E_{nl}$). A factor of importance when making method C (IEC) measurements is that the high-purity Al filtration specified by the IEC ($\geq 99.9\%$) has been associated with low-frequency artifacts, and thus we recommend the use of type 1100 Al (99.0% purity).²⁶

While the current results indicate excellent agreement between the three methods evaluated, it should be noted that only a single detector was used for the comparative study. It is possible that other detectors would show a different relative performance from the three techniques. It is likely, though, that any differences in measured NNPS due to differences in the detector would be mostly due to the choice of beam spectrum and use of external apertures; other differences between methods are likely to have comparable magnitudes as those reported here. The quantitative use of the comparative findings need to be taken with additional precautions, as noted in the last paragraph of the Discussion in a concurrent paper.²¹

VI. CONCLUSIONS

In summary, excellent agreement was found in NPS estimates obtained using methods A, B and C; historical comparisons between data reported on similar detectors using the three methods can be made with an overall disagreement of no more than about 1.6%. This finding suggests that any of the three methods, including the new IEC standard (method

C), can be used with confidence. We do, however, offer several recommendations based primarily on matters of practicality of the measurement procedures.

(1) The beam spectrum specified by IEC provides the most reliably calibrated spectrum. However, there was virtually no difference between the results measured with the three spectra reported here. As the IEC-specified spectrum is based on a measured HVL rather than a kilovoltage and filtration thickness, it is the least convenient to use because it requires a measurement to confirm target HVL.

(2) A ROI size of 128×128 coupled with background detrending using a second-order polynomial fit yields the least susceptibility to residual shading artifacts at very low frequencies. Because the frequencies affected by residual shading are less than the lowest frequency specified by the IEC, one may ignore the detrending and use a ROI size of 256×256 for purposes of measurement according to the IEC standard. For investigators interested in the noise performance at frequencies lower than those specified by the IEC, ROIs of size 128×128 and second-order polynomial fit background detrending are recommended.

(3) The use of a subtraction method is recommended to further elucidate the degree of low-frequency residual artifacts.

(4) Frequency bins of 0.05 mm^{-1} , used by all three methods, give adequate resolution of the spectrum while providing reasonably smooth results.

(5) Overlapping of ROIs using the method specified by the IEC returned minimal benefit in improved precision of the NNPS estimate; the small improvement in measurement uncertainty was due to the slightly larger image area (hence, a slightly larger number of independent pixels) that could be placed within the collimated region of the beam when using overlapping ROIs of large size.

(6) Provided a constant number of independent image pixels is used for NPS analysis, the use of the IEC-specified beam-limiting apertures had little impact on the NPS estimate. Their use, however, severely limits the field of view, increases the number of images needed for a reasonably smooth NPS estimate, and complicates the image acquisition process. Their use, therefore, is not recommended.

ACKNOWLEDGMENTS

The authors wish to thank Dr. Carl Ravin of the Duke Radiology Department for his assistance with this study. The flat-panel detector used for evaluation in this study was provided through a research agreement with GE Healthcare. This work was supported in part by grants from the National Institutes of Health (R01 CA80490 and R01 CA109074).

¹⁾This paper is part of a two-paper series. The readers are advised to also review the concurrent manuscript (Ref. 21).

¹A. D. A. Maidment, M. Albert, P. C. Bunch, I. A. Cunningham, J. T. Dobbins III, R. M. Gagne, R. M. Nishikawa, R. F. Wagner, and R. L. Van Metter, "Standardization of NPS measurement: Interim report of AAPM TG16," Proc. SPIE **5030**, 523–532 (2003).

²⁾"Medical electrical equipment—characteristics of digital x-ray imaging devices—part 1: determination of the detective quantum efficiency," International Electrotechnical Commission, Geneva, Switzerland, 2003.

³J. T. Dobbins III, D. L. Ergun, L. Rutz, D. A. Hinshaw, H. Blume, and D. C. Clark, "DQE(f) of four generations of computed radiography acquisition devices," Med. Phys. **22**, 1581–1593 (1995).

⁴E. Samei and M. J. Flynn, "Physical measures of image quality in photostimulable phosphor radiographic systems," Proc. SPIE **3032**, 328–338 (1997).

⁵E. Samei, R. S. Saunders, J. Y. Lo, J. T. Dobbins III, J. L. Jesneck, C. E. Floyd, Jr., and C. E. Ravin, "Fundamental imaging characteristics of a slot-scan digital chest radiographic system," Med. Phys. **31**, 2687–2698 (2004).

⁶C. D. Bradford, W. W. Peppler, and J. T. Dobbins III, "Performance characteristics of a Kodak computed radiography system," Med. Phys. **26**, 27–37 (1999).

⁷C. E. Floyd, Jr., R. J. Warp, J. T. Dobbins III, H. G. Chotas, A. H. Baydush, R. Vargas-Voracek, and C. E. Ravin, "Imaging characteristics of an amorphous silicon, flat-panel detector for digital chest radiography," Radiology **218**, 683–688 (2001).

⁸P. R. Granfors and R. Aufrichtig, "Performance of a $41 \times 41\text{-cm}^2$ amorphous silicon flat panel x-ray detector for radiographic imaging applications," Med. Phys. **27**, 1324–1331 (2000).

⁹W. Hillen, U. Schiebel, and T. Zaengel, "Imaging performance of a digital storage phosphor system," Med. Phys. **14**, 744–751 (1987).

¹⁰M. J. Flynn and E. Samei, "Experimental comparison of noise and resolution for 2k and 4k storage phosphor radiography systems," Med. Phys. **26**, 1612–1623 (1999).

¹¹W. Zhao, W. G. Ji, A. Debrue, and J. A. Rowlands, "Imaging performance of amorphous selenium based flat-panel detectors for digital mammography: characterization of a small area prototype detector," Med. Phys. **30**, 254–263 (2003).

¹²J. H. Siewerdsen, L. E. Antonuk, Y. El-Mohri, J. Yorkston, and W. Huang, "Signal, noise power spectrum, and detective quantum efficiency of indirect-detection flat-panel imagers for diagnostic radiology," Med. Phys. **25**, 614–628 (1998).

¹³U. Neitzel, I. Maack, and S. Gunther-Kohfahl, "Image quality of a digital chest radiography system based on a selenium detector," Med. Phys. **21**, 509–516 (1994).

¹⁴E. Samei, "Image quality in two phosphor-based flat panel digital radiographic detectors," Med. Phys. **30**, 1747–1757 (2003).

¹⁵E. Samei and M. J. Flynn, "An experimental comparison of detector performance for computed radiography systems," Med. Phys. **29**, 447–459 (2002).

¹⁶E. Samei and M. J. Flynn, "An experimental comparison of detector performance for direct and indirect digital radiography systems," Med. Phys. **30**, 608–622 (2003).

¹⁷E. Samei, M. J. Flynn, H. G. Chotas, and J. T. Dobbins III, "DQE of direct and indirect digital radiography systems," Proc. SPIE **4320**, 189–197 (2001).

¹⁸K. A. Fetterly and N. J. Hangiandreou, "Effects of x-ray spectra on the DQE of a computed radiography system," Med. Phys. **28**, 241–249 (2001).

¹⁹S. M. Kengyelics, A. G. Davies, and A. R. Cowen, "A comparison of the physical imaging properties of Fuji ST-V, ST-VA, and ST-VN computed radiography image plates," Med. Phys. **25**, 2163–2169 (1998).

²⁰J. T. Dobbins III, "Image quality metrics for digital systems," in *Handbook of Medical Imaging*, edited by R. L. van Metter, J. Beutel, and H. Kundel (Society of Photo-Optical Instrument Engineers, Bellingham, WA, 2000), Vol. 1, p. 161–222.

²¹E. Samei, J. T. Dobbins III, N. T. Ranger, and Y. Chen, "Inter-comparison of methods for image quality characterization: 1. modulation transfer function," Med. Phys. **33**, 1454–1465 (2006), preceding paper.

²²J. C. Dainty and R. Shaw, *Image Science* (Academic, London, 1974).

²³R. N. Bracewell, *The Fourier Transform and its Applications* (McGraw-Hill, New York, 1978).

²⁴E. O. Brigham, *The Fast Fourier Transform* (Prentice-Hall, Englewood Cliffs, NJ, 1974).

²⁵R. F. Wagner and J. M. Sandrik, "An introduction to digital noise analysis," in *The Physics of Medical Imaging: Recording System Measurements and Techniques*, edited by A. G. Haus (American Association of Physicists in Medicine, New York, 1979), pp. 524–545.

²⁶N. T. Ranger, E. Samei, J. T. Dobbins III, and C. E. Ravin, "Measurement of the detective quantum efficiency in digital detectors consistent with the IEC 62202-1 standard: practical considerations regarding the choice of filter material," Med. Phys. **32**, 2305–2311 (2005).

Note: This copy is for your personal, non-commercial use only. To order presentation-ready copies for distribution to your colleagues or clients, use the *Radiology Reprints* form at the end of this article.

Assessment of Detective Quantum Efficiency: Intercomparison of a Recently Introduced International Standard with Prior Methods¹

Nicole T. Ranger, MSc
Ehsan Samei, PhD
James T. Dobbins III, PhD
Carl E. Ravin, MD

Purpose:

To prospectively evaluate the recently introduced international standard method for measurement of the detective quantum efficiency (DQE) of digital radiography systems, in comparison with representative prior methods.

Materials and Methods:

A recently introduced international standard method (International Electrotechnical Commission [IEC] 62220-1, 2003) for DQE measurement and two previously described DQE evaluation methods were considered. In addition to an overall comparison, evaluations of the following method factors were performed: beam quality, beam-limiting devices (apertures or collimators), noise power spectrum (NPS) analysis algorithms and parameters (area, region of interest size, background detrending), and modulation transfer function (MTF) test devices and methods.

Results:

Overall, at low to middle frequencies, the IEC method yielded DQE estimates that were 3.3% and 6.5% lower than the values yielded by the two previous methods. Averaged over the frequency range of 1.5–2.5 mm⁻¹, the DQE estimate derived by using the IEC method was 7.1% lower and 12.4% higher than the estimates derived by using the other two methods. Results obtained with the two previous DQE evaluation methods agreed well (within 2.0%) in the low- to middle-frequency range but diverged by up to 10% at higher frequencies. When the DQE method factors were evaluated separately, the largest percentage deviations in DQE were associated with (in order of decreasing influence) the MTF analysis method (~11%), the beam limitation (about 7%–10%), the beam quality (~9%), and the NPS analysis method (~3%).

Conclusion:

Comparison of DQE estimates obtained by using the recently introduced international standard technique with those obtained by using prior methods revealed that the overall measurement method can affect the DQE estimate by as much as 12%. Findings further suggest that both beam limitation achieved by means of internal collimation (rather than external apertures) and use of a radio-opaque edge MTF device yield a more accurate estimation of the DQE.

© RSNA, 2007

¹ From Duke Advanced Imaging Laboratories, Department of Radiology, Duke University and Medical Center, 2424 Erwin Rd (Hock Plaza), Suite 302, Durham, NC 27705. Received March 30, 2006; revision requested May 31; revision received June 19; accepted June 23; final version accepted September 22. Supported in part by grants from the National Institutes of Health (R01 CA80490 and R01 CA109074). Address correspondence to N.T.R. (e-mail: nicole.ranger@duke.edu).

Detective quantum efficiency (DQE) historically has been the most commonly used metric of the overall image quality of radiographic systems (1). Defined as the ratio of the squared image signal-to-noise ratio to the number of incident x-ray photons, the DQE describes how efficiently a system translates incident x-ray photons into useful signal (relative to noise) within an image. With the introduction of digital radiographic imaging systems, the DQE has continued to be regarded as a convenient, reasonably accurate, and widely accepted metric of image quality (2,3).

Although the DQE is almost universally regarded as the best overall indicator of the image quality of digital radiography systems, until recently there was no universally accepted standard for the measurement of this parameter. In 2003, the International Electrotechnical Commission (IEC) published a standard method (4) for measurement of the DQE that also included specifications for the measurement of two associated metrics: the modulation transfer function (MTF) and the noise power spectrum (NPS). Given the large amount of literature on DQE measurements, the

introduction of the standard has created the need for insight into how the results acquired by using the standard technique compare with the results obtained by using prior methods (5,6). Thus, the purpose of our study was to prospectively evaluate the recently introduced international standard method for measurement of the DQE of digital radiography systems, in comparison with representative prior methods (7–13).

Materials and Methods

Imaging System

The prototype flat-panel detector used in this study was provided by GE Healthcare (Milwaukee, Wis) through a research agreement. To compare DQE measurement methods specifically—as opposed to the performance of specific imaging systems—all measurements were obtained (N.T.R.) by using a single representative flat-panel imaging device. This device has a 0.2-mm pixel pitch and an amorphous silicon–cesium iodide flat-panel detector equivalent to that in a commercially available system (Revolution XQ/i; GE Healthcare) (5,6,14). The detector was calibrated before the acquisition of imaging data according to manufacturer guidelines.

Advances in Knowledge

- Comparison of detective quantum efficiency (DQE) estimates obtained by using the recently introduced international standard technique with estimates obtained by using prior methods revealed that the overall measurement method can affect the DQE estimate by as much as 12%.
- The DQE method factors that had the greatest effect on the DQE estimate were (in order of decreasing influence) MTF analysis method (~11%), beam limitation (about 7%–10%), beam quality (~9%), and NPS analysis method (~3%).
- Findings suggest the use of both beam limitation achieved by means of internal collimation and a radio-opaque edge MTF device for more accurate estimation of the DQE.

Beam Conditions

Each of the three DQE measurement methods involves the use of an enhanced x-ray beam quality that is based on a combination of specified tube voltage and external beam-hardening filtration (Table 1). Furthermore, the three DQE techniques differ in terms of the method and extent of beam limitation used. The DQE measurement methods of both Dobbins et al (8) and Samei and Flynn (13) involved the use of the internal collimator of the tube to restrict the beam extent to the outer edge of the detector, whereas the IEC method (4) involves the use of a specified set of external lead apertures (Fig 1) to restrict the area of the beam to 16 × 16 cm.

The effect of beam quality in the absence of beam limitation was evaluated by using the IEC DQE method with

each of three beam qualities (Table 1). In addition, the effect of the beam limitation independent of beam quality was assessed by using the IEC-specified RQA5 beam quality (16) in three configurations: without beam limitation, with the IEC-specified external apertures, and with the internal tube collimators configured to achieve beam limitation comparable to that of the IEC-specified external apertures (5,6). It should be noted that the aluminum filtration used to achieve the RQA5 beam quality was type 1100 (99.0% purity) rather than the higher-purity (>99.9%) aluminum specified in the standard because of the highly visible structured image nonuniformities associated with the use of very-high-purity (≥99.9%) aluminum filtration (15).

Determination of MTF

As the first component of DQE assessment, the MTF was measured according to the prescribed MTF measurement device of each method—specifically, (a) a radiopaque edge (IEC [4]), (b) a slit (Dobbins et al [8]), and (c) a radiolucent edge (Samei and Flynn [13])—by using acquisition and analysis algorithms specific to each method. To isolate the effect of the MTF measurement method from all other factors, all MTF

Published online

10.1148/radiol.2433060485

Radiology 2007; 243:785–795

Abbreviations:

- DQE = detective quantum efficiency
 E_{NI} = IEC-defined normal exposure
IEC = International Electrotechnical Commission
MTF = modulation transfer function
NPS = noise power spectrum
 q = number of incident x-ray photons per unit area per unit of exposure incident on the detector
ROI = region of interest

Author contributions:

Guarantors of integrity of entire study, N.T.R., E.S., J.T.D.; study concepts/study design or data acquisition or data analysis/interpretation, all authors; manuscript drafting or manuscript revision for important intellectual content, all authors; manuscript final version approval, all authors; literature research, N.T.R., E.S., J.T.D.; experimental studies, N.T.R., E.S., J.T.D.; statistical analysis, N.T.R., E.S., J.T.D.; and manuscript editing, all authors

Authors stated no financial relationship to disclose.

devices were imaged by using the same beam quality (RQA5 beam quality at exposure of 1.03×10^{-6} C/kg [4.0 mR]). Additional images were acquired at exposures of 2.0×10^{-6} C/kg (7.7 mR) (slit) and 9.5×10^{-7} C/kg (3.7 mR) (radiolucent edge) by using the beam qualities associated with the Dobbins et al and Samei et al methods, respectively (Table 1). All MTF images were analyzed by using basic Fourier analysis techniques tailored to each method. The images of the slit device were analyzed with a slit MTF algorithm developed by Fujita et al (17) and adapted by Dobbins (7) and Dobbins et al (7,8). The radiolucent edge and radio-opaque edge images were analyzed according to the Samei et al and IEC methods by using an algorithm developed by Samei et al (9–13). Further details of the MTF data acquisition and analysis component of the current study are reported elsewhere (5).

Determination of NPS

The second component of the DQE evaluation involved acquiring NPS estimates—derived from flat-field images—by using the three methods. The image acquisition and analysis details for these measurements were described previously (6). Flat-field images were acquired at approximate exposures of $E_{nl}/3.2$, E_{nl} , and $3.2E_{nl}$, where E_{nl} (Table 1) is approximately 1.03×10^{-7} C/kg (0.4 mR), according to the manufacturer of

the detector used in this study. NPS estimates were derived from the images by using algorithms and parameters specific to each of the three methods. The three techniques involved similar processing parameters, with the exception of the area of the detector evaluated, the size and number of the regions of interest (ROIs) used for analysis, the background subtraction method (detrending), and the inclusion of on-axis data in the reported NPS results (Table 2). In addition, the images acquired by using the IEC beam quality and beam limitation were analyzed with each of the three NPS algorithms to assess the effect of computational technique alone. Further details of the NPS data acquisition and analysis component of the current study are reported elsewhere (6).

Determination of Incident Exposure and *q* Value

An essential step in determining the DQE is estimating the incident exposure (*E*) associated with each NPS measurement (Table 1). The incident exposure at the detector was estimated (N.T.R.) by using the system (linearity) response function (5) to convert the mean pixel value to an exposure value.

Another element required to compute the DQE is the *q* value (Table 1), which was estimated by means of computer spectrum modeling for each of the beam conditions evaluated. For the IEC

method, a *q* value of $264\,626\text{ mm}^{-2}\text{ mR}^{-1}$ was obtained by multiplying the IEC-specified *q* value (4) of $30\,174\text{ mm}^{-2}\text{ }\mu\text{Gy}^{-1}$ by the conversion factor of $8.77\text{ }\mu\text{Gy mR}^{-1}$ air kerma per unit exposure. For the Dobbins et al and Samei et al beam qualities, *q* values were computed (E.S. and J.T.D.) by using the DXSPEC (18) and xSpect (13) computational models and were $271\,500\text{ mm}^{-2}\text{ mR}^{-1}$ and $255\,855\text{ mm}^{-2}\text{ mR}^{-1}$, respectively, which correspond to the values used historically (7–13).

Computation of DQE

The frequency-dependent DQE, DQE(*f*), was computed (N.T.R.) by using the estimated MTF, NPS, *q*, and *E* values:

$$\begin{aligned} \text{DQE}(f) &= S^2 \frac{\text{MTF}^2(f)}{\text{NPS}(f) \times q \times E} \\ &= \frac{\text{MTF}^2(f)}{\text{NNPS}(f) \times q \times E}, \end{aligned}$$

where MTF(*f*) is the frequency-dependent MTF; NPS(*f*) is the frequency-dependent NPS; and NNPS(*f*) is the frequency-dependent normalized NPS (3,6), calculated as $[\text{NPS}(f)]/S^2$, where *S*² is the square of the large-area signal intensity (assuming the detector is linear with respect to exposure). The DQE estimates were computed with the quantities specific to each method or condition. For these computations, in

Table 1

X-ray Beam Conditions for Measurement of DQE

Beam Quality*	Beam Limitation	Tube Voltage (kV)	Measured HVL (mm Al) [†]	Exposure Estimate at Detector Surface (mR) [‡]			<i>q</i> Value (mm ⁻² mR ⁻¹) [§]
				$E_{nl}/3.2$	E_{nl}	$3.2E_{nl}$	
Dobbins et al (8)	None	70	0.5 mm Cu	6.7	0.187	0.494	271 500
Samei and Flynn (13)	None	70	19 mm Al [†]	6.6	0.195	0.400	255 855
IEC RQA5 with no aperture	None	74	21 mm Al [†]	7.1	NA	0.555	NA
IEC RQA5 with external aperture	External (16 × 16 cm)	74	21 mm Al [†]	7.1	0.197	0.526	264 626
IEC RQA5 with internal aperture	Internal collimator (16 × 16 cm)	74	21 mm Al [†]	7.1	NA	NA	264 626

* The IEC-specified RQA5 beam quality was evaluated with full detector irradiation—that is, with no apertures; with IEC-specified external lead apertures restricting the field of view to 16 × 16 cm; and with the device's internal collimator adjusted to simulate the effect of the IEC-specified external apertures. Numbers in parentheses are reference numbers.

† Aluminum (Al) type 1100 alloy (99.0% purity) was used for historical reasons and because of the nonuniformity of aluminum filtration with greater than 99.9% purity, as reported previously (15). HVL = half-value layer.

‡ E_{nl} = IEC-defined normal exposure (~0.4 mR). NA = not applicable; no exposure or NPS measurement was performed under this condition. 1 R = 2.58×10^{-4} C/kg.

§ *q* = number of incident x-ray photons per unit area per unit of exposure incident on the detector. 1 R = 2.58×10^{-4} C/kg.

|| Cu = copper.

adherence with the IEC specification and to facilitate comparisons, all of the MTF and NPS results were averaged into frequency-sampling intervals of 0.05 mm^{-1} . The DQE estimates derived by using each of the three methods were compared (N.T.R., E.S., J.T.D.). Additional comparisons were made to elucidate the isolated effects of beam quality, beam limitation, MTF analysis method, and NPS analysis method on the DQE estimate. DQE curves were then compared by computing the relative difference (expressed as a percentage) between one curve and another at each 0.05 mm^{-1} frequency bin and averaging over the frequency ranges of interest (N.T.R.). Error estimates for the DQE results were derived (N.T.R., E.S., and J.T.D.) from the reported MTF (5) and NPS (6) values and the error estimate in the computed exposure.

Results

Effect of Beam Limitation

With all other factors constant, across the entire frequency range, the mea-

sured DQE estimate without external beam-limiting apertures—that is, with full detector irradiation—was generally lower than that obtained when the IEC-specified external beam-limiting apertures were used. The results indicated a mean relative difference of 6.8% (standard deviation, 0.9) between the DQE estimates obtained with and those obtained without external apertures over spatial frequencies 0.5 mm^{-1} and greater (Fig 2). Within the same frequency range, the mean relative difference in the measured DQE estimate with use of the device's internal collimators for beam collimation compared with the DQE estimate obtained with use of the IEC-specified external apertures was 9.6% (standard deviation, 0.9).

Effect of Beam Quality

Regarding the effect of beam quality on the DQE estimate (Fig 3), all other factors except q —the effect of which was removed by evaluating the results in terms of the product of $q \cdot \text{DQE}$ —were kept constant. When the full detector was irradiated, the DQE estimate ob-

tained by using the beam quality for the Samei et al method (70 kV, 19 mm of aluminum) was only slightly lower than that obtained by using the IEC RQA5 beam quality (74 kV, 21 mm aluminum) (mean relative difference, 2.2%; standard deviation, 1.4%; over spatial frequencies of 0.5 mm^{-1} and greater). In comparison, over the same frequency range, the mean relative difference in the DQE estimate obtained by using the beam quality for the Dobbins et al method (70 kV, 0.5 mm of copper) was 8.7% (standard deviation, 1.4%) higher than that obtained by using the IEC RQA5 beam quality without apertures.

Effect of NPS Analysis Method

Isolating the effect of the NPS analysis approach, we evaluated the DQE estimate with each of the three NPS methods by using a common data set of flat-field images acquired according to the IEC protocol. With the effect of differences in q value between methods eliminated, the $q \cdot \text{DQE}$ products (Fig 4) for incident exposures of $E_{nl}/3.2$, E_{nl} , and $3.2E_{nl}$ indicated consistent results at all three exposure levels and excellent agreement among the different methods, except at the lowest spatial frequencies ($\leq 0.15 \text{ mm}^{-1}$), at which the $q \cdot \text{DQE}$ product derived by using the IEC-NPS method decreased precipitously. The mean relative difference in the estimated $q \cdot \text{DQE}$ products over spatial frequencies of 0.5 mm^{-1} and greater derived by using the methods of Dobbins et al (8), Samei and Flynn (historical) (13), and Samei et al (current) (Table 2) were, respectively, 0.3%, 2.8%, and 2.0% (standard deviation, ≤ 1.2) higher than the product derived by using the IEC standard method.

Combined Effect of NPS and MTF Methods

Qualitatively, the results obtained at different incident exposures with each method were consistent except at very low spatial frequencies. For the NPS-MTF methods of Dobbins et al and Samei et al, the $q \cdot \text{DQE}$ product estimates were higher than those obtained by using the IEC standard method, except at the highest spatial frequencies (Fig 5). Furthermore, within the limits

Figure 1

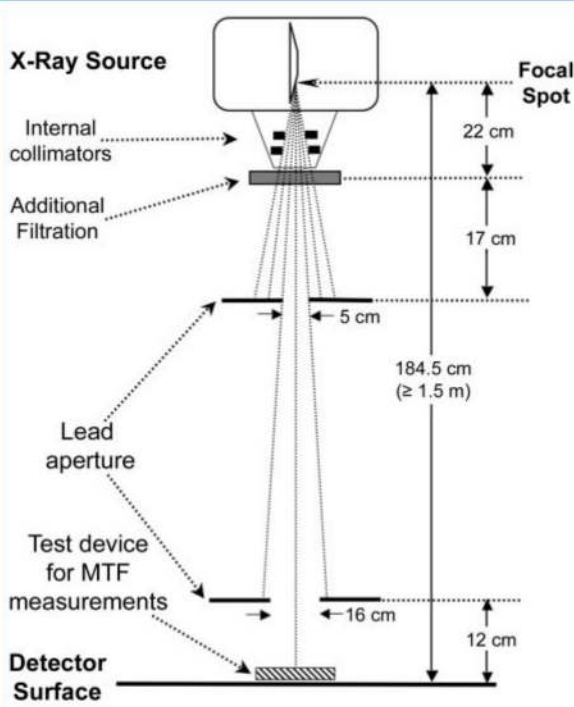


Figure 1: DQE test geometry, compliant with the IEC 62220-1 standard. For the RQA5 beam quality, additional filtration with 21 mm of aluminum is used to simulate the spectral quality of radiation incident on the detector during a typical clinical examination. The detector is positioned at a source-to-image distance of 1.5 m or greater. The internal collimator of the device and external beam-limiting lead apertures are adjusted to achieve a radiation field of approximately $16 \times 16 \text{ cm}$ at the detector surface. The IEC standard specifies the exact position and size of only the aperture closest to the detector. The radio-opaque MTF device is placed adjacent to the detector as shown.

Table 2**Summary of Measurement Parameters for Evaluated DQE Methods**

Overall DQE Method	IEC Apertures	Beam Quality*	MTF Device	MTF Analysis Method	NPS Analysis Method	NPS Analysis Area†	ROI Size and Type‡	NPS Band Size§	NPS Detrending
Dobbins et al	None	70 kV 0.5 mm Cu	Slit	Dobbins et al	Dobbins et al	640 × 640 Pixels (10)	128 Pixels, NOL	±4	Two-dimensional (first order)
						1024 × 1024 Pixels (1)			
Samei and Flynn	None	70 kV 19 mm Al	Radiolucent edge	Samei and Flynn	Samei and Flynn	640 × 640 Pixels (10)	128 Pixels, NOL	±7 With on-axis data	Two-dimensional (second order)
Historical						1280 × 1280 Pixels (1)			
Current						640 × 640 Pixels (3)	128 Pixels, OL		
						1280 × 1280 Pixels (1)			
IEC [¶]	External	RQA5	Radiopaque edge	IEC	IEC	640 × 640 Pixels (3)	256 Pixels, OL	±7	Two-dimensional (second order)
						640 × 640 Pixels (10)			

Note.—Parameters used in the Dobbins et al (8), Samei and Flynn (13), and IEC (4) methods are given.

* Cu = copper, Al = aluminum.

† The first set of parameters corresponds to the parameters employed for the evaluation of the NPS and combined NPS plus MTF dependence on the DQE estimate. Comparable statistical quality in the NPS estimates was achieved by varying the relative number of images analyzed with each method (5). The second set of parameters corresponds to results regarding the effect of the overall DQE method. The number of images analyzed was indicated by the specifications of each image, or in the case of the IEC method, by the requirement to use a total of at least 4 million independent image pixels in the NPS analysis. The number of images used is in parentheses.

‡ NOL = nonoverlapping (one pass) ROIs, OL = overlapping (four passes) ROIs.

§ Number of rows of data averaged in two-dimensional NPS to produce a one-dimensional NPS curve.

¶ The IEC method requires the use of 256 × 256-pixel ROIs for NPS analysis involving the use of an overlapping placement scheme achieved with four successive analysis passes with ROIs offset as follows: (x, y); x + 128, y; x, y + 128; and x + 128, y + 128. x And y are the reference coordinates for the top left-most corner of the analysis area.

of uncertainty there appeared to be close agreement (within 2% on average) between the results obtained by using the Dobbins et al and those obtained by using the Samei et al method in the low to middle range of spatial frequencies (0.15–1.00 mm⁻¹). However, the results obtained by using the historical and current methods of Samei et al, which did not differ by a mean of more than 1.5% (standard deviation, 0.8) over the frequency range of 0.5–2.5 mm⁻¹, began to diverge from those obtained by using the method of Dobbins et al at spatial frequencies of 1.0 mm⁻¹ and greater and approached the results obtained by using the IEC method at spatial frequencies of 2.0 mm⁻¹ and greater. When averaged over spatial frequencies of 0.5 mm⁻¹ and greater, the mean relative differences in the $q \cdot$ DQE product estimates derived by using the methods of Dob-

bins et al, Samei et al (historical), and Samei et al (current) were, respectively, 13.3%, 7.5%, and 6.7% (standard deviation, ≤1.2) higher than the product obtained by using the IEC standard method. From these results, the effects of MTF analysis (5) alone were estimated to be 11.0%, 4.4%, and 4.4% (standard deviation, ≤0.4), respectively.

Comparison of Overall Methods

Overall comparison of the DQE estimates obtained by using each method (Fig 6a) revealed that when the effect of variations in q were excluded, use of the DQE method of Dobbins et al, as compared with use of the IEC DQE method, resulted in a higher $q \cdot$ DQE product estimate over the full frequency range but yielded results that approached those obtained by using the IEC method at the cutoff frequency. The results derived by

using the historical and current methods of Samei et al agreed with each other quite well at all spatial frequencies. Within the 0.15–0.75 mm⁻¹ range, use of the Samei et al method resulted in $q \cdot$ DQE products that were qualitatively greater than those obtained by using the IEC method and essentially equivalent to those obtained by using the Dobbins et al method. In the spatial frequency range of 0.8–1.1 mm⁻¹, the Samei et al method yielded $q \cdot$ DQE product estimates that were roughly equivalent to those obtained by using the IEC method. However, beyond this range, the Samei et al method yielded product estimates that were lower than those obtained by using the Dobbins et al and IEC standard methods.

The DQE estimates (with q value dependence included) derived by using the Dobbins et al and IEC methods (Fig

6b) were in the closest agreement in the frequency range of $0.25\text{--}1.25\text{ mm}^{-1}$, with the IEC method yielding DQE estimates that were comparatively lower (mean relative difference, 5.7%; standard deviation, 0.8%; over frequencies greater than 0.5 mm^{-1}). The historical and current methods of Samei et al agreed well with one another over the full range of frequencies (mean relative difference, 1.5%; standard deviation, 0.9%; over frequencies of greater than 0.5 mm^{-1}), and both techniques yielded DQE estimates that were higher (at low frequencies) and lower (at high frequencies) than those derived by using the Dobbins et al and IEC methods (Table 3). The crossover point at which all methods yielded equivalent DQE estimates was approximately 1.0 mm^{-1} .

Discussion

Our study results show that moderate differences in estimated DQE that result from methodologic differences do exist. With publication of the recently introduced international standard for DQE measurement (IEC 62220-1), a consensus as to the “best practice” method for DQE evaluations has been reached that will facilitate future intercomparisons. Nevertheless, there is still a broad body of published literature on existing imaging devices, and the results obtained by using the international standard method cannot be easily compared with the previously published results obtained by using the other methods.

We found that the values obtained by using the IEC method were lower

than those obtained by using the established methods of Dobbins et al (8) and Samei and Flynn (13) at low frequencies and intermediate between the Dobbins et al and Samei et al results at frequencies of greater than 1.5 mm^{-1} . At the very lowest frequencies, the results obtained by using the IEC method (4) diverged substantially from those obtained by using the Samei et al methods. In the IEC-reporting range ($\geq 0.5\text{ mm}^{-1}$) and relative to the IEC method, the greatest differences were seen in the middle to high frequency range, corresponding to mean relative differences of approximately 7% (Dobbins et al vs IEC method) and approximately 12% (Samei et al vs IEC method).

Our two prior reports (5,6) describe in detail the comparison of spe-

Figures 2, 3

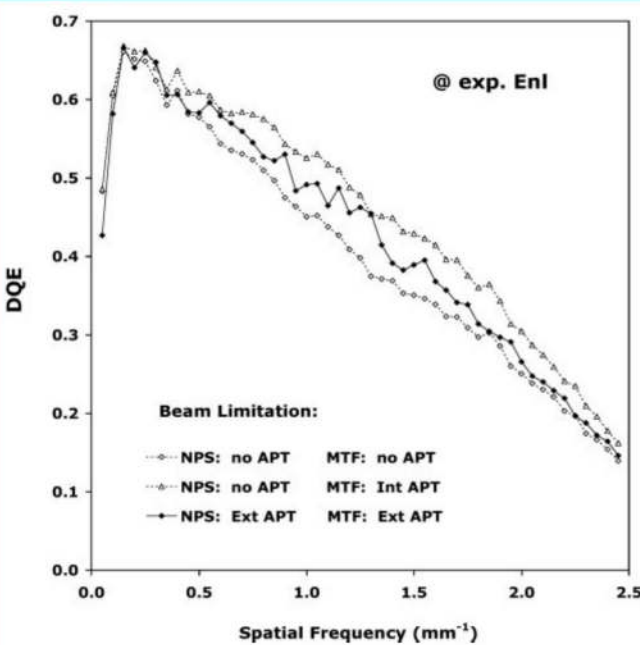


Figure 2: Graph illustrates effects of various beam-limiting conditions on DQE estimates: full detector irradiation with no external apertures (NPS: no APT, MTF: no APT), limited $16 \times 16\text{-cm}$ detector irradiation for MTF measurement with internal collimators and no additional external apertures (NPS: no APT, MTF: Int APT), and limited $16 \times 16\text{-cm}$ detector irradiation with external apertures (NPS: Ext APT, MTF: Ext APT). Data were collected by using the IEC RQA5 beam quality and the IEC standard acquisition and processing method. Ten images acquired at a detector exposure level corresponding to E_{nl} (Table 1) were analyzed by using a total of 160 overlapping 256×256 -pixel ROIs for the NPS component of the DQE measurements. Error bars less than $\pm 2.5\%$.

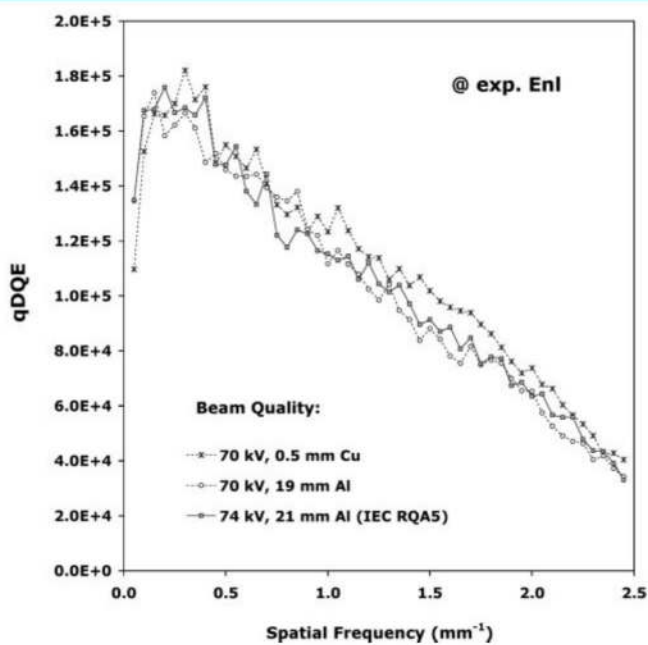


Figure 3: Graph illustrates DQE dependence on beam quality. The $q \cdot DQE$ products obtained with the following beam qualities are plotted: 70 kV, 0.5 mm of copper filtration (used by Dobbins et al); 70 kV, 19 mm of aluminum filtration (used by Samei et al); and 74 kV, 21 mm of aluminum filtration (IEC RQA5) with no added apertures. Excluding beam quality, in all other respects the acquisition and processing method complied with the IEC standard. Three images acquired at a detector exposure level corresponding to E_{nl} (Table 1) were analyzed by using a total of 48 overlapping 256×256 -pixel ROIs for the NPS component of the DQE measurements. Error bars less than $\pm 4.3\%$.

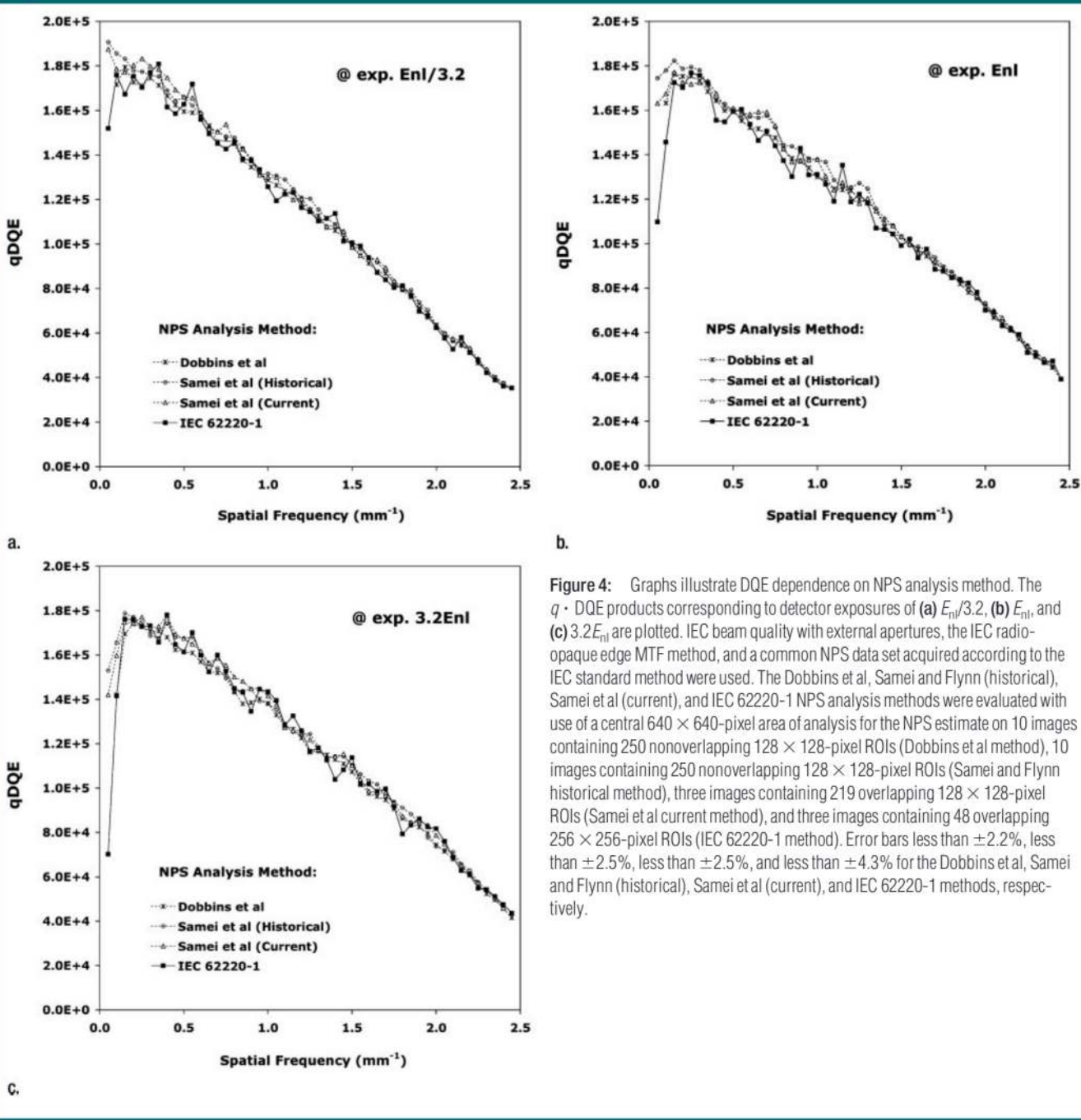
Figure 4

Figure 4: Graphs illustrate DQE dependence on NPS analysis method. The $q \cdot \text{DQE}$ products corresponding to detector exposures of (a) $E_{\text{nl}}/3.2$, (b) E_{nl} , and (c) $3.2E_{\text{nl}}$ are plotted. IEC beam quality with external apertures, the IEC radio-opaque edge MTF method, and a common NPS data set acquired according to the IEC standard method were used. The Dobbins et al, Samei and Flynn (historical), Samei et al (current), and IEC 62220-1 NPS analysis methods were evaluated with use of a central 640×640 -pixel area of analysis for the NPS estimate on 10 images containing 250 nonoverlapping 128×128 -pixel ROIs (Dobbins et al method), 10 images containing 250 nonoverlapping 128×128 -pixel ROIs (Samei and Flynn historical method), three images containing 219 overlapping 128×128 -pixel ROIs (Samei et al current method), and three images containing 48 overlapping 256×256 -pixel ROIs (IEC 62220-1 method). Error bars less than $\pm 2.2\%$, less than $\pm 2.5\%$, less than $\pm 2.5\%$, and less than $\pm 4.3\%$ for the Dobbins et al, Samei and Flynn (historical), Samei et al (current), and IEC 62220-1 methods, respectively.

specific MTF and NPS results. In terms of NPS analysis, all three methods agreed exceptionally well (mean relative difference, $<1.6\%$; standard deviation, 0.6% ; over the frequency range of 0.15 mm^{-1} to cutoff). Since none of the measurement parameters had a substantial effect on the measured NPS, we can

infer that the observed differences between the DQE measurement methods were not due in any substantial way to differences in the NPS technique, except at the very lowest spatial frequencies ($<0.2 \text{ mm}^{-1}$), at which the differences were due to a combination of the detrending method and the size of the

ROIs used for NPS measurement (6). It should be noted tangentially that although beam limitation had no measurable effect on the NPS estimates, the use of beam limitation had the disadvantage of increasing the number of images required to achieve the same number of independent image pixels and a compa-

rable level of precision in the NPS and DQE estimates.

In terms of MTF analysis, we noted differences in the measured MTF as a function of the applied method in our recent report (5). Although the differences were relatively modest, because

the MTF term in the expression for DQE is squared, the MTF method accounted for the majority of the noted differences in the DQE estimates. Primarily related to the MTF, beam quality and beam limitation each were found to individually affect the DQE estimate by

7%–10%. Results from a related study (5) demonstrated that in the presence of device misalignment and image glare (1), the MTF estimate measured by using a slit (Dobbins et al method) was less accurate than the MTF estimate measured by using an edge (Samei et al

Figure 5

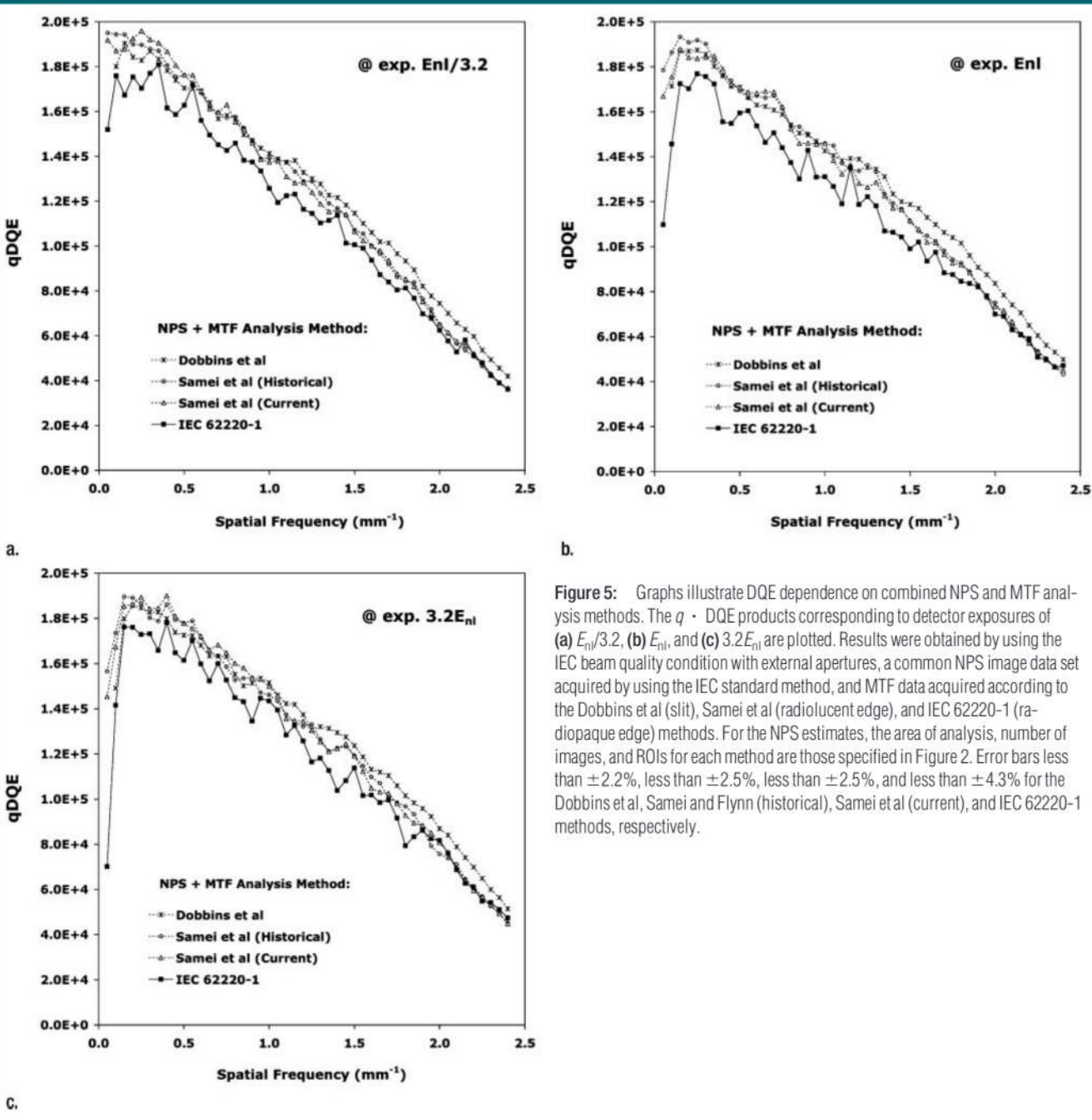
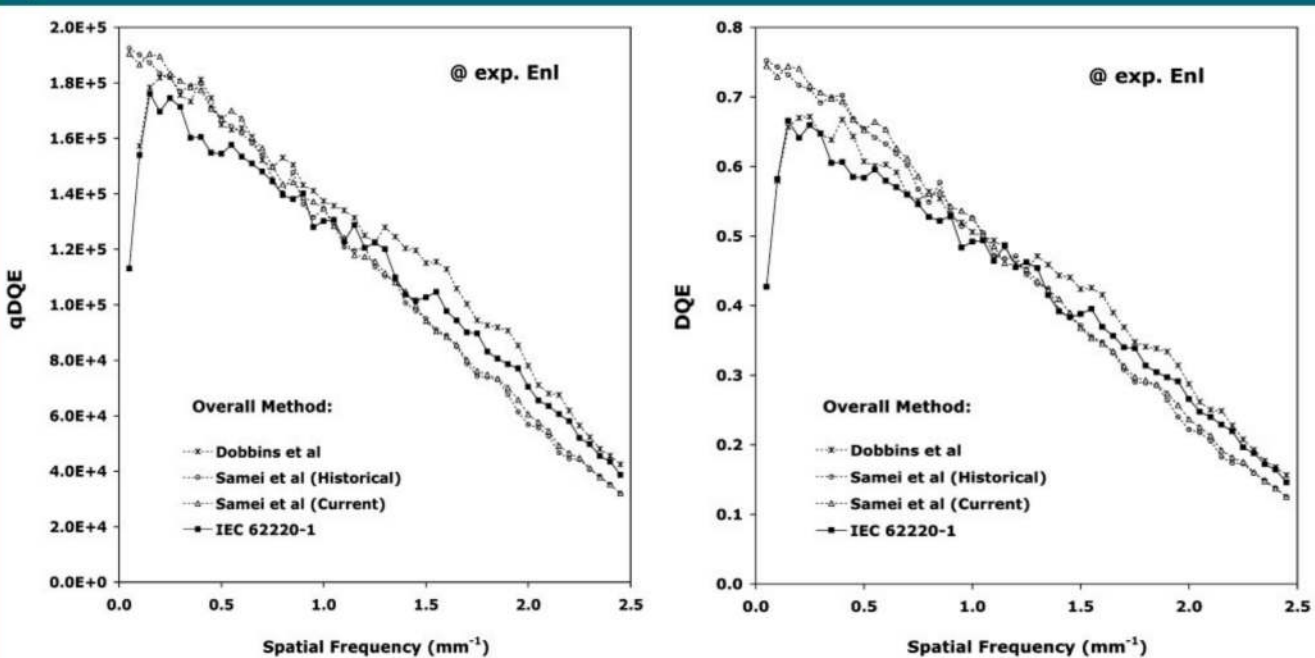


Figure 5: Graphs illustrate DQE dependence on combined NPS and MTF analysis methods. The $q \cdot DQE$ products corresponding to detector exposures of (a) $E_{nl}/3.2$, (b) E_{nl} , and (c) $3.2E_{nl}$ are plotted. Results were obtained by using the IEC beam quality condition with external apertures, a common NPS image data set acquired by using the IEC standard method, and MTF data acquired according to the Dobbins et al (slit), Samei et al (radiolucent edge), and IEC 62220-1 (radiopaque edge) methods. For the NPS estimates, the area of analysis, number of images, and ROIs for each method are those specified in Figure 2. Error bars less than $\pm 2.2\%$, less than $\pm 2.5\%$, less than $\pm 2.5\%$, and less than $\pm 4.3\%$ for the Dobbins et al, Samei and Flynn (historical), Samei et al (current), and IEC 62220-1 methods, respectively.

Figure 6

a.

Figure 6: Graphs illustrate comparison of overall DQE methods, including beam quality and limitation, NPS analysis method, and MTF analysis method (a) without and (b) with q value variations taken into consideration at detector exposure levels corresponding to E_{nl} . For the Dobbins et al overall method, the following parameters were used: 70 kV with 0.5 mm of copper filtration (no beam limitation), the slit MTF method, a 1024×1024 -pixel analysis area on one image with 64 nonoverlapping 128×128 -pixel ROIs for NPS analysis, and a q value of $271\,500 \text{ mm}^{-2} \text{ mR}^{-1}$. For the Samei and Flynn historical method, the following parameters were used: 70 kV with 19 mm of aluminum filtration (no beam limitation), the radiolucent edge MTF method, a 1280×1280 -pixel analysis area on one image with 100 nonoverlapping 128×128 -pixel ROIs for NPS analysis, and a q value of $255\,855 \text{ mm}^{-2} \text{ mR}^{-1}$. For the Samei et al current method, the historical method parameters were used, with the exception that 343 overlapping 128×128 -pixel ROIs were used for NPS analysis. For the IEC 62220-1 method, the following parameters were used: 74 kV with 21 mm of aluminum filtration, IEC-specified external apertures, the IEC radiopaque edge MTF method, a 640×640 -pixel analysis area on 10 images with 160 overlapping 256×256 -pixel ROIs for NPS estimates, and a q value of $264\,626 \text{ mm}^{-2} \text{ mR}^{-1}$. Error bars less than $\pm 4.0\%$, less than $\pm 3.8\%$, less than $\pm 2.2\%$, and less than $\pm 2.5\%$ for the Dobbins et al, Samei and Flynn (historical), Samei et al (current), and IEC 62220-1 methods, respectively.

Table 3**Relative Differences in DQE Estimates between the Three DQE Measurement Methods**

Spatial Frequency Range	Samei and Flynn (historical) vs IEC Method	Samei et al (current) vs IEC Method	Dobbins et al vs IEC Method	Samei and Flynn (historical) vs Dobbins et al Method
0.5–2.5 mm ⁻¹	-4.3 ± 0.9	-2.9 ± 0.8	5.7 ± 0.8	-5.2 ± 1.0
0.25–1.25 mm ⁻¹	6.5 ± 1.0	7.5 ± 0.8	3.3 ± 1.1	1.5 ± 1.3
1.5–2.5 mm ⁻¹	-12.4 ± 1.3	-10.8 ± 1.1	7.1 ± 1.1	-10.0 ± 1.4

Note.—Data are mean relative differences, cited as percentages, \pm standard deviations.

and IEC methods). In that study, it was concluded that the radiopaque edge method recommended by the IEC and the beam limitation achieved by using the device's internal collimators yield the most accurate estimate of overall MTF in the presence of glare and there-

fore constitute the preferred approach for characterizing the MTF for DQE measurement.

An important element of DQE evaluation is estimation of the level of exposure associated with the NPS measurement used to compute the DQE estimate. Di-

rect single-exposure measurements generally have a precision of 5%–10%. In our study, we used an average of a large number of individual exposure measurements (6) to improve precision to within about 0.6% at high exposure values but only achieved a precision of within about 6.4%

at low exposures. However, our use of the system transfer function in the exposure estimation process (5) resulted in further precision, yielding an overall exposure uncertainty of about 0.2% across the exposure range. This improvement in precision had a favorable influence on the precision of DQE estimates, enabling a more statistically rigorous comparison of the methods.

Notwithstanding the findings, the present investigation was limited in a number of respects. First, the study was aimed at comparing the recently introduced international standard with only two other methods. Other DQE assessment methods would probably compare differently. Second, the comparisons were made at only a single—although typical—range of x-ray spectra based on a tube voltage of about 70 kVp. The evaluated methods might compare differently at other beam qualities. Finally, the study was based on evaluation involving the use of only one image receptor—namely, an indirect flat-panel detector. This limitation resulted from the intended focus of the study, which was the intercomparison of methods rather than of systems. Nevertheless, the findings of this study are generalizable (with caveats), because the relative differences between the DQE estimates observed in this work are likely to be reflective of the relative magnitude of expected differences due to varying measurement methods for other classes of digital radiographic imaging systems. Furthermore, for studies in which the same type of flat-panel device is used, a quantitative correction could be applied to relate the DQE measurement to any of the three DQE measurement methods described herein.

In summary, we found that the choice of overall measurement method can affect the DQE results by as much as 12%; therefore, careful attention to the details of the DQE measurement method is necessary to ensure reliable estimation of the DQE and comparison with previously published results. The DQE results obtained by using the Dobbins et al and Samei et al methods agreed well at low to middle frequencies (mean relative difference, 2.0%; stan-

dard deviation, 1.3; over frequency range of 0.25–1.25 mm⁻¹) but deviated substantially at higher frequencies (mean relative difference, 10.0%; standard deviation, 1.4; over frequency range of 1.5–2.5 mm⁻¹). The IEC technique yielded lower DQE estimates than either of these methods in the 0.25–1.25 mm⁻¹ range (mean relative differences, 3.3% and 6.5%, respectively; standard deviations, 1.1 and 1.0, respectively), whereas at frequencies of greater than 1.5 mm⁻¹, the IEC method yielded estimates intermediate between the Dobbins et al and Samei et al (historical) values (mean relative differences, 7.1% and 12.4%, respectively; standard deviations, 1.1 and 1.3, respectively). We have the following recommendations regarding DQE measurements, which are based on our study results and consistent with the findings reported in associated publications (5,6):

1. Using the IEC RQA5 spectrum (based on an iteratively achieved target half-value layer with type 1100 aluminum filtration for improved image uniformity [15]) yields a calibrated spectrum, but for well-calibrated radiographic systems it probably has little advantage over using a specific target voltage and filtration (as in the Samei et al and Dobbins et al methods).
2. Use of internal collimation instead of the IEC-specified external beam apertures yields better estimates of the MTF and the DQE while diminishing the complexity of image acquisition (5).
3. Use of a more conventional (larger) field of view (as in the Samei et al and Dobbins et al methods), as opposed to the beam limitation specified by the IEC, reduces the number of images required to achieve low variance in NPS and DQE results (6).

4. Using a radiopaque edge (as in the IEC standard method) to measure the MTF component of the DQE permits relatively easy alignment compared with using a slit and yields a more accurate measurement of the MTF in the presence of image glare than either the slit method or the radiolucent edge method (5).

5. In NPS analysis, use of 128 × 128-pixel ROIs, coupled with second-

order polynomial background detrending (as in the Samei et al method), improves estimation of the DQE at low frequencies (6).

Acknowledgments: The authors acknowledge the assistance in data acquisition and processing provided by Devon Godfrey, PhD, Ying Chen, MS, and Brian Harrawood, BA, of Duke University.

References

1. Dainty JC, Shaw R. *Image science*. London, England: Academic Press, 1974.
2. Cunningham IA. Applied linear-systems theory. In: Beutel J, Kundel HL, van Metter RL, eds. *Proceedings of SPIE: medical imaging 2000—handbook of medical imaging*. Vol 1. Bellingham, Wash: International Society for Optical Engineering, 2000; 79–160.
3. Dobbins JT III. Image quality metrics for digital systems. In: Beutel J, Kundel HL, van Metter RL, eds. *Proceedings of SPIE: medical imaging 2000—handbook of medical imaging*. Vol 1. Bellingham, Wash: International Society for Optical Engineering, 2000; 161–222.
4. International Electrotechnical Commission. Medical electrical equipment: characteristics of digital x-ray imaging devices—part 1: determination of the detective quantum efficiency. Document no. 62220-1. Geneva, Switzerland: International Electrotechnical Commission, 2003.
5. Samei E, Ranger NT, Dobbins JT 3rd, Chen Y. Inter-comparison of methods for image quality characterization. I. Modulation transfer function. *Med Phys* 2006;33:1454–1465.
6. Dobbins JT 3rd, Samei E, Ranger NT, Chen Y. Inter-comparison of methods for image quality characterization. II. Noise power spectrum. *Med Phys* 2006;33:1466–1475.
7. Dobbins JT 3rd. Effects of undersampling on the proper interpretation of modulation transfer function, noise power spectra, and noise equivalent quanta of digital imaging systems. *Med Phys* 1995;22:171–181.
8. Dobbins JT 3rd, Ergun DL, Rutz LD, Hinshaw DA, Blume H, Clark DC. DQE(f) of four generations of computed radiography acquisition devices. *Med Phys* 1995;22: 1581–1593.
9. Samei E, Flynn MJ, Reimann DA. A method for measuring the pre-sampled MTF of digital radiographic systems using an edge test device. *Med Phys* 1998;25:102–113.
10. Flynn MJ, Samei E. Experimental comparison of noise and resolution for 2k and 4k

- storage phosphor radiography systems. *Med Phys* 1999;26:1612–1623.
11. Samei E, Flynn MJ. An experimental comparison of detector performance for computed radiography systems. *Med Phys* 2002;29:447–459.
 12. Samei E. Image quality in two phosphor-based flat panel digital radiographic detectors. *Med Phys* 2003;30:1747–1757.
 13. Samei E, Flynn MJ. An experimental comparison of detector performance for direct and indirect digital radiography systems. *Med Phys* 2003;30:608–622.
 14. Floyd CE Jr, Warp RJ, Dobbins JT 3rd, et al. Imaging characteristics of an amorphous silicon flat-panel detector for digital chest radiography. *Radiology* 2001;218:683–688.
 15. Ranger NT, Samei E, Dobbins JT III, Ravin CE. Measurement of the detective quantum efficiency in digital detectors consistent with the IEC 62220-1 standard: practical considerations regarding the choice of filter material. *Med Phys* 2005;32:2305–2311.
 16. International Electrotechnical Commission. Medical diagnostic x-ray equipment: radiation conditions for use in the determination of characteristics. Document no. 61267. Geneva, Switzerland: International Electrotechnical Commission, 1994.
 17. Fujita H, Tsai DY, Itoh T, et al. A simple method for determining the modulation transfer function in digital radiography. *IEEE Trans Med Imaging* 1992;11:34–39.
 18. Ergun DL, Eastgate RJ, Jennings RJ, Siedband MP. DXSPEC: a computer program for diagnostic x-ray spectral filtration studies. Madison, Wis: University of Wisconsin-Madison Department of Medical Physics, 1977.